Order Number 9520438

Numerical modeling of the transient thermal interference of vertical U-tube heat exchangers

Muraya, Norman Kaguma, Ph.D.

Texas A&M University, 1994

U·M·I
300 N. Zeeb Rd.
Ann Arbor, MI 48106

NUMERICAL MODELING OF THE TRANSIENT THERMAL INTERFERENCE OF VERTICAL U-TUBE HEAT EXCHANGERS

A Dissertation

by

NORMAN K. MURAYA

Submitted to the Office of Graduate Studies of
Texas A&M University
in partial fulfillment of the requirements for the degree of

DOCTOR OF PHILOSOPHY

December 1994

Major Subject: Mechanical Engineering

NUMERICAL MODELING OF THE TRANSIENT THERMAL INTERFERENCE OF VERTICAL U-TUBE HEAT EXCHANGERS

A Dissertation

by

NORMAN K. MURAYA

Submitted to Texas A&M University
in partial fulfillment of the requirements
for the degree of

DOCTOR OF PHILOSOPHY

Approved as to style and content by:

Dennis L. O'Neal
(Co-Chair of Committee)

Warren M. Heffington
(Co-Chair of Committee)

Guy Fipps
(Member)

Harry A. Hogan
(Member)

G. P. Peterson
(Head of Department)

December 1994

Major Subject: Mechanical Engineering

ABSTRACT

Numerical Modeling of the Transient Thermal Interference

of Vertical U-tube Heat Exchangers. (December 1994)

Norman K. Muraya, B.S., Wheaton College;

B.S., Texas A&M University; M.S., Texas A&M University

Co-Chairs of Advisory Committee: Dr. Dennis L. O'Neal
Dr. Warren M. Heffington

Non-linear finite element models were developed to simulate transient heat and mass transfer in the soil surrounding the ground heat exchangers of ground-coupled heat pumps (GCHPs) operating in the cooling mode. Parametric studies were performed with two dimensional horizontal cross sectional models. The heat transfer and temperature distributions yielded excess errors less than 6% and 3%, respectively, when compared to analytical solutions.

Two constant temperature sources performed equivalent heating as one constant temperature source having twice the radius. For constant heat flux sources, the equivalent radius was found to be increased by $\sqrt{2}$. A heat flux equivalent radius ($r_{h,eqv}$) was developed and shown to be more consistent than the geometric radius ($r_{g,eqv}$). All equivalent radii varied with time and source separation.

A heat exchanger effectiveness for two sources, (ε_Λ), was introduced based on an earlier definition for one source. Effectiveness was found to be independent of a dimensionless temperature variable that included temperatures of the tubes and soil, and varied only with separation distance at steady state. Thermal short circuiting was defined as $1 - \varepsilon_\Lambda$ and ranged from 38% to 47% in the reasonable installation separation range.

Non-homogenous media were modeled by varying backfill thermal conductivity. Maximum heat transfer was achieved with a fictitious backfill thermal conductivity of 1,000 W/m-K, while measured bentonite backfill conductivities were less than 2

W/m-K. The overall heat transfer increased with backfill thermal conductivity but ε_Λ decreased. Therefore, the backfill effectiveness ($\varepsilon_{b'fil}$) of Couvillion was used to rank backfill performance. The range of $\varepsilon_{b'fil}$ was from 45% for touching bentonite backfill tubes to 60% for the fictitious backfill at a separation of seven l/D_o.

Moisture migration was incorporated into the numerical finite element model by formulating coupled partial differential equations for non-linear heat and mass transfer. Simulations with decreasing soil moisture contents resulted in lower thermal conductivity and performance degradation.

Increasing the bore hole size improved the efficiency (decreased thermal short circuiting) by as much as 20%. In addition, higher conductivity fictitious backfills improved efficiency by up to an additional 20%. However, cost savings in both cases had a negligible effect compared to the bore hole cost.

DEDICATION

I wish to dedicate this dissertation to my parents, Beth Wanjiru and Ayub Muraya for their invaluable support and encouragement for excellence in learning.

ACKNOWLEDGEMENTS

I wish to thank my Co-Chairmen Dr. Warren Heffington and Dr. Dennis O'Neal for their time and technical supervision. In addition, I appreciated the Ph.D. committee guidance extended by Dr. Hogan in Mechanical Engineering and Dr. Fipps in Agricultural Engineering. I gratefully acknowledge employment and industrial experience provided during the course of this study. Partial employment was provided by the Department of Energy (DOE) projects for the Energy Analysis and Diagnostic Center and the Industrial Assessment Center. Additional employment was also provided by the LoanSTAR program for the State of Texas.

NOMENCLATURE

Symbol	Description	MKS Units
a	coefficients of general two-point boundary-value problems	
a_1	coefficient of temperature dependent heat source	
C_p	coefficient of $\dot{T}$ in FE heat equation (ρc_p)	$kJ/(m^3 \cdot K)$
c_p	specific heat	$kJ/(kg \cdot K)$
$[C]$	FE capacitance matrix	
D_T	thermal moisture diffusivity	$m^2/(s \cdot K)$
D_o	diameter of cylindrical heat sourse	m
d	y cartesian coordinate for line source	m
E	specific enthalpy	kJ/kg
e	enthalpy	kJ
$F(Z)$	cylindrical constant temperature weighting function	
$[F]$	FE matrix for source terms and loads	
f	FE source terms and loads	
$G(Z,R)$	cylindrical heat source weighting function	
g	gravitational constant	m/s^2
h	convection term in heat transfer	$kJ/m^2 \cdot K$
J_i^j	Bessel function first kind of order i and exponential j	
k	thermal conductivity	$W/m \cdot K$
$[K]$	FE dependent variable loading matrix	
K_i	hydraulic conductivity of phase i	m/s
L	latent heat	kJ/kg
l	length	m
M	mass	kg
$\dot{m}$	mass flux density	$kg/(m^2 \cdot s)$
n	normal coordinate	m
P	total gas pressure	$Pa = N/m^2$ or $bar = 10^5 Pa$

p	partial pressure	bar or Pa
Q	heat flux	W
q	specific heat flux	W/kg
Q_T	heat flux proportional to temperature	W/K
R	radii	
R_{gc}	specific gas constant	$kJ/(kg \cdot K)$
$R.H.$	relative humidity	
r	radial coordinate	m
$r_{g,eqv}$	geometric equivalent radius for dual source $= \frac{r_\infty}{(r_\infty/r_1)^{(Q_1/Q_{eqv})}}$	
$r_{h,eqv}$	heat flux equivalent radius for dual source or equivalent number of sources $= \frac{Q_{eqv}}{(Q_1+Q_2)/2}$	
$r_{hi,g,eqv}$	equivalent high temperature geometric radius for dual source $= \frac{r_\infty}{(r_\infty/r_1)^{(Q_{hi}/Q_{eqv})}}$	
r_{res}	residual in FE variational formulation	
r_o	radius of cylindrical heat sourse (R=1.0)	m
S_L	liquid source (+) or sink (-)	kg/m^3
S_s	specific storage	m^{-1}
T	temperature	^oC
t	time	s
u	generic variable to be solved in general FE variational formulation	
v	FE variational test function	
x	cartesian coordinate	m
x_{sep}	non-dimensioal separation parameter $=(x + 2r_o)/r_o$ or (l/D_o)	
Y_i^j	Bessel function second kind order i and exponential j	
y	cartesian coordinate	m
Z	Fourier number $=(\alpha t/R_o^2)$	
z	cartesian depth coordinate	m

LIST OF GREEK SYMBOLS

Symbol	Description	MKS Units
α	thermal diffusivity	m^2/s
α_h	coefficient of heat diffusion boundary condition	
β	$= \frac{r}{2\sqrt{\alpha(t-\tau)}}$ parameter in transient line solution	
β_h	coefficient of heat diffusion boundary condition	
β_T	liquid thermal expansivity	K^{-1}
Γ	property conserved by flux in FE variational formulation	
γ	FE formulation constant loading	
δ	change in property	
ε_Λ	coil thermal effectiveness $\frac{Q_{1+2,net}}{(Q_{1,isolated}+Q_{2,isolated}}$	
$\varepsilon_{b'fil}$	backfill thermal effectiveness $= \frac{\sum\lvert Q'/k\rvert}{\sum\lvert T_c-T_{ff}\rvert}$	
ζ	$(\Delta T)_a/(\Delta T)$	
η	coordinate for y in FE master element	
θ	time integration scheme	
θ_{cyln}	cylindrical angular coordinate	$radians$
θ_l	volumetric water content	
θ_w	water content fraction	
Λ	thermal short circuiting $(1-\varepsilon_\Lambda)$	
λ	$=k$ thermal conductivity	$W/m \cdot K$
ξ	coordinate for x in FE master element	
ρ	density	kg/m^3
σ	flux in FE variational formulation	
σ'	total stress in FE moisture equation	n/m^2
Φ	porosity	
ϕ_i	FE basis functions	

φ_T	imensionless temperature = $\frac{T_{hi}-Tlo}{T_{hi}-T_{ff}}$	
Ψ	suction pressure	m^{-1}
ψ_i	FE shape functions	
$\hat{\Omega}$	master FE element	
Ω_e	actual element in FE grid	
$\partial\Omega$	boundary of FE element	

LIST OF SUBSCRIPT SYMBOLS

Symbol	Description
d	dry
ff	farfield (∞)
h	heat
l	liquid
μ	dynamic viscosity
o	condition at time zero
p	constant pressure
s	soil
v	vapor
w	water

TABLE OF CONTENTS

CHAPTER		Page
I	INTRODUCTION	1
I.1	Challenges of Cooling-dominated GCHPs	4
I.2	Objectives	5
I.3	Procedure	6
I.4	Outline of Thesis	9
II	LITERATURE REVIEW	11
II.1	Overall U-value - Analytical	12
II.2	Steady-state Single Heating Source - Analytical	13
II.3	Steady-state Dual Heat Source Superposition - Analytical	15
II.4	Transient Line Solution - Analytical	17
II.5	Transient Cylindrical Source - Analytical	17
II.6	Leg Spacing and Short Circuiting - Analytical, FD and FE	20
II.7	Transient Non-homogenous Media - FD and FE	23
II.8	Three Dimensional Analysis - FD and FE	24
II.9	Moisture Migration - FE	26
II.10	Literature Summary	33
III	FINITE ELEMENT HEAT TRANSFER EQUATIONS	36
III.1	Classical Second-order Two-point Boundary-value Problem	37
III.2	Time-dependence	39
III.3	Spatial Discretization	42
III.4	Complete Discretization in Time	49
III.5	Physical Significance of Terms	52
III.6	Computation of Matrices	52
III.7	Time-stepping Scheme Theory	52
III.8	Summary	53
IV	VALIDATION OF HEAT TRANSFER MODELS	54
IV.1	Overall U-value	54
IV.2	Single Source Heating	55
IV.3	Dual Cylindrical Source Heating	65
IV.4	Single Source Constant Temperature	66
IV.5	Dual Cylindrical Constant Temperature	69
IV.6	Summary	69

CHAPTER Page

V APPLICATIONS OF THE HEAT TRANSFER MODELS 70

V.1 Equivalent Diameter 70
V.2 Short Circuiting and Equivalent Diameter 76
V.3 Backfill (Non-homogenous properties) 93
V.4 Case Study: Comparison with Mei Experiment 101
V.5 Multi-pipe Installations 104
V.6 Summary 106
V.7 Conclusion on Equivalent Diameter 108
V.8 Further Work 108

VI FINITE ELEMENT HEAT AND MASS TRANSFER EQUATIONS . . 109

VI.1 Phillip and de Vries Model 109
VI.2 Hampton: FE with Moisture 110
VI.3 Heat Transfer Equation 110
VI.4 Water Transport 119
VI.5 Summary 125

VII VALIDATION OF HEAT AND MASS TRANSFER MODELS 127

VII.1 Model Structure 127
VII.2 Non-linear Model Calibration Variables 128
VII.3 Validation and Application 132
VII.4 Summary 133

VIII APPLICATION TO GCHP SYSTEM DESIGN 136

VIII.1 Sizing Criteria 136
VIII.2 Application of Heat Transfer Models 137

IX CONCLUSIONS AND RECOMMENDATIONS 147

IX.1 Recommendations 150

REFERENCES 151

APPENDIX

A FINITE ELEMENT METHOD 157

A.1 Finite Element Method 158

APPENDIX Page

A.2 Master Element 158
A.3 Element Map T_e 159
A.4 Shape Function Interpolation 161
A.5 Quadrature Integration 163
A.6 Conclusion 165

B FINITE ELEMENT HEAT TRANSFER CODE FLOW CHART 166

B.1 PART I- Four Components 166
B.2 PART II- Subroutine Tree 166
B.3 PART III - Subroutine Applications 168

C FINITE ELEMENT HEAT TRANSFER AND MOISTURE CODE FLOW CHART 174

C.1 PART I- Four Components 174
C.2 PART II- Subroutine Tree 175
C.3 PART III - Subroutine Applications 177

VITA 185

LIST OF TABLES

Table		Page
1	Sophistication of various models	34
2	Paramcters and results for different temperature scurces	87
3	Thermal effectiveness as a function of separation and temperature	94
4	Thermophysical data for non-homogenous grid	98
5	Properties for simulating Mei's experiment	103
6	Comparison of author's model with various models	134
7	Earth loop size by configuration and soil type.	144
8	Cost vs bore hole width	145
9	Consumption and bore hole cost	145
10	Cost vs backfill thermal conductivity	146

LIST OF FIGURES

Figure		Page
1	Typical heat pump system in cooling mode with three vertical series U-tube loops	3
2	Ground heat exchanger cross section showing the two tubes of a U-tube with backfill	4
3	Non-dimensionalization parameters	8
4	Design methods of experience, steady-state, transient and non-linear	12
5	Steady-state single source heating in a Claesson grid	14
6	Steady-state dual source heating with Claesson grid coordinates	16
7	The double two-coordinate system	25
8	Thermal dry-out curves for (a) resistivity and (b) conductivity.	28
9	Soil triangle of the basic soil textural classes.	29
10	Overall heat transfer coefficient (UA) for constant temperature source in FD and FE models	55
11	FE mesh for twin cylinders with three nodes per element (0-10r_o in grid of 1600r_o where r_o =0.0133 m)	56
12	FD constant heat stair-step approximation of circular pipes with one node per element (0-3r_o in grid of 400r_o)	57
13	Transient constant heat source temperature	59
14	Steady state constant heat source temperature	60
15	Excess error for FE and FD	61
16	Transient finite element boundary size temperature accuracy	62
17	Transient FD boundary size temperature accuracy	63
18	Number of nodes vs accuracy in 100 radii models	64

Figure		Page
19	Dual heat source models for FE and FD	66
20	FD constant temperature stair-step approximation of circular pipes ($0\text{-}3r_o$ in grid of $400r_o$)	67
21	Transient single source constant temperature (35°C) for FD and FE	68
22	Boundary condition on surface	72
23	Boundary condition on cross sectional area	72
24	Heat transfer as a function of time and radius	73
25	Grid for two constant heat sources	75
26	FE mesh grid with nine available source locations	77
27	Use of quadrilateral four-node elements to extend grid	78
28	Non-dimensional separation parameters, $x_{sep} = (x + 2r_o)/r_o$ and l/D_o	79
29	Separation parameters for one-inch nominal pipes (2.7cm o.d.)	80
30	Thermal effectiveness and thermal short circuiting vs separation distance and grid size	82
31	Concentric cylinder model for geometric equivalent radius r_{eqv} of two sources	83
32	Equivalent radius, $r_{g,eqv}$, of similar sources	84
33	Equivalent heat flux radius $r_{h,eqv}$ of similar sources	85
34	Thermal effectiveness ε_Λ for different sources (above) transient and (below) steady-state	88
35	Transient geometric equivalent radius $r_{hi,g,eqv}$ for different sources	89
36	Steady-state equivalent geometric radius $r_{hi,g,eqv}$ for different sources	90
37	Steady-state heat flux equivalent radius $r_{h,eqv}$ for different sources	90

Figure		Page
38	Effect of farfield temperature on thermal effectiveness	92
39	Effect of coil temperature difference on thermal effectiveness	93
40	Thermal effectiveness as a function of separation and temperature	94
41	Energy balance for the homogenous nine-source model at various radii	95
42	Non-homogenous material composition	96
43	Thermal conductivity of bentonite grouts	97
44	Net heat dissipated in the soil	99
45	Heat flux equivalent radius $r_{h,eqv}$	100
46	Thermal effectiveness	101
47	Backfill effectiveness	102
48	FE grid to simulate Mei's experiment	103
49	Transient equivalent radius simulating Mei's experiment.	104
50	Flat and bundle multi-pipe arrangements	105
51	Typical four pipe FE grid.	106
52	Steady-state heat transfer ratio of four pipes vs two pipes	107
53	Control volume for water flow in x-direction.	121
54	Comparison of water content changes when suction pressure increased.	122
55	Volumetric water content (VWC) vs suction pressure.	130
56	Suction pressure vs hydraulic conductivity.	131
57	Heat transfer for various water contents and operation modes	132
58	Backfill effectiveness for various water contents and operation modes	133

Figure		Page
59	The FE structures of preprocessor, processor, time loop, and post processor	157
60	Quadrilateral linear mapping.	159
61	Triangular linear mapping.	160
62	Transformation of quadrilateral area elements	161
63	Nine node shape functions	162
64	Nine-point Gauss quadrature rule integration points and weights.	164
65	The FE structure of preprocessor, processor, time loop, and postprocessor	166
66	Subroutine sequences in QT	167
67	The FE structure of preprocessor, processor, time loop, and postprocessor	174
68	Overall subroutine sequences in QM	175
69	Time loop subroutine sequences in QM	176

CHAPTER I

INTRODUCTION

Heat pumps provide cooling and heating to residences. The condenser in cooling mode operation for a heat pump is usually either a refrigerant-to-air heat exchanger (used in air-source heat pumps (ASHP)) or a refrigerant-to-water heat exchanger (used in water source heat pumps (WSHP) and ground-coupled heat pumps (GCHP)). In a GCHP, the water from the refrigerant-to-water heat exchanger is circulated through tubing in the ground. ASHPs are the most common heat pump for residential applications. WSHPs are primarily used for commercial building applications. GCHPs offer three potential advantages over an ASHP. First, GCHPs replace the outdoor fan with a fluid-circulating pump and eliminate the outdoor coil frost and defrost losses. Second, the GCHP heat exchanger can have better heat transfer because water is a superior heat transfer media than air. Third, and most significantly, the ground temperature is closer to that desired for human comfort than the outside air during extreme heat or cold. While outdoor temperatures change hourly, ground temperatures below nine meters are relatively constant all year. In Texas, summer daytime air temperatures often reach over 38°C. In contrast, soil temperatures vary from 16°C to 27°C, depending on location in the state (Gonzalez, 1993).

Models of GCHPs performance can be used to optimize designs for adequate capacity while not incurring excessive pipe lengths. Unfortunately, each of the three theoretical GCHP advantages can be negated if not designed properly. Designing a GCHP installation is much more difficult than an ASHP or conventional air conditioner. Hence, the potentials for increased efficiency must be optimized for suitable applications with appropriate evaluation tools.

The style and format for this dissertation conforms to that of the *ASME Journal of Heat Transfer.*

Water-source heat pumps have been produced in the United States for over 30 years. These systems are used in residences, commercial buildings (offices etc.), and institutional buildings such as schools, nursing homes, and hospitals. The development of reliable underground plastic piping technology with a long life led to the emergence of closed-loop systems. In 1987, water-source heat pumps comprised 3.4% of the commercial air-conditioning industry with a strongly upward 10-year trend in market share (Pietsch, 1990).

GCHPs are classified into horizontal and vertical systems. In vertical loops, the three primary configurations are the U-tube, divided tube, and concentric tube. This study examined vertical U-tube configurations because these are the most popular units (Bose, 1985).

Figure 1 shows a typical vertical U-tube GCHP cooling cycle. Energy is extracted from the conditioned space by the refrigerant and transferred to water in a refrigerant-to-water heat exchanger. The energy is then transferred to the ground via the water that flows through vertical U-tubes in the ground. During the winter, the cycle is reversed and the heat pump operates in the heating mode by extracting heat from the soil. Ground coil performance and capacity are determined by the amount of heat dissipation (or absorption when heating).

Heat pump system components must be matched with predicted energy use and demand. The complexity of the heat transfer problem eludes an exact analytical solution. Experimental testing by trial and error is cost prohibitive. As a result, numerical models can be used to predict heat transfer to/from the ground coil.

A ground-source system installer must have accurate building cooling loads, soil property data, weather data (both monthly bin and design temperature determination), and specifications for a variety of manufacturers' heat pumps. Also of importance is calculation of entering water temperature to the heat pump to allow estimation of energy use.

The ideal model would have to predict how soil thermal properties, soil density, soil moisture content, soil temperature distribution, heat exchanger material, pipe diameter, heat exchanger fluid properties, fluid film resistance, and thermal contact

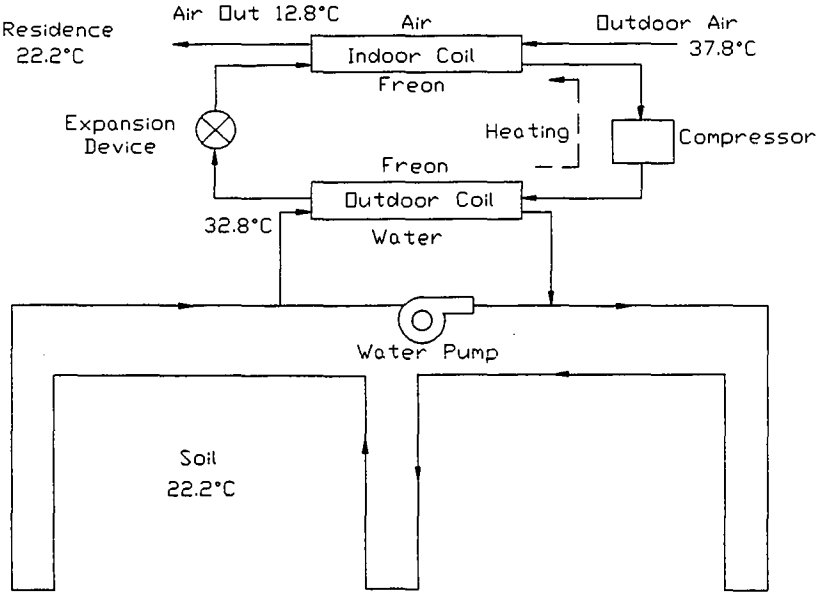

Figure 1. Typical heat pump system in cooling mode with three vertical series U-tube loops

resistance between the pipe and the soil impact the performance of the heat exchanger (Cane and Forgas, 1991). In addition, accurate predictions of ground-source heat pump performance require accounting for the effects of equipment cycling, seasonal earth temperature changes, and heat exchanger surface temperatures below freezing. No method exhaustively accounts for all these factors, and many oversimplify the heat transfer process to obtain solutions that are are mathematically tractable and readily accommodated in building energy analysis software. In particular, many two dimensional models approximate the dual cylindrical source using a single Kelvin line source solution (Cane and Forgas, 1991). Unfortunately, short cuts can lead to uneconomical heat exchanger lengths or misrepresent the energy performance of such systems.

I.1 Challenges of Cooling-dominated GCHPs

This investigation examined the modeling of cooling-dominated vertical U-tube GCHPs. The associated major challenges can be outlined as follows.

Thermal interference between the two pipe legs results in unsymmetric boundary conditions. Figure 2 shows the relative position of the two tubes. As a further complication, some installations use more than two coils in the same trench to cut costs.

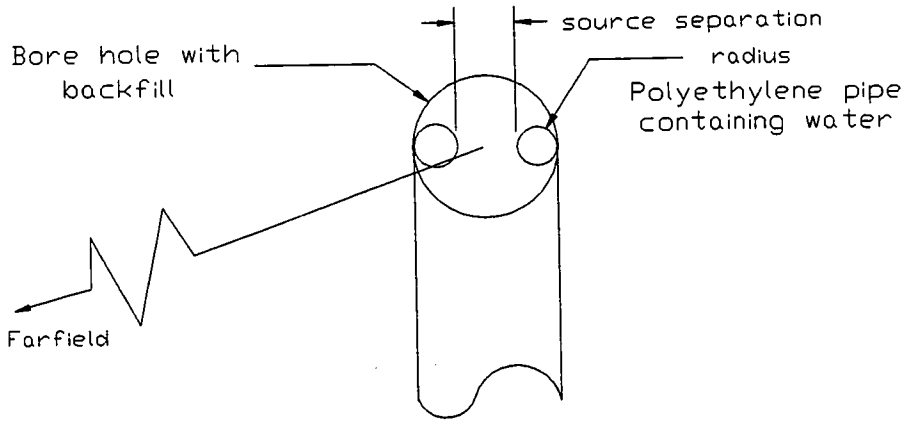

Figure 2. Ground heat exchanger cross section showing the two tubes of a U-tube with backfill

GCHP capacity varies with time during the course of an on-cycle. During the off-cycle, water in the ground has more time to approach the lower ground temperature. This leads to better start-up performance. The cumulative effect of on-cycle heat rejection is an increase in the surrounding ground temperature. Some sufficiently cooling-dominated sites have documented a net seasonal increase in soil temperature (De Lange, 1988).

GCHP performance is also a function of soil thermal properties which vary with location, depth, and time. In sufficiently cooling-dominated regions, the soil

temperature will increase during the cooling season. This can decrease the net seasonal moisture content near the ground heat exchange (Couvillion and Cotton, 1990). Long term heating can "bake" the soil. While moisture apparently cannot be ignored, the effect could be minimized by the use of backfills that are insensitive to moisture migration or by having adequate water content. In addition, there is hysteresis in the moisture curve (thermal conductivity as a function of water content) depending on whether the soil is drying or wetting. Most notably in high clay content soils, heating can cause drying and soil shrinkage, which results in air gaps and reduces the thermal conductivity of the soil. In the power industry, this phenomena has led to the placement of high conductivity backfills around buried electrical power cables. These backfills are insensitive to moisture migration. However, the current bentonite backfills used by the heat pump industry are generally poor conductors (Remund and Lund, 1993).

I.2 Objectives

The numerical investigation had three objectives: (1) to quantify short circuiting through parametric analysis, (2) to examine the effect of backfills, and (3) to compute performance degradation from moisture migration.

First, a transient conduction finite element model was needed for running the single line-source and cylindrical-source. The two configurations had existing analytical solutions (Ingersoll et al, 1948) and many studies had used these simplified solutions. The numerical model should optimize dual cylinder pipe leg spacing to balance wider bore hole costs and thermal short-circuiting of "hot" and "cold" legs. The model should also examine the effect of different backfill materials on the heat transfer. Consequently, the above studies should be combined to develop a reliable method for analyzing heat transfer and post-processing performance for use as an algorithm tool for installing heat pumps. Finally, a preliminary investigation of the coupling of the conduction model with moisture migration should be conducted.

I.2.1 Simulation Requirements

The GCHP project at Texas A&M University required development and validation of a computer code to quantify performance at variable pipe leg spacing for different backfill materials and declining soil moisture content. The algorithm had to interface with hourly building loads and weather data to predict the long term performance of a ground source heat exchanger of a GCHP. Soils in Texas range from relatively dry and granular in West Texas to nearly saturated on parts of the Gulf Coast. Soil thermophysical properties determine the size of the ground-coupled heat exchanger.

The model required five attributes:

- Finite element simulation to handle physical phenomena and complicated geometry. Galerkin weighted residual pseudofunctional method of triangular and/or rectangular elements,
- 2-D for either vertical and radial or horizontal cross section,
- Transient performance,
- Accessible (obtainable, machine compatible, modifiable to Texas data), and
- Inputs of soil type, density, temperature, and/or moisture.

I.3 Procedure

I.3.1 Single Cylinder Constant Heat or Temperature Conduction

The first phase was to construct a transient conduction finite element model and simplify the actual GCHP network to simple configurations with known analytical solutions. First the line-source was compared with the steady-state solution of Claesson and Dunard (1983). The cylindrical finite element (FE) model examined the representative horizontal cross section of Figure 2 with a unit vertical depth of one foot. The heat flux for the typical cross section was the average hourly heat output divided by the total pipe network length. The 1-D radial single cylinder homogeneous transient geometry was then verified with the Ingersoll et al (1948) solutions for constant heat flux and temperature boundary conditions.

After verifying the model in a geometry, the model was extended to simulating the complex array of underground double (supply and return) pipes plus a backfill material (Figure 1).

I.3.2 Two Cylinder Leg Spacing and Backfill Materials

Several mesh models of different pipe leg spacings were run to quantify the thermal interaction between the two legs. The resulting thermal short circuiting was analyzed to answer two questions:

- What is the equivalent radius of a single cylindrical heat source?
- What is the associated effective heat transfer rate?

After validating the single cylinder conduction model, a second cylinder was added. The supply water cylinder tube became the "hot" leg while the return cylinder was the "cold" leg. The parameters for temperature and heat are shown in Figure 3. This study examined overall performance for different spacings and backfill materials. Results were generalized to allow GCHP installers to examine a wide range of configurations. The dimensionless temperature and dimensionless heat effectiveness were defined, respectively, as follows:

$$\varphi_T = \frac{T_{hi} - T_{lo}}{T_{hi} - T_{ff}} \text{ and } \varepsilon_\Lambda = \frac{Q_{1+2,net}}{Q_{1,isolated} + Q_{2,isolated}}. \quad (1)$$

Heat dissipation at selected leg spacing distances was compared with other numerical models as well as experimental monitoring sites. Available comparisons included the steady-state analytical line-source of Claesson and Dunard (1983) and the transient finite difference (FD) Texas A&M University model of Dobson (1991).

The soil physics literature examined included initial thermophysical soil data, separate backfill materials, variable soil properties, and moisture transport.

I.3.3 Moisture Migration

The third and final procedure evaluated coupling moisture transport with conductive heat transfer. The merits of including moisture in a variety of operation

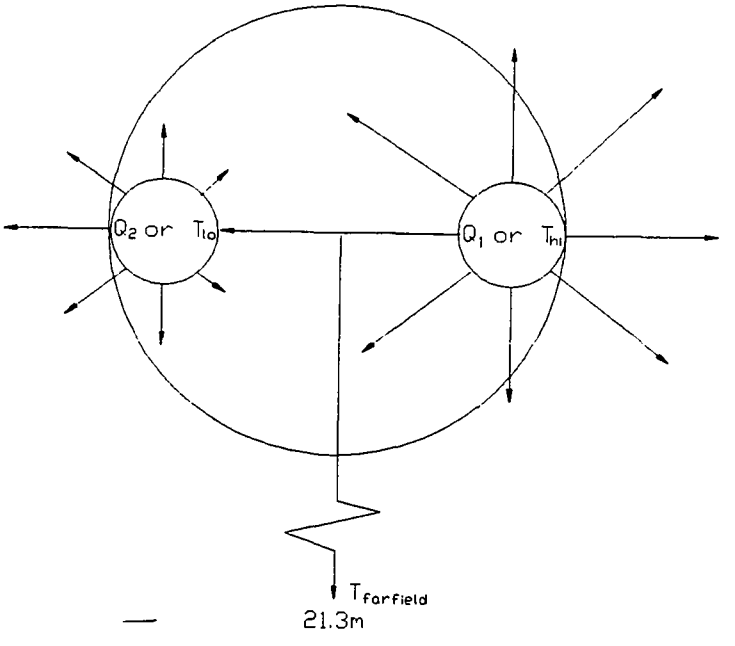

Figure 3. Non-dimensionalization parameters

scenarios are discussed with data collated from different studies. The difficulties, uncertainties, and additional computing resources are also identified. A "simultaneous" solution method is achieved by iterative sequential solutions of heat and moisture at each time step. The model must be run long enough in a predominantly cooling mode to reach the "critical moisture" level. This is the moisture content at which the relatively flat nature of the thermal dryout curve gives way to a disproportionate increase in the thermal resistivity.

I.3.4 Model Verification

The final model achieved the intended goal of establishing a procedure to quantify deterioration of the heat exchanger over time. The final model inputs were the soil properties (type, density, moisture content, and porosity) as a function of depth.

Limited verification of the model was done using data from other experimental studies. Only limited coil water and soil temperature data were available at the Texas A&M University sites. Some of the sites had already documented net seasonal temperature increases in the vicinity of the tubes. However, moisture content was not monitored.

Analytical and numerical verification was also done with indirect comparisons with other experiments and numerical models. To the author's knowledge, no other GCHP model adequately accounted for thermal short-circuiting or coupled heat and moisture transport. The closest models to this GCHP study were the double coordinate system finite difference model (Lei, 1993) and a backfill finite element model for heat and moisture (Couvillion and Cotton, 1990).

I.3.5 Alternative Numerical Schemes

Three models were utilized as secondary numerical schemes. ANSYS and Intergraph I/EMS are packaged systems which allow three-dimensional modeling, but less control of equations and theory. CONDUCT is a general transient finite difference method developed by Suhas V. Patankar (1991). The model shell has built in subroutines to ease grid setup. In addition, each problem requires coding modifications of appropriate subroutines. CONDUCT roughly modeled cylindrical conduction problems, but did not have the power of FE to model complex geometry, input complex equations such as those for moisture transport, or handle variable loading.

I.4 Outline of Thesis

This dissertation first introduced GCHP modeling, then discussed pertinent literature, and finally developed FD and FE simulation models. Chapter II examined existing analytical and numerical heat pump models in ascending order of complexity. The remaining chapters consisted of FE analysis. Chapter III outlined development of the heat transfer code QT (heat and temperature). The chapter began with the variational calculus equation and developed the heat flux finite element model. Next,

Chapter IV validated the FE and FD heat flux models against analytical cylindrical-source solutions. The error analysis examined accuracy, CPU time, convergence, and stability. The validated model was then used for heat pump case studies in Chapter V: *Applications of Heat Transfer Model.* The primary topics were equivalent diameter, thermal short circuiting, and backfill conductivity. The next two chapters incorporated mass flow. The associated moisture transport equations were derived for coupled non-linear heat and mass transfer in in Chapter VI. In Chapter VII, heat and mass transfer case studies were performed to validate the model and quantify the effect of moisture on heat pump operation. Next, *Application to GCHP System Design* was done in Chapter VIII. The design theory was reduced to practical field situations and costs. Finally, conclusions and recommendations were made in Chapter IX.

Three appendixes supported this thesis. Appendix A outlined the fundamental FE method and elements mutual to both heat and mass transfer. Then the flowcharts are contained in Appendix B for the heat transfer code, and Appendix C for the heat and mass transfer code.

CHAPTER II

LITERATURE REVIEW

This investigation concentrated on the vertical U-tube configurations, but when necessary, useful information was also extracted from horizontal configurations. GCHP design methods ranged from design experience, to utilizing numerical methods to predict steady-state, transient, and non-linear performance (Figure 4). This thesis examined the three common approaches to modeling heat exchange in the ground loop: (1) analytical solutions, and (2) numerical models of (a) finite difference (FD) and (b) finite elements (FE). Literature was collated to develop nine sequential levels of complexity in modeling ground heat exchange.

1) Overall U-Value -*Analytical*

2) Steady-State Single Source -*Analytical*

3) Steady-State Dual Source Superposition -*Analytical*

4) Transient Line Source -*Analytical*

5) Transient Cylindrical Source -*Analytical*

6) Leg Spacing and Short Circuiting -*Analytical, FD and FE*

7) Transient Non-homogenous Media -*FD and FE*

8) Three Dimensional Analysis -*FD and FE*

9) Moisture Migration -*FE*

All nine stages are listed with their documented or proposed solutions. The selection of application depended on the required accuracy versus computational

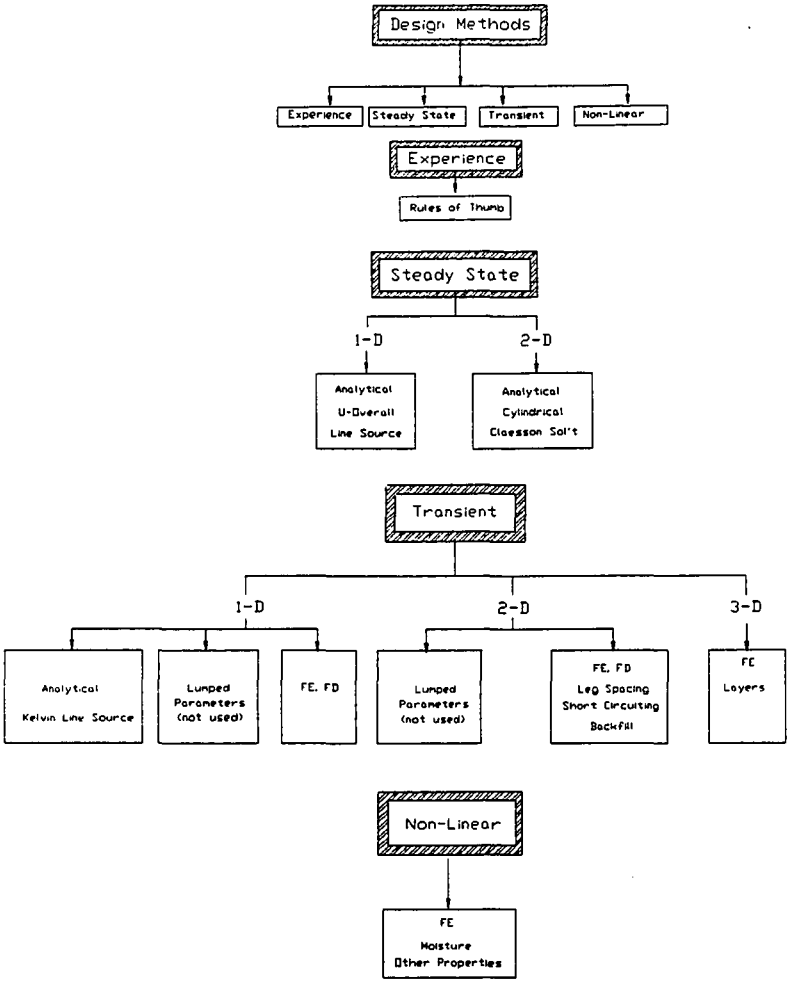

Figure 4. Design methods of experience, steady-state, transient and non-linear

effort.

II.1 Overall U-value-*Analytical*

The most basic means of modeling the ground-coil consisted of using an overall heat transfer coefficient, (also called a U-Value). A study of fractional on-times

by Braud et al (1983) calculated U-values for vertical U-tube, vertical concentric tube, and horizontal heat exchangers. Their results showed a U-value asymptotically decreasing by a factor of three over several hours. In addition, lowering the fractional on-time from 100% to 25% raised the U-value by 2.54 times. As a result, they concluded that the the large variation in U-values was evidence that the method was too simple to capture the complexity of transient heat transfer.

The U-value method offered insight into how the heat transfer of the ground-coil varied over long time periods. Because a typical heat pump cycle is on the order of ten to twenty minutes, this method was clearly unsuitable for predicting short term heat transfer.

II.2 Steady-state Single Heating Source - Analytical

Steady-state solutions offer quick simple insight into long-term performance by calculating the base load contribution to the total thermal process.

Figure 5 represents steady-state heating by a single pipe in the ground. The center of the pipe was at (x,y)=(0,d). The rate of heat extraction from the ground to the pipe per unit length of the pipe was $\dot{Q}'$. The negative value of $\dot{Q}'$ in Figure 5 indicated that heat is flowing from the pipe to the ground.

Backfill was ignored and the ground was assumed to be homogenous with a soil thermal conductivity of k. Therefore, the steady-state temperature $T(x,y)$ satisfied the Laplace equation $\partial^2 T/\partial x^2 + \partial^2 T/\partial y^2 = 0$. If the temperature at the ground surface $y = 0$ was arbitrarily set to zero, then the solution $T(x,y)$ represented the excess temperature field due to the heat sink $\dot{Q}'$.

The temperature due to a single line source in an infinite homogenous medium with conductivity k can be derived using the cylindrical Fourier's law. The rate at which energy was conducted across the pipe cylindrical surface into the solid soil was expressed as

$$\dot{Q}_r = -kA\frac{dT}{dr} = -k(2\pi rl)\frac{dT}{dr}, \tag{2}$$

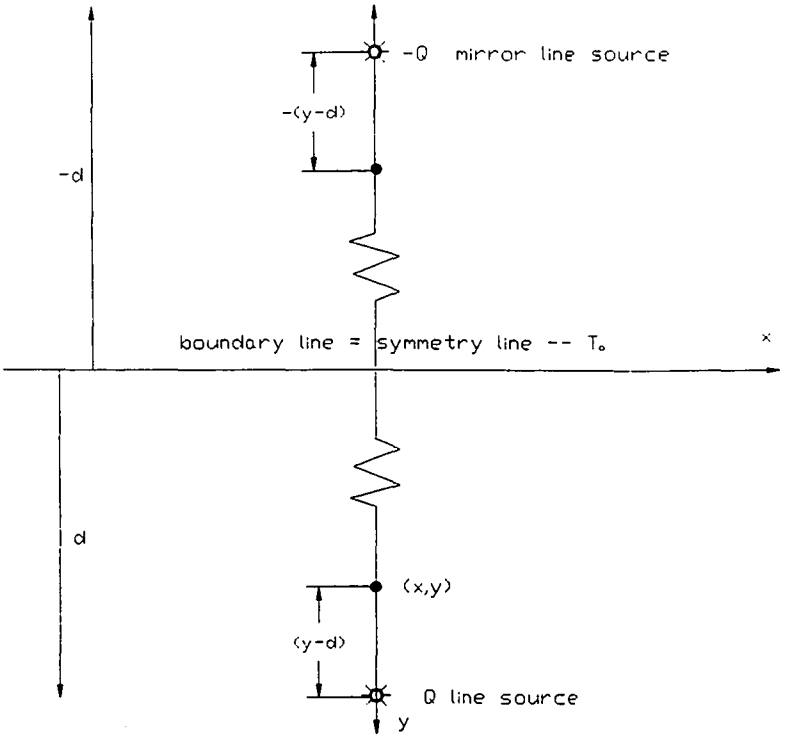

Figure 5. Steady-state single source heating in a Claesson grid

where $A = 2\pi rl$ is the area normal to the direction of heat transfer. Assuming a constant k, simple integration can be performed to yield

$$T - T_o = -\frac{\dot{Q}}{2\pi kl} ln(r), \tag{3}$$

where r is the distance from the line source, and T_o is the reference temperature. This is the line solution because it used a point source.

Claesson and Dunard (1983) suggested a simple "mirror source" method of using the analytical line source to verify two-dimensional numerical models. The key point was to satisfy the condition of zero temperature (T_o) at the boundary $y = 0$. Figure 5 shows that the temperature distribution can be simulated by having two

opposite sources (dipoles) equidistant from the line of symmetry. The basic solution of temperature T was given as:

$$T(x,y) = T_0 + \frac{\dot{Q}_1}{2\pi k} \cdot \ln\left(\frac{\sqrt{x^2+(y-d)^2}}{\sqrt{x^2+(y+d)^2}}\right). \tag{4}$$

Here, $\dot{Q}$ was the heat generation per unit length. The numerator of the arguement of the logarithmic term of the equation was the distance from (x,y) to the line sink at $(0,d)$, while the denominator was the distance to the mirror source at $(0,-d)$. A line source approximated a cylindrical source at large distances. Therefore, the accuracy of the line source depended on the validity of the assumption that the radius r_o was much smaller than the depth d ($r_o \ll d$).

In numerical simulations, the "mirror" half was not modeled so the distance from the mirror line source to the boundary was d. Numerical cylindrical source results should approach those of the line source with larger grids as d becomes much larger than r_o.

II.3 Steady-state Dual Heat Source Superposition - Analytical

The next stage in improving GCHP modeling was adding a second cylindrical pipe. The overall performance in a two-coil trench was difficult to determine because of the thermal interference between the different sources. To the author's knowledge, the only known accepted analytical solution was for the simplified steady-state line-source of Claesson and Dunard (1983). This traditional line-source mirror-image approach has two major limitations. First, the actual problem was cylindrical and not a line. Second, the heat transfer transient response time scale is on the order of days rather than seconds or minutes.

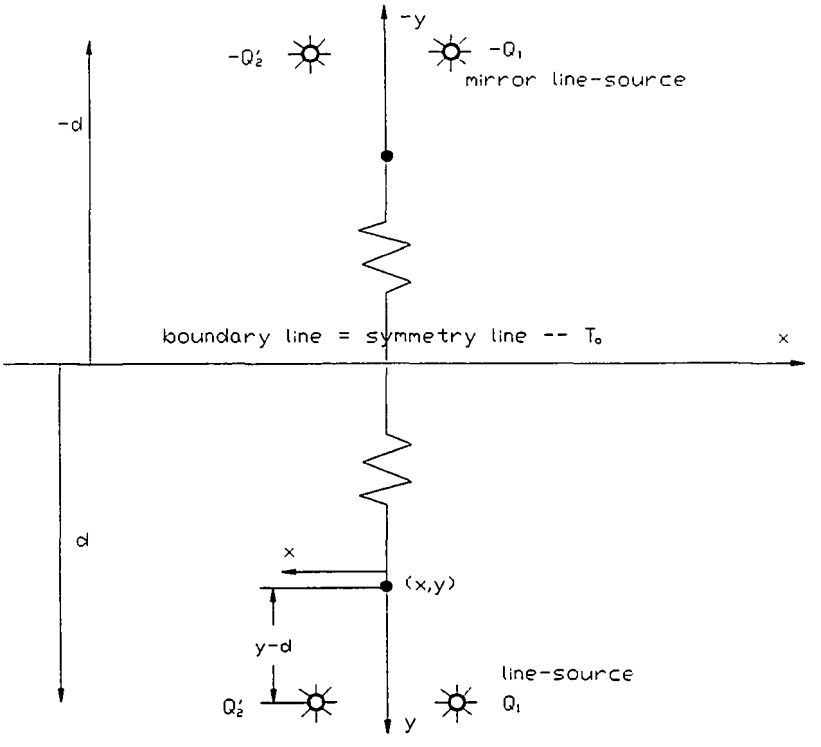

Figure 6. Steady-state dual source heating with Claesson grid coordinates

Figure 6 depicts two parallel pipes in the ground. The two pipes lie at points (x_1, d) and (x_2, d). The distance between the pipes is B, and the respective heat extraction rates are Q_1 and Q_2.

Claesson and Dunard (1983) used superposition to extend their single source solution to a dual source solution.

$$T(x,y) = T_0 + \frac{Q_1}{2\pi k} \cdot \ln\left(\frac{\sqrt{(x-x_1)^2+(y-d_1)^2}}{\sqrt{(x-x_1)^2+(y+d_1)^2}}\right) + \frac{Q_2}{2\pi k} \cdot \ln\left(\frac{\sqrt{(x-x_2)^2+(y-d_2)^2}}{\sqrt{(x-x_2)^2+(y+d_2)^2}}\right) \tag{5}$$

They used the same assumptions as in Equation 4 and the grid in Figure 6.

II.4 Transient Line Solution -*Analytical*

The simplest transient analytical solutions approximated the cylindrical pipe as a line-source. As in the single source problem, Claesson and Dunard (1983) also extended the dual Kelvin line-source to examine pulses, periodic variations, ground water flow and infiltration, as well as variations of temperature/heat and pipe configurations (three-pipes, etc.). With some effort, these basic methods can be applied to the cylindrical heat exchangers used with GCHPs. However, inaccuracies occurred when simulating a pipe of finite radius for short time periods, since the heat takes a finite amount of time to travel from the imaginary line-source to the actual radius. Consequently, for thermal properties of most soils, the line-solution was limited to time scales of hours, days, and years, rather than minutes. Designs based on the line-solution must use a conservative estimate of longer and more expensive coil than was actually needed.

II.5 Transient Cylindrical Source -*Analytical*

Carslaw and Jaeger (1940) analyzed a finite diameter pipe in an infinite medium. They developed one-dimensional radial solutions using Laplace transforms. The work included a constant pipe surface temperature and a convective boundary condition, with both constant and arbitrary initial temperature profiles. The solutions were complicated indefinite integrals of Bessel functions. Jaeger (1942) solved these equations and gave numerical values for the cases of constant surface temperature, constant heat flux, and convective boundary conditions with constant initial temperature. Jaeger (1942) also derived the general boundary condition for a perfectly conducting fluid that was either at rest or flowing inside a pipe.

The only solutions derived by Carslaw and Jaeger (1940) which have been used in later GCHP research were those repeated by Ingersoll et al (1948). He transformed the solutions into more common heat transfer terminology, presented values for the integrals, and gave case studies of ground-coupling with constant heat or temperature boundary conditions.

The transient line solution was required in two-dimensional modeling involving the depth. Because depth was used for one of the coordinates, the horizontal plane could only be a function of radial distance. However, the cylindrical-source solution for constant heat flux reduced to the line-source solution for large values of the Fourier number ($\alpha t/R^2$). The associated line solution error should be less than 2% if the Fourier number is greater than 20. For a system with soil thermal properties of 1.73 W/(m-K) and a heat exchanger with radius of 0.01334 m, a Fourier number of 20 corresponded to a time of one hour. The temperature T in a medium at distance r from a permanent source with a strength per unit length of Q' at time t after release was

$$T - T_o = \frac{Q' r^{(2-n)}}{2\pi^{n/2} k} \int_{r\eta}^{\infty} \beta^{(n-3)} e^{-\beta^2} d\beta, \tag{6}$$

where

$$T_o = \text{ initial soil temperature, } \beta = \frac{r}{2\sqrt{\alpha(t-\tau)}}, \eta = \frac{1}{2\sqrt{\alpha t}},$$

and steady-state occurred only in the case of $n = 3$.

The cylindrical-solution yielded maximum accuracy in two-dimensional modeling of the horizontal plane. Jaeger presented equations for the constant heat flux and constant temperature problems. When a pipe transferred heat per unit length of Q', the temperature T at a given time and point (Z, R) was given by

$$T - T_o = \frac{Q'}{k} G(Z, R) = \frac{2\pi R Q''}{k} G(Z, R),$$

where the function $G(Z, R)$ is

$$G(Z, R) = \frac{1}{\pi^2} \int_0^{\infty} \frac{e^{-\beta^2 Z} - 1}{J_1^2(\beta) + Y_1^2(\beta)} [J_o(R\beta) Y_1(\beta) - J_1(\beta) Y_o(R\beta)] \frac{d\beta}{\beta^2},$$

$$Z = \frac{\alpha t}{r_o^2} \text{ and } R = \frac{r}{r_o}. \tag{7}$$

An equation for *constant surface temperature* assuming a long pipe was also presented by Jaeger. The time rate of heat exchange per unit length Q' for a pipe held at constant temperature ΔT deviation from the initial soil temperature was given by

$$Q' = k\Delta T F(Z),$$

where the rate of heat transfer per unit area Q'' was

$$Q'' = \frac{k\Delta T}{2\pi R} F(Z)$$

and

$$F(Z) = \frac{8}{\pi} \int_0^\infty \frac{e^{-\beta^2 Z}}{J_0^2(\beta) + Y_0^2(\beta)} \cdot \frac{d\beta}{\beta}. \tag{8}$$

Ingersoll et al (1948) solved Equations 7 and 8 to produce tables with values of $G(Z, R)$ and $F(Z)$. These heat equation solutions for constant heat flux and temperature were the fundamental verification for all heat transfer models developed in this thesis.

II.5.1 Numerical Models Using Finite Difference

De Lange (1988) modeled a cylindrical heat source and validated the results with an operating system. He used a very simplified 2-D finite difference model and ignored moisture migration.

Deerman (1989) used the unsteady constant heat flux cylindrical-source equation of Ingersoll et al (1948) and predicted heat-pump entering water temperatures for hourly increments for two field-monitored, vertical U-tube GCHPs. His start-up analysis over the first 30 minutes was erroneous because he ignored the thermal mass of the water in the ground-coil.

II.5.1.1 Dobson: Start-up FD With Superposition

Dobson (1991) performed an experimental and analytical study of the transient behavior of a vertical U-tube GCHP. A three-ton GCHP was installed at Abilene,

Texas, and monitored via a remote data acquisition system on time intervals of one to 30 minutes.

Dobson developed an unsteady finite difference cylindrical constant heat source equation based on the solution of Ingersoll et al (1948). The required inputs were building structure and GCHP characteristics, soil properties, undisturbed soil temperatures, and outdoor air temperatures. The ground-coil was meshed with discrete elements. The principle of superposition accounted for thermal interference from the adjacent leg of the U-tube and transient variations in the the heat flux.

The model predicted the average entering water temperature (EWT) over five days to within 0.3°C, but also over-predicted the decreased EWT at the beginning of a cycle by 0.6 to 1.1 °C.

Three of Dobson's recommendations deserved particular attention. First, frequent cycling and long off-times were found to have a positive effect on all performance variables, and increased the efficiency by as much as 5%. Secondly, he stated that the effect of varying the spacing between adjacent legs of the U-tube should be quantified and related to GCHP installations. Third, he also recommended that an attempt be made to find a single analytical solution to the cylindrical constant heat source valid over the entire coil rather than on an elemental basis. Another interesting conclusion from page 135 of his study was that

> Comparisons of far-field soil temperature to outdoor air temperature, which are frequently cited as an advantage of GCHPs over ASHPs, are irrelevant and in the case of the data from this study, misleading. (Dobson, 1991)

II.6 Leg Spacing and Short Circuiting -*Analytical, FD and FE*

Only limited and sketchy information was available on the thermal short-circuiting of pipe legs for GCHPs. An equivalent diameter approach was originally suggested by Bose (1984) as well as Claesson and Dunard (1983) to account for thermal *short circuiting* between pipe legs.

In an experimental study. Mei and Baxter (1986) operated a vertical GCHP with six dissimilar U-tube coils in series for heating, cooling, and controlled tests. Each U-tube was isolated and studied individually and corporately to test the validity of the equivalent diameter approach (i. e., $D_{eq} = C \cdot D$, where C was a correction factor). They statistically determined that the C-values for the six pipes varied from a minimum of 1.0 to a maximum of 1.622. The original C-value of $\sqrt{2} = 1.414$ suggested by Bose (1984) as well as Claesson and Dunard (1983) was within this range. The average equivalent radius was 1.3 times the coil radius, which was very close to the original C-value, but significantly different from the 1.8 value of Fischer and Newman (1981). Because their work yielded such a large scatter in equivalent diameter correction values, Mei and Baxter concluded the equivalent diameter method could not be used with a high degree of confidence. In addition, their study's validity was limited by several applications. The C-value was determined by iterating values in a FD code to calculate the Reynold's number correlation for the convective heat transfer assuming a constant water flow rate. The value was assumed correct when the experimental exit water water temperature over five days was duplicated. Furthermore, the two tubes were only separated by rubber insulation. This configuration is rarely used and (Mei, 1988) admitted that the insulation "probably did more harm than good" because it reduced the heat transfer area.

Mei (1988) derived a finite difference mathematical model in cylindrical coordinates for two coils. The relevancy of Mei's study was limited for several reasons. It was limited to horizontal coils, only considered heating, and data were collected for only one month. Also, there were gravity and temperature gradient effects because of locating one pipe over the other in their double coil system. In addition, the computer model only cycled once per hour.

Each coil had three partial differential equations for the fluid, coil wall, and soil. The associated boundary conditions were for convection and conduction. Mei encountered difficulty in determining the soil thermal conductivity, due to wide variance within the trench. Comparison with experimental data for energy absorbed

by the ground yielded an average error of 12% and a maximum error or 27%. Results were more accurate for longer cycling time intervals. The advantage over the line-source was the energy exchange between the coil and the soil was calculated instead of assuming the strength of the source.

The model of Dobson (1991) included superposition, but only for a single leg. Therefore, a parametric analysis of leg separation distance could not be performed.

II.6.1 Deerman: Cylindrical With Corrections

Deerman (1989) relied on Ingersoll et al (1948) for constant heat flux unsteady solutions of the Kelvin line-source equation and the cylindrical-source equation. He predicted heat-pump entering water temperatures for both hourly and daily increments for two field-monitored, vertical U-tube GCHPs. Although both solutions yielded similar results over long time intervals, he concentrated on the cylindrical-source equation to get better accuracy in predicting short term temperatures. He kept the same limitations found in the original model of Ingersoll et al (1948). The model assumptions included:

- Heat transfer by pure conduction,
- Perfect soil and pipe contact,
- Soil acts as an infinite solid,
- No ground water movement, and
- No thermal interference from adjacent bore holes.

Deerman's work combined four components: equivalent diameters recommended by Bose (1985) and Mei (1988), standard heat transfer correlations, a correction factor for number of tubes, and short circuiting developed by Kavanaugh (1984). He used three correction factors to "force" the U-tube to overcome the limitations outlined for a *single, isolated*, pipe with a *constant* heat flux. He developed two "variations" of the method of superposition, which in effect discarded prior time interval contributions whenever their inclusion forced his model to deviate from the actual test results. His start-up analysis over the first 30 minutes was erroneous because he ignored the thermal mass of the water in the ground-coil.

II.7 Transient Non-homogenous Media -*FD and FE*

Heat pump installations are primarily non-homogenous because of backfill media which differs from the original soil. In addition, the soil properties vary with depth (3-D) and to a lesser degree with time and horizontally in the case of multiple bore holes. Other variances include the pipe material and contact resistances between the filler and the pipe or soil.

II.7.1 Backfill

Soil replacement after trenching should minimize contact resistance (Bose, 1985). One reference, (AIEE, 1960), stated that 20% of the earth's thermal resistance was in the first six inches of soil around the pipe. Backfill materials should posses high-conductivity and resist drying-out over time. The Texas A&M University installation sites in Abilene and College Station, Texas, used bentonite as a soil additives for particle bonding (with PVC or polyethylene pipes). Soil "binders" are often used to form thermal bridges between grains. Because "binders" do not evaporate or move when heated, they can increase soil thermal conductivities. However, many designers and installers of earth heat pump systems consider additional length and multiple pipes to be more economical considerations than backfill variations.

Several soil thermal improvement additives (for particle bonding) have been identified in the power cable industry and include:

- Moisture insensitive thermal products,
- Wax,
- Cement, and
- Non-swelling clays.

Couvillion and Cotton (1990) used a finite element model to solve heat and mass transfer for different backfill materials. Application of the study was limited to a horizontal GCHP. The numerical model considered moisture migration, varying soil properties, varying ambient conditions, varying load conditions, and backfill placement, size, and type.

Despite the "short" time period of 60 days, moisture migration decreased the effectiveness of the "un-binded" moist sand by 20%. Computer results slightly under-predicted the temperature response, but gave proportionally correct results in ranking four backfills for heat exchanger effectiveness (native soil at 14% moisture content, acrylic latex/sand, paraffin/sand, and worst of all moist sand).

II.8 Three Dimensional Analysis -*FD and FE*

Most of the two-coil thermal interference occurs in a two-dimensional (2-D) horizontal layer. However, the thermal conductivity, heat transfer, and temperature distribution also vary with depth. Unfortunately, the voluminous complexity of three dimensional elements in FD or FE renders analysis out the range of most researchers and computers. Frequently, 3-D problems are reduced to 2-D by approximating two coordinates with a line source. The line-source approximation will continue to be used widely until someone develops a more accurate, simple, and intuitive means of simplifying the three dimensional analysis.

Deng and Fedler (1992) examined the non-homogeneity effect of multi-layered soil on vertical heat pumps. A computer model was developed and validated for two-dimensional, transient, heat conduction. A hot copper tube was assembled in a three layered soil system comprised of coarse sand, clay, and fine sand. Heat transfer rates between soil layers was found to be discontinuous. The fine sand and coarse sand dissipated 27% and 62% more heat than the clay, respectively, over a 24 hour period. As a result, there was an initial vertical temperature gradient between the soil layers. However, the gradients decreased over time due to vertical heat flow.

Lei (1993) developed the double coordinate 2-D cylindrical system shown in Figure 7 to simulate the 3-D analysis. The finite difference model used cylindrical coordinates of radius and depth. Therefore, heat was assumed to only flow in the radial direction from each tube, except for the small region between the two coils. To

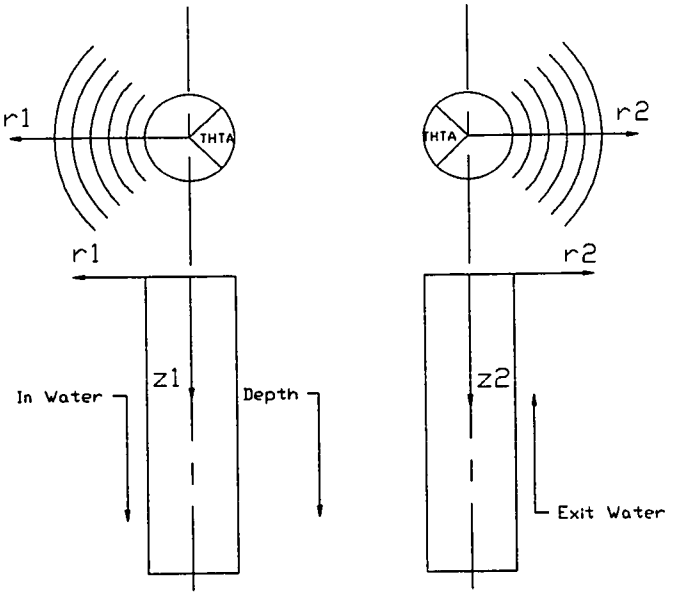

Figure 7. The double two-coordinate system

simulate interference in this region, Lei used the un-verified steady-state interference model of Hopkins (1983).

Lei's goal was to efficiently predict the outlet water temperature from a vertical U-tube ground-coupled heat exchanger. For verification, the test rig was run for 160 minutes. The exiting water temperature was monitored with a thermocouple in the fluidstream. Because the thermocouple was placed too close to the surface, there was no reading of the average off-time water temperature. However, for on-times, the numerical model error ranged from 0.2% to 5%. Lei also stated that the far-field infinity distance can be decreased from 9 meters to 5 meters with no effect. However, this was a trivial consequence of only running his experiment for 160 minutes. For his FD explicit scheme, he found the maximum time step increased with the square of the elementary grid size, Δr. At the heart of this model was the angle, θ, of each coil which was assumed to interact with the adjacent coil. The angle θ was a function of the geometric relation between the adjacent pipes and significantly affected the

net heat transfer to the soil. However, Lei did not suggest a selection method. A fit of the experimental data suggested a value of 90°. The model also needed to be modified to account for varying thermal conductivity.

II.8.1 Combined Slices of Pipe Length

Three dimensional heat transfer can be modeled using two dimensional grids. Mohammad-zadeh et al (1990) solved temperature fields in the earth by examining slices along the length of the heat exchanger. The top boundary condition was ambient temperature and solar insolation. The finite difference model was validated with experimental data over two months. The simulation computed the optimum size for a two-ton system. The model also verified that GCHP systems were not sensitive to changes in the water/earth heat transfer coefficient because the dominant resistance to heat transfer was ground conduction.

II.9 Moisture Migration -*FE*

II.9.1 Moisture Theory

One important potential impact on the performance of GCHPs was water transport. This study conducted a preliminary examination of the impact of including moisture with 2-D models. Water mass flow is the most difficult aspect of simulation due to highly non-linear terms. Therefore, accurate simulation required higher degree polynomial fits, thermal dry-out curves, and another set of boundary conditions for water content and/or flux.

II.9.1.1 Non-linear Soil Properties

Introduction of moisture migration required non-linear analysis of thermal conductivity, thermal dryout curves, and heat capacity.

II.9.1.1.1 Thermal Conductivity

There were three major factors in determining soil thermal conductivity (EPRI, 1989).

- Composition determined general thermal behaviour.
- Moisture content was the major influence on thermal conductivity (k = 5 - 10 W/°C·m), for a particular kind of soil. Soil composition is a mixture of solid mineral grains, air ($k \sim 0.022$W/°C·m), and water ($k = 0.61$W/°C·m). The thermal dryout curves were evidence of shifting from water to air in the spaces between soil grains.
- Density was taken to be constant since it did not generally change with time. However, the initial density should be verified, because density reduced the air pockets and improves conductivity especially in low moisture content curves.

II.9.1.1.2 Dryout Curves

Several thermal dryout curves were presented by the Electric Power Research Institute (1989) and a silty sand was reproduced in Figure 8. The Figure showed that the "knee" which signified a sharp change in thermal resistivity was not evident in the conductivity curve. All soils resistivities exhibited a concave shape, but varying degrees of sharpness in the "knee". The factors influencing the shape of the curve for a given soil composition were:

- higher dry density results in higher conductivities at low moisture content,
- higher organic content results in lower conductivities at higher moisture contents,
- angular soil grains have higher conductivities, and
- uniform grain size lowers the conductivity.

The three basic soils (sand, clay, and silt) are shown in Figure 9. Subjecting sands to a heat source results in drying and low conductivity due to their round grains and open structure. A typical conductivity change was from 1 to 0.33 W/4°C·m. The "critical moisture" was the sharp "knee" in the thermal dryout curves (such as in Figure 8). This was the onset of a disproportionate increase in thermal resistivity.

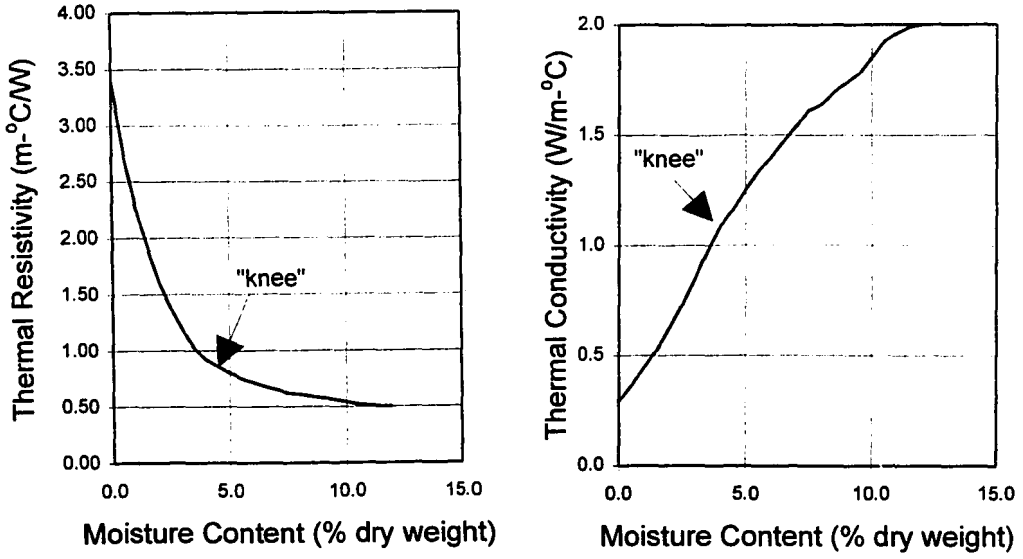

Figure 8. Thermal dry-out curves for (a) resistivity and (b) conductivity. Light gray fine to coarse sand with silt and some fine gravel.

II.9.1.1.3 Heat Capacity

The volumetric heat capacity was given as $\rho c_p = k/\alpha$. For a moist soil, the heat capacity ρcP, in J/kg·°C would be calculated from the specific heats of the components of soil, solids, and water:

$$\rho cP = \rho_d * (c_{ps} + c_{pw} * \Theta_w)/100, \tag{9}$$

where

ρ_d = soil dry density (kg/m^3),

α = thermal diffusivity (m^2/sec) ,

Θ_w = soil water content (% dry weight),

c_{pw} = specific heat of water = 1.0 kJ/kg·K, and

c_{ps} = specific heat of soil solids (kJ/kg·K).

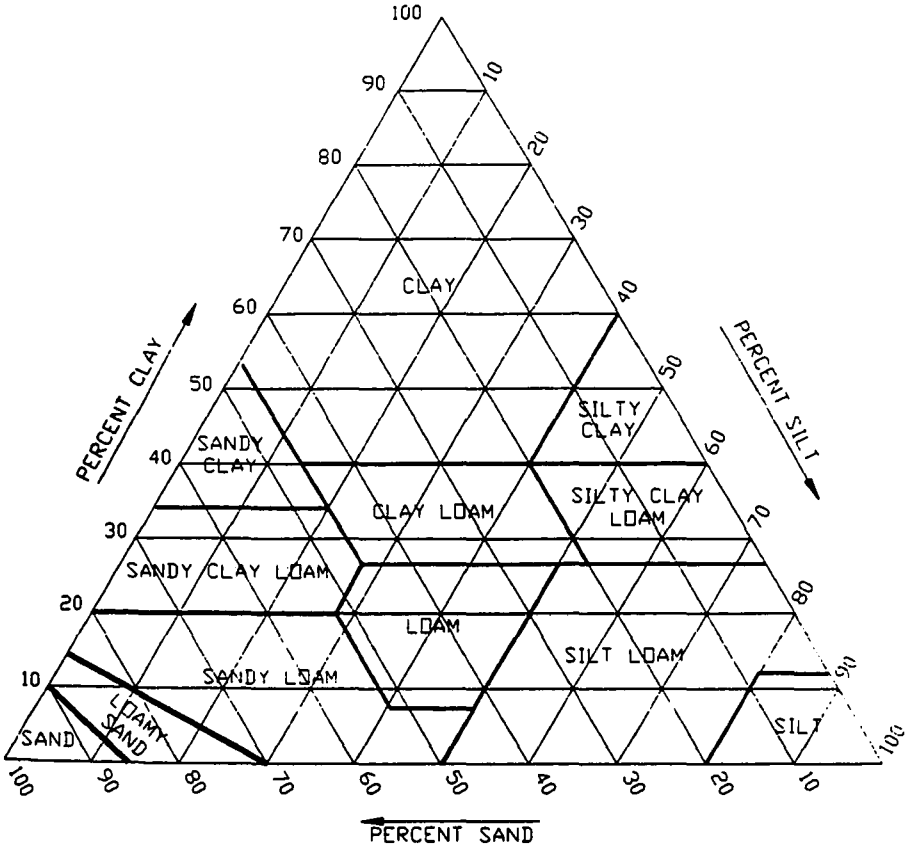

Figure 9. Soil triangle of the basic soil textural classes. (EPRI, 1989)

The general range of the specific heats of mineral soils ranged from 750 to 920 J/kg-°C.

In cooling dominated applications, long term heating can cause the onset of soil "baking." Figure 8 showed how decreasing soil moisture decreases thermal conductivity and therefore lowers performance. Formulation and solution of the coupled partial differential equations for heat and moisture migration is necessary. This allows a quantification of the change in heat transfer as a function of time given a load profile and the soil environment of moisture, conductivity, and temperature.

II.9.1.2 Phillip and de Vries: Moisture

Phillip and de Vries (1957) developed the basic equations for coupled heat and water transport in an incompressible saturated media. Although some later investigators [(Schroeder, 1974), (Hampton, 1989), etc.] have improved some of the mathematics, relatively few have revised their physical insight into the process.

Phillip and de Vries explained the primary mechanisms responsible for heat and water flow in soils. Capillary pressure gradients and gravity caused liquid water to flow. The reason water vapor diffused through a stagnant gas phase was the vapor concentration differences created by temperature and water content gradients. Both distillation and conduction accounted for heat transfer. Therefore, a secondary liquid flow resulted from temperature gradients. They proposed two enhancement mechanisms for liquid-vapor interaction to explain why the amount of water vapor transported in soil was three to ten times the amount predicted by Fick's law of diffusion.

II.9.2 Moisture Computer Models

Very few models for simultaneous heat and moisture transfer in soils have been used in the analysis of ground-coupled heat pumps. The best heat transfer models were designed for buried electrical transmission cables, thermal storage, or buried radioactive waste containers. These were partially verified finite element models of heat and moisture migration. However, they were not designed for complex geometry (such as dual cylinder pipe networks), variable heat flux, or variable operation.

Schroeder (1974) developed one of the earliest computer models on general heat transfer in non-porous media. He used the forward finite difference (FD) method simulate transient two-dimensional heat and moisture transport. The algorithm modified the methodology of Phillip and de Vries. Because the intended application was plant growth and irrigation, modification would be required to model heat exchange with a GCHP.

The next year, Slegel (1975) developed a 2-D transient central finite difference model for heat and mass transfer in soils in the vicinity of heated porous pipes.

The algorithm included gradients of vapor density and water tension, whereas Phillip and de Vries (1957) used temperature and water content gradients. The water table was input as saturated soil and the model achieved good agreement of temperature and moisture content. The intended applications were soil warming and sub-surface irrigation.

II.9.2.1 Hampton: FE with Moisture

Walker (1981) simulated two-dimensional heat and moisture using modified forms of the equations of Phillip and de Vries (1957). The model yielded good temperature agreement but the moisture prediction was rudimentary and un-verified. The same thermal storage project was continued by Hampton (1989). His model included coupled heat and fluid flow in saturated-unsaturated compressible porous media. He was initially motivated by the soil drying problem. His work detailed coupled heat and fluid flow in saturated-unsaturated compressible porous media. The equations differed from those of Phillip and de Vries in four respects, as described on p. 115:

> A pressure-head (rather than water content) approach is employed, thus facilitating analysis of saturated and layered media as well as unsaturated soils; matrix suction is consistently considered a function of temperature as well as water content; the medium is compressible; and the enhancement factors added to the thermal vapor diffusivity have been revised. This improved model of thermal vapor flow fits experimental data better for very dry and wet soils, and can be readily calibrated to data for a given soil. (Hampton, 1989)

Hampton first examined the Phillip and de Vries model, and then expanded on liquid-vapor interactions. He formulated a set of coupled, nonlinear, parabolic partial differential equations in T and Ψ. The variable ϕ_{pw} also appeared, but with a value uniquely determined by Ψ and T because hysteresis was neglected.

Hampton utilized a two dimensional finite element model based on the Galerkin technique. The model was compared with both analytical solutions and a laboratory experiment on soil drying due to a heat source.

Hampton validated his model against laboratory measurements and analytical solutions of the *uncoupled* equations. Presently, there are no analytical solutions to the *coupled* heat and water flow equations derived. The experiment consisted of temperature and moisture content at several points in a disk-shaped box of clay with a heating element in the center. The numerical model predicted a water loss of 67.6 grams after 630 hours. This matched the experimental calibration data within 0.005 volumetric water content.

II.9.2.2 Other Numerical Models

Mulay and Worek (1990) presented and numerically solved (FE with IMSL) the equations governing the transfer of heat and mass in a partially saturated soil. They performed a parametric study showing the effects of various terms on the distributions of temperature and moisture within the soil. Their equations can be compared to those of Hampton.

Cane and Forgas (1991) reviewed computer programs for GCHP systems. Their investigation sought sophisticated and validated models for sizing and energy analysis for designers of small, commercial building GCHP systems. Design or sizing procedures were compared with regard to the heat exchanger lengths predicted for common heat exchanger configurations.

Twenty major programs written by eleven primary authors were identified for GSHP simulation comparison. The comparisons are shown in Table 1 and later compared with the author's program in Chapter VII. Two codes used the line-source, ten used the Kelvin line-source, and nine used finite elements. Only four programs did not incorporate thermal interference. Other options included sizing or accepting

heat exchanger lengths, estimating building loads from user-specified data, and some programs were exclusively for either commercial or residential applications.

The variation in earth temperature with both time of year and depth below the surface was included in all methods by using the Kusuda analytical equations for estimating earth temperatures. The Kelvin Line-Source solutions used superposition for thermal interference. The program from Oak Ridge National Laboratory could model the different thermal performance in the backfill region. Another program from Brookhaven National Laboratory used finite elements to solve for "blocks" of earth rather than a regular mesh. The resulting single pipe serpentine heat exchanger was integrated with the TRNSYS program to predict heat pump performance.

In 1991, the North American standard for sizing earth heat exchangers was the International Ground-Source Heat Pump Association (IGSHPA) method described in the American Society of Heating Refrigeration and Air-Conditioning Engineers (ASHRAE) *Design/Data Manual.* However, comparisons with the National Water Well Association (NWWA) model indicated oversizing heat exchangers between 10% and 33%. As a result, Cane and Forgas (1991) suggested using the NWWA method as a basis for a new design algorithm that could be adopted by software developers.

II.9.3 Moisture Experiments

Sorour, et al (1990) experimentally measured soil thermal conductivity and diffusivity as a function of moisture content. They analyzed soil in Alexandria, Egypt in three classifications: sandy (sand>70%), sandy clay (sand 50% to 70 %), and clay (sand $<$ 50%). These soils were measured in the moisture content range of 0% to 40%. Unfortunately, they chose to only publish the results at one (dry) moisture content.

II.10 Literature Summary

The critical review of literature synthesized the nine levels of modeling ground heat exchange. The most complex levels were three dimensional modeling and coupled heat and mass transfer. Very few models for simultaneous heat and moisture transfer

Table 1. Sophistication of various models

REFERENCES	ANALYTICAL METHOD	INTERACTIONS OR FACTORS ACCOUNTED FOR						
		ON/OFF CYCLING	SOIL MOISTURE FREEZING	SEASONAL EARTH TEMPERATURE VARIATION	THERMAL INTERFERENCE EFFECTS	THERMAL EFFECT OF BACKFILL MATERIAL	FLUID TEMP. LEAVING GROUND HEAT EXCHANGER	SURFACE EFFECTS
Hackner, Hughes, Giffin	Kelvin Line-Source	No	Yes (empirical)	Yes	Yes	No	Yes	No
Mei	Numerical (FD)	Yes	Yes	Yes	Yes (two coils)	Yes	Yes	Yes
Metz, Andrews	Numerical (FE)	Yes	No	Yes	No	No	Yes	Yes
Claesson, Eskilson	Line-Source	Yes	No	Yes	Yes	Yes	Yes	Yes
Bose	Kelvin Line-Source	No	No	Yes	Yes	No	No	Yes
Hart, Couvillion	Kelvin Line-Source (FE)	Yes	Yes (approximate)	Yes (max, min only)	Yes	No	Yes	Yes

in soil had an origin in the discipline of ground-coupled heat pumps. Even fewer numeric schemes considered predominant cooling in dry soil for vertical installation. This investigation was primarily concerned with the effect on performance of moisture migrating away from buried pipes during cooling operation. The best models seemed to be designed for the buried electrical transmission cable scenario of high horizontal constant heat flux loads. These were partially verified finite element models of heat and moisture migration. The currently available GCHP models were summarized in Table 1. None of the transmission cable or GCHP programs combined vertical variable operation, horizontal cylindrical cross sectional parametric analysis, and thermal effect of backfill material.

CHAPTER III

FINITE ELEMENT HEAT TRANSFER EQUATIONS

Two finite element (FE) codes were developed for this thesis: one for pure heat conduction, and the other for coupled heat conduction and moisture diffusion. Appendix A outlines the finite element (FE) method variations (elements, shape functions, interpolation schemes, etc) common to both the heat as well as the heat and moisture model. This chapter derives the specific FE formulations for the heat model, QT (heat and temperature). Appendix B contains the associated flow chart.

The initial steady-state models followed the principles presented by Becker et al. (1981). The final transient heat models were derived from an outline by a student of Oden, Strouboulis (1992), and a short section from the text by Reddy (1993). The final heat and moisture model (QH) was additionally influenced by the moisture flow formulations of Hampton (1989) and the layers concept of Deng and Fedler (1992).

The finite element heat model was coded to approximate solutions to the partial differential heat diffusion equation where no analytical solutions were available. These include nonlinear conductivity, non-homogenous media, irregular two dimensional geometries, and three dimensional irregular geometry. Galerkin's method was used for converting equations into their finite element formulation. The algorithm could use any input file problem that had been converted into its FE formulation.

The guidelines used in developing QT were computational efficiency, ability to accept control elements of squares or rectangles, adequate documentation, accuracy to the required tolerance, and ease of understanding and debugging.

ROLE OF FE MODELING

Partial differential equations were numerically solved by both the finite difference (FD) and the finite element (FE) method. In general, both schemes converged towards the true solution as the grid became finer. The advantage of FD was the relative ease in programing. FD equations were formulated in Chapter IV for inter-element heat transfer which was approximated from the nodes at the center of each

rectangular element. However, more complex geometry, and complicated physical phenomena necessitated the FE method. The Galerkin method converted polynomial equations into FE equations without having to know the solution functional. Each element consisted of three to nine nodes and each node could model a polynomial curve for heat or moisture. As a result, the coding was not intuitive and used a master element to generate invertible mappings and integrations to the actual finite element mesh. Complicated domain geometries were generated by assigning nodal locations. Another advantage of FE was the use of a separate input file. Therefore, at execution time, the operator could select any available file and the associated physical problem, grid, and loading boundary conditions. FE can improve accuracy over FD by providing super-convergence at nodes, and by using higher order polynomial terms. The disadvantages were greater difficulty in coding, more possibilities of error, and voluminous output that had to be sorted out and understood (post-processed).

III.1 Classical Second-order Two-point Boundary-value Problem

The generalized FE model QT could solve any two-point boundary-value problem, although it was best suited for heat and temperature. The general class of second-order linear boundary-value problems with general boundary conditions was first considered. Then acceptable finite element approximations of these problems were constructed.

Computations were performed on each finite element, Ω. A boundary-value problem was characterized by a differential equation which must be satisfied by the solution on the interior domain of Ω, and by boundary conditions that the solution must satisfy at the endpoints of Ω. The derivation of the code QT was two dimensional. However, for simplicity, derivations for only one dimension were shown whenever there was no loss of generality. The general one dimensional steady-state situation was governed by a differential equation of the form:

$$a_0(x)\frac{d^2u(x)}{dx^2} + a_1(x)\frac{du(x)}{dx} + a_2(x)u(x) = f(x), \tag{10}$$

where the coefficients a_0, a_1, and a_2, as well as the function f were given functions of x defined on the given domain. For diffusion process, the variable coefficients in Equation 10 were usually formulated as

$$\frac{d}{dx}\left[a_0(x)\frac{du(x)}{dx}\right] + a_1(x)\frac{du(x)}{dx} + a_2(x)u(x) = f(x). \tag{11}$$

The equation was linear because the derivatives of the solution appear linearly, and of second-order because u'' is the highest order derivative. Therefore, the linear ordinary differential equation was of second order in the function $u = u(x)$. As a consequence of linearity, the *principle of superposition* applied. If u_1 was a solution corresponding to $f = f_1$, and u_2 was solution corresponding to $f = f_2$, then for any arbitrary constants α_h and β_h, $\alpha_h u_1 + \beta_h u_2$ was a solution satisfying Equation 11 for the choice $f = \alpha_h f_1 + \beta_h f_2$.

The Galerkin method of discretization only required that the differential Equation(11) be met at certain subintervals of Ω and in which special conditions were to be met at the endpoints of these subintervals.

The complete specification of the problem must include, in addition to the differential equation, enough additional conditions to determine the values of the two solution constants required when one "integrates" on an interval.

The boundary conditions of the second order equation (11) involved only the values of the solution u and of its first derivative. Therefore, the most general boundary conditions on the interval $0 < x < l$ were of the form

$$\alpha_{h0}\frac{du(0)}{dx} + \beta_{h0}u(0) = \gamma_{h0}$$

and

$$\alpha_{hl}\frac{du(l)}{dx} + \beta_{hl}u(l) = \gamma_{hl}, \tag{12}$$

where $\alpha_{h0}, \beta_{h0}, \gamma_{h0}, \alpha_{hl}, \beta_{hl}$, and γ_{h0} were given constants.

The time-independent problem of Equations 11 and 12 were developed in an abstract setting that was independent of any physical situation. Most physical

problems were formulated with two functions whose values were to be determined. These functions were the state variable u and the flux σ. These quantities were related to each other by a *constitutive equation*, which contained all of the information descriptive of the particular material in which the process was taking place. The general mathematical form of the constitutive equation describing linear material behaviour was

$$\sigma(x) = -k(x)\frac{du(x)}{dx}. \tag{13}$$

The function k is the *material modulus* and any non-uniformity in the state variable u produces a flux σ. The flux σ at any point x in the physical environment should, according to Equation 13, be proportional to the rate at which u changes; the proportionality was determined by k, which would vary with location and material. Each problem had an associated conservation law stating that the net flux entering a subdomain was zero. The flux can enter a subdomain by a distribution of internal sources, or through the boundary region.

For heat conduction, the problem involved conservation of energy, state variable of temperature, heat flux, thermal conductivity modulus, heat sources, and the constitutive equation Fourier's law.

III.2 Time-dependence

If the dependent variable, u, is a function of both position and time, then the steady-state general *one dimensional elliptic two point boundary-value problem* is converted to a transient *two dimensional initial value parabolic problem.* Equation 13 can be substituted into Equation 11 by designating $k = -a_0$ to yield:

$$\frac{d}{dx}\sigma(x) + a_1(x)\frac{du(x)}{dx} + a_2(x)u(x) = f(x). \tag{14}$$

Next, time dependence was introduced to the conservation law

$$\frac{d}{dx}\sigma(x,t) + a_1(x)\frac{du(x)}{dx} + a_2(x)u(x) - f(x,t) + \frac{\partial}{\partial t}\Gamma(x,t) = 0,$$
$$\text{for all } 0 < x < l,\ t > 0. \tag{15}$$

The ground couple heat pump (GCHP) heat conduction problem required transient analysis because the dependent variable of temperature (T) was a function of both position and time. Therefore, σ is the flux, f is the density of distributed internal sources, and Γ is the energy being conserved in the heat transfer process. Because energy was being conserved $\partial\Gamma/\partial t$ represented the time rate of change of entropy per unit length per degree absolute temperature, and was related to the state variable T (temperature) by:

$$\frac{\partial\Gamma(x,t)}{\partial t} = C_p(x,t)\frac{\partial T(x,t)}{\partial t}, \tag{16}$$

where $C_p(x,t)$ was the material property of specific heat (ρc_p).

The heat flux was assumed to be given in terms of the spatial rate of change of T by the linear constitutive form of Equation 13

$$\sigma(x,t) = \frac{\dot{Q}(x,t)}{A} = -k(x)\frac{\partial T(x,t)}{\partial x}, \tag{17}$$

where $\dot{Q}$ was the heat flux, A was the normal area, and $|k(x)| \geq k_0 = \text{constant} > 0$ for all x satisfying $0 \leq x \leq l$. The standard convention in heat transfer was for k to remain positive.

In formulating heat diffusion, the first and zero order terms were omitted,

$$a_1(x,t)\frac{dT(x,t)}{dx} \Longrightarrow 0 \quad \text{and} \quad a_2(x,t)T(x,t) \Longrightarrow 0. \tag{18}$$

The two terms usually existed in heat transfer boundary conditions which were treated later.

The zero order term can also be used in heat transfer to represent temperature induced non-linearity in the coefficients of conductivity. The same equation would

also represent temperature dependent specific heat and diffusivity because of the relation $k = \alpha \rho c_p$. However, this problem was deferred until the non-linear moisture equations.

Equation 14 can be modified with Equations 15 through 18 to become a parabolic partial differential equation (PDE)

$$C_p(x,t)\frac{\partial T(x,t)}{\partial t} - \frac{\partial}{\partial x}\left[k(x)\frac{\partial T(x,t)}{\partial x}\right] = f(x,t), \quad \text{for all } 0 < x < l, \text{ and } t > 0. \quad (19)$$

In problems where Equation 16 was expressed as a second derivative, the associated Equation 19 was hyperbolic. However, heat conduction and a variety of other diffusion processes resulted in the parabolic PDE. In the absence of source terms f (internal heat sources) and for homogeneous boundary conditions $T = 0$, the solutions to parabolic equations have the property that they decay with time relative to the fixed initial data.

The ultimate two dimensional formulation used in this study required three adjustments from the one dimensional parabolic Equation 19. First, terms that were a function of x become a function of x and y. Next we assumed that the specific heat C_p was a smooth function of x and y, was independent of t, and that $C_p(x,y) \geq C_{p0} > 0$. Then boundary conditions were needed in x and y as well as an intial-value of temperature distribution at time $t=0$. Incorporating these changes and utilizing common heat transfer terminology, the resulting diffusion equation for transient heat conduction with appropriate boundary conditions in two dimensions was

$$\rho c_p \frac{\partial T}{\partial t} = \frac{\partial}{\partial x}\left(k\frac{\partial T}{\partial x}\right) + \frac{\partial}{\partial y}\left(k\frac{\partial T}{\partial y}\right) + f(x,y,t), \quad (20)$$

in domain Ω, $0 < t < t_{\text{final}}$,

where

$$f = \left(\frac{\dot{Q}}{A} + \frac{\dot{Q}_T T}{A} + f_0\right),$$

$T = T_0$ on essential boundary $\partial\Omega_1$, $t = 0$, and

$-k\frac{\partial T}{\partial n} = h(T - T_\infty) = H$ on natural boundary condition surface $\partial\Omega_2$.

The definitions included

- ρ = density of soil (kg/m^3),
- c_p = specific heat of the soil ($kj/kg \cdot K$),
- T = soil temperature ($^\circ C$),
- T_0 = initial soil temperature = T_∞ ($^\circ C$),
- T_∞ = far field undisturbed soil temperature ($^\circ C$),
- $\frac{\partial T}{\partial t} = \dot{T}$ the time-rate of change of temperature ($^\circ C$/s),
- t = time (seconds),
- k = thermal conductivity of the soil ($W/m \cdot K$),
- x, y = cartesian coordinate components (m),
- $\dot{Q}$ = heat generated in soil (W per linear meter of pipe),
- $\dot{Q}_T$ = heat proportional to temperature (W/K per linear meter of pipe),
- A = unit area in soil (m^2),
- f= thermal force (kJ/m^2),
- h = surface heat transfer coefficient ($W/m^2 \cdot K$),
- H = heat-flux on the part $\partial\Omega_2$ of the boundary (W/m^2), and
- n = normal coordinate x or y (m).

III.3 Spatial Discretization

In this section, the spatial discretization of the heat transfer equation at a given time step was derived. The derivation culminated with the finite element formulation which was later fully discretized in time.

III.3.1 Vector Variational Formulation

The heat diffusion equation must first be formulated as a vector equation. A variational formulation can then be derived and terms simplified into a format that would readily allow a finite element approximation in two dimensions. The vector formulation of the boundary value problem defined in Equation 20 can be written as

$$
\begin{aligned}
C_p\dot{T} - \nabla \cdot (k\nabla T) &= f \qquad \text{in } \Omega, \\
T &= \bar{T} \qquad \text{on } \partial\Omega_1 \text{ (essential boundary condition)}, \\
-k\frac{\partial T}{\partial n} = H &= h(T - T_\infty) \qquad \text{on } \partial\Omega_2 \text{ (natural boundary condition)}. \qquad (21)
\end{aligned}
$$

The construction of the variational formulation of the boundary-value problem began by defining the residual r_{res} as

$$r_{res}(x,y,t) \equiv C_p(x,y,t)\dot{T}(x,y,t) - \nabla \cdot \{k(x,y,t)\nabla T(x,y,t)\} - f(x,y,t). \qquad (22)$$

Because time was linear and simple, the model was formulated to be finite difference in time and finite element in space. Because no integrity was lost by neglecting time in the FE discretization, the residual can be defined as

$$r_{res}(x,y) \equiv C_p(x,y)\dot{T}(x,y) - \nabla \cdot \{k(x,y)\nabla T(x,y)\} - f(x,y). \qquad (23)$$

To "test" the residual over arbitrary subregions ("finite elements"), r was multiplied by a sufficiently smooth test function v, integrated over each domain in which rv was smooth, and the resulting weighted average of r_{res} set to zero

$$\int r_{res}(x,y)v d\Omega \equiv \int_\Omega \{C_p\dot{T} - \nabla \cdot (k\nabla T) - f\} \cdot v d\Omega = 0. \qquad (24)$$

Equation 24 was the abbreviated vector FE variational formulation. Therefore, the full variational formulation of heat diffusion from Equation 20 was

$$\int_\Omega \rho c_p \frac{\partial T}{\partial t} v d\Omega - \int_\Omega \left[\frac{\partial}{\partial x}\left(k\frac{\partial T}{\partial x}\right) + \frac{\partial}{\partial y}\left(k\frac{\partial T}{\partial y}\right)\right] v d\Omega + \int_\Omega f v d\Omega = 0. \qquad (25)$$

Unfortunately, the finite element formulation could not handle partial derivatives in two dimensions with an order of more than one. This *weak* FE formulation theory did not require integrable second order derivatives of T. As a result, the middle term on the left hand side (LHS) must be expanded into computable terms using a two-dimensional *integration-by-parts formula* to reduce the integral to a first derivative. The product rule for differentiation gave the identity

$$\nabla \cdot (vk\nabla T) = k\nabla T \cdot \nabla v + v\nabla \cdot (k\nabla T),$$

which can be rearranged as

$$v\nabla \cdot (k\nabla T) = -k\nabla T \cdot \nabla v + \nabla \cdot (vk\nabla T). \tag{26}$$

Substitution of the identity in Equation 26 into the integral of Equation 24 yielded

$$\int_{\Omega_i} \{C_p\dot{T}v + k\nabla T \cdot \nabla v - \nabla \cdot (vk\nabla T) - fv\}d\Omega = 0. \tag{27}$$

Here Ω_i was each different boundary condition in an element. The third term could be transformed into a boundary integral using Gauss's Divergence Theorem

$$\int_{\Omega_i} \nabla \cdot (vk\nabla T)d\Omega = \int_{\partial\Omega_i} (vk\nabla T) \cdot \bar{n}dS = \int_{\partial\Omega_i} k\frac{\partial T}{\partial n}vdS. \tag{28}$$

Substitution of the expansion back into the last term in Equation 27 yielded

$$\int_{\Omega_i} \{C_p\dot{T}v + k\nabla T \cdot \nabla v - fv\}d\Omega - \int_{\partial\Omega_i} k\frac{\partial T}{\partial n}vdS = 0. \tag{29}$$

Re-arrangement of terms gave the final heat transfer vector variational equation as

$$\int_{\Omega_i} \{C_p\dot{T}v + k\nabla T \cdot \nabla v\}d\Omega = \int_{\Omega_i} fvd\Omega + \int_{\partial\Omega_i} k\frac{\partial T}{\partial n}vdS, \tag{30}$$

for all v such that $v = 0$ on boundary $\partial\Omega_i$.

III.3.2 Variational Diffusion Equation Formulation

It has now been shown how the second order Equation 20 for heat diffusion can be simplified to first order derivatives by the vector formulation in Equation 30. Combining the two equations, the heat diffusion equation was written in the variational format

$$\int_{\Omega_i} \rho c_p \frac{\partial T}{\partial t} v d\Omega + \int_{\Omega_i} k \left(\frac{\partial T}{\partial x}\frac{\partial v}{\partial x} + \frac{\partial T}{\partial y}\frac{\partial v}{\partial y} \right) d\Omega = \int_{\partial\Omega_i} k \left(\frac{\partial T}{\partial x} n_x + \frac{\partial T}{\partial y} n_y \right) v dS + \int_{\Omega_i} f v d\Omega, \tag{31}$$

where

$$f = \left(\frac{\dot{Q}}{A} + \dot{q}T + f_0 \right),$$

for all $v \in H_0^1(\Omega)$.

Here $H_0^1(\Omega)$= was the set of all functions with square-integrable first-derivatives and zero values at elemental boundaries.

The spatial domain was discretized by a finite element (FE) grid of biquadratic quadrilaterals and triangles. The global function, ϕ_j, corresponded to node j on the FE grid. Therefore, the problem consisted of finding a finite element approximation for the temperature field in the linear superposition form

$$T_h(x,y,t) = \sum_{j=1}^{NNODES} T_j(t)\phi_j(x,y), \tag{32}$$

where

NNODES = total number of nodes in the mesh,

$T_j(t)$ = the time dependent value of temperature at node j,and

$\phi_j(x,y)$ = FE spatial representation of temperature.

Using the finite element approximation method of Becker et al. (1981) the trial functions, v, in Equation 31 was replaced with the basis functions ϕ to yield

$$\int_{\Omega_i} \rho c_p \phi_i(x,y)\phi_j(x,y)\frac{dT(t)}{dt} dxdy + \int_{\Omega_i} \left\{ k\frac{\partial \phi_i(x,y)}{\partial x}\frac{\partial \phi_j(x,y)}{\partial x} + k\frac{\partial \phi_i(x,y)}{\partial y}\frac{\partial \phi_j(x,y)}{\partial y} \right\} T(t) dxdy = \int_{\partial\Omega_i} \left\{ k\frac{\partial \phi_i(x,y)}{\partial x} n_x + k\frac{\partial \phi_j(x,y)}{\partial y} n_y \right\} T(t) dxdy + \int_{\Omega_i} \{\dot{q}\phi_i(x,y)\phi_j(x,y)\} T(t) dxdy + \int_{\Omega_i} \left(\frac{\dot{Q}}{A} + f_0 \right)(x,y)\phi_i(x,y) d\Omega. \tag{33}$$

An important physical change occurred in the boundary value problem because of replacing trial functions v with basis functions ϕ. As explained in Chapter VI, one can select appropriate shape functions and their associated quadrature integration scheme for the quality of solutions desired.

III.3.3 Spatially Discrete Boundary Conditions

Equation 33 showed the general boundary conditions of all parabolic equations. GCHP heat transfer modeling specifically considered the above general heat diffusion problem of the following vector format

$$C_p\dot{T} - \nabla T(x,y) = f(x,y) \quad \text{in } \Omega, \tag{34}$$

with the boundary conditions

$T = T_\infty$ on essential boundary condition outer edge Γ_1,

$T = T_{pipe}$ on essential boundary condition inner edge Γ_2, or

$\alpha_h \dfrac{\partial T}{\partial n} + \beta_h T = \gamma$ on natural boundary condition inner edge Γ_2.

The initial conditions were

$T = T_0$ on all nodes at initial time,

$\dot{q}T =$ heat generated proportional to T.

These boundary conditions must be converted to the format of their associated equation (33).

The three GCHP heat transfer boundary conditions were constant temperature, convection, and constant heat flux. In finite elements, the three elementary types of boundary conditions are handled differently and categorized as *essential* for variable values (such as T), *Nueman* for gradients (such as dT/dx), and *natural* for a combination of the other two.

A temperature was always required to maintain the farfield temperature on the outer boundary condition edge Γ_1. Essential boundary conditions were handled by the *penalty method* of forcing the matrix to yield the desired value. Γ_2 was forced

to allow $T = T_{pipe}$. This scenario modeled ground conduction without modeling the effect of water loop fluid flow.

A convective boundary condition was needed in modeling the effect of fluid flow in the water loop pipe. Most convective studies only used the soil region as a boundary condition. In this study, the primary concern was modeling soil behavior. However, convection can be handled in QT by a natural (gradient and value) boundary condition for normal heat flux on inner edge Γ_2

$$\frac{\dot{Q}}{A} = -k\frac{\partial T_{pipe}}{\partial n} = h(T_{pipe} - T_{constant}) \approx P_{i,j}T_j - \gamma_i. \tag{35}$$

where $P_{i,j}$ was for heat loading that proportional to temperature and γ_i was heat loading that is independent of temperature.

Constant heat flux can also be applied to the inner boundary condition edge Γ_2. This was useful when given the total amount of heat rejected to the ground. The thermal force loading was independent of temperature

$$f = \frac{\dot{Q}}{A} = -k\frac{\partial T_{pipe}}{\partial n} = -\gamma_i. \tag{36}$$

The derived boundary condition formulations in Equations 34 through 36 were incorporated into Equation 33. which was of the form

$$[G\tilde{K}]_{i,j}T_j = (\tilde{F})_i(t). \tag{37}$$

The constant boundary condition terms was added to the $(\tilde{F})_i$ vector, while terms to be multiplied by the temperature were inserted into the $(\tilde{K})_{ij}$ matrix.

The temperature dependent boundary conditions were applied to the boundary elements of the discrete problem by modifying the entries of the element stiffness matrix (thermal conductivity matrix) in Equation 33

$$[GK] = \sum \left\{ (\tilde{K})_{ij} + (\tilde{P})_{ij} \right\}$$
$$= \int_{\Omega_e} \left\{ k \frac{\partial \phi_i(x,y)}{\partial x} \frac{\partial \phi_j(x,y)}{\partial x} + k \frac{\partial \phi_i(x,y)}{\partial y} \frac{\partial \phi_j(x,y)}{\partial y} \right\} d\Omega$$
$$+ \int_{\Omega_e} h \phi_i(x,y) \phi_j(x,y) dS. \tag{38}$$

The elemental thermal force matrix for the loading that was independent of temperature in Equation 33 is also modified

$$[F] = \sum \left\{ (\tilde{F})_i + (\gamma)_i \right\} = \sum \int_{\Omega} f(x,y,t) \phi_i(x,y) d\Omega$$
$$= - \int_{\partial \Omega_e^*} HT_{constant} \phi_i(x,y) dS + \int_{\partial \Omega_e^*} \gamma \phi_i(x,y) dS, \tag{39}$$

where $\partial \Omega_e^* = \partial \Omega_e \cap \partial \Omega$ = the intersection of the boundary of the element with the outer boundary. Note $\partial \Omega_e^*$ is empty for all other elements.

III.3.4 Working Form of Heat Diffusion Equation

Two terms in Equation 33 had little or no application. The first term was

$$\int_{\Omega} \left\{ k \frac{\partial \phi_i(x,y)}{\partial x} n_x + k \frac{\partial \phi_j(x,y)}{\partial y} n_y \right\} T(t) d\Omega = 0. \tag{40}$$

These use unsymmetric volume convection terms which were small and cannot be represented with banded matrices. Banded matrices were required for computational efficiency. As a result, volumetric convection was physically removed from the model.

The other minor term was

$$\int_{\Omega} \dot{q} \phi_i(x,y) \phi_j(x,y) d\Omega = 0. \tag{41}$$

This integral representing surface convection temperature dependency was rarely used in this study of soil. The term was available in QT because some researchers model the water loop and used the soil as a convective outer boundary

condition. In the study of constant heat or constant temperature, this term was always zero ($P_{i,j} = 0$).

When the two minor terms were neglected, the final form of the first order spatially discrete variational diffusion of Equation 33 was

$$\int_\Omega \rho c_p \phi_i(x,y)\phi_j(x,y)\frac{dT(t)}{dt}d\Omega + \int_\Omega \left\{ k\frac{\partial \phi_i(x,y)}{\partial x}\frac{\partial \phi_j(x,y)}{\partial x} + k\frac{\partial \phi_i(x,y)}{\partial y}\frac{\partial \phi_j(x,y)}{\partial y} \right\} T(t)d\Omega = \int_\Omega f(x,y,t)\phi_i(x,y)d\Omega. \tag{42}$$

III.4 Complete Discretization in Time

The transient diffusion equation was spatially discretized in Equation 33. However, transient numerical application required discretization in time. The finite element approximation of Equation 33 resulted in a system of NNODE (number of nodes) ordinary differential equations (ODE's) in the NNODE unknown functions $T_j(t)$ of the form

$$\tilde{C}_{i,j}\frac{dT_j(t)}{dt} + (\tilde{K}_{i,j} + \tilde{P}_{i,j})T_j(t) = \tilde{F}_i(t), \quad 0 < t \leq t_{final}, \tag{43}$$
$$T_j(0) = T_0[1] \quad t = 0,$$

where

$T(t) = [T_1(t), \cdots, T_{NNODES}(t)]^T$, is a vector of nodal temperatures,

$$\tilde{C}_{ij} \equiv \rho c_p \int_\Omega \varphi_i \varphi_j d\Omega = \int_\Omega \rho c_p \phi_i(x,y)\phi_j(x,y)d\Omega,$$

$$\tilde{K}_{ij} \equiv k\int_\Omega \nabla\varphi_i \nabla\varphi_j d\Omega = \int_\Omega \left(k\frac{\partial \phi_i(x,y)}{\partial x}\frac{\partial \phi_j(x,y)}{\partial x} + k\frac{\partial \phi_i(x,y)}{\partial y}\frac{\partial \phi_j(x,y)}{\partial y} \right) d\Omega,$$

$$\tilde{P}_{ij} \equiv \int_{\Omega_e} h\phi_i(x,y)\phi_j(x,y)dS,$$

$$\tilde{F}_i(t) \equiv \sum \int_\Omega f\varphi_i d\Omega + \int_{d\Omega} = \int_\Omega hT_\infty \phi_i(x,y)d\Omega + \int_{\partial\Omega_\varepsilon} \gamma\phi_i(x,y)dS,$$

$T_0 =$ initial temperature, and

$[1] = [1,1,1,\cdots,1]^T$ vector with unit entries.

The physical meanings were:

- T(0) = given initial condition,
- $\tilde{C}$ = elemental heat capacitance,
- $\tilde{K}$ = elemental thermal conductivity matrix,
- $\tilde{P}$ = temperature dependent convection terms, and
- $\tilde{F}$ = elemental thermal force matrix, a load vector which has contributions from body sources and boundary conditions.

III.4.1 Time-Stepping Schemes

The above heat diffusion equation was nonlinear predominantly because of the unsteady term. Nonlinearity can also result if the the thermal conductivity was a function of temperature ($\alpha_h = \alpha_h(T)$ which implied $C_p = \rho c_p(T)$). Equation 43 must be solved for each step in time for the temperature. Then, the conductivity can be computed as a function of temperature. Using vector notation, the parabolic Equation 43 can be written as

$$[C]\{\dot{T}\} + [K + P]\{T\} = \{F\}, \tag{44}$$

subject to the initial condition $\{T\}_0 = \{T_0\}$.

The most common method for solving Equation 44 was the finite difference θ *family of approximations.* The weighted average of the time derivative of a dependent variable is approximated at two consecutive time steps by linear interpolation of the values of the variable at the two time steps:

$$(1-\theta)\{\dot{T}\}_n + \theta\{\dot{T}\}_{n+1} = \frac{\{T\}_{n+1} - \{T\}_n}{\Delta t_{n+1}} \quad \text{for } 0 \le \theta \le 1. \tag{45}$$

Rearranging Equation 45 yielded

$$\Delta t_{n+1}\left((1-\theta)\{\dot{T}\}_n + \theta\{\dot{T}\}_{n+1}\right) = \{T\}_{n+1} - \{T\}_n \quad \text{for } 0 \le \theta \le 1. \tag{46}$$

Equation 46 was used to reduce the parabolic ordinary differential Equation 44 to algebraic equations among the temperatures T_j at time t_{n+1}. Because 44 was valid for all $t > 0$, the equation it was valid for $t = t_n$ and $t = t_{n+1}$

$$[C]\{\dot{T}\}_n + [K + P]_n\{T\}_n = \{F\}_n \tag{47}$$

and

$$[C]\{\dot{T}\}_{n+1} + [K + P]_{n+1}\{T\}_{n+1} = \{F\}_{n+1}. \tag{48}$$

with the assumption of the capacitance (or mass) matrix being constant in time. In other words $[C] = \rho c_p$ = constant, while the conductivity k can still change with time, moisture, etc. If both sides of Equation 46 are multiplied with $[C]$, the result was

$$\Delta t_{n+1}(1-\theta)[C]\{\dot{T}\}_n + \Delta t_{n+1}\theta[C]\{\dot{T}\}_{n+1} = [C]\Big(\{T\}_{n+1} - \{T\}_n\Big). \tag{49}$$

Substituting for $[C]\{\dot{T}\}_{n+1}$ and $[C]\{\dot{T}\}_n$ from Equations 47 and 48:

$$\begin{aligned}\Delta t_{n+1}(1-\theta)\Big(\{F\}_n - [K+P]_n\{T\}_n\Big) + \Delta t_{n+1}\theta\Big(\{F\}_{n+1} - [K+P]_{n+1}\{T\}_{n+1}\Big)\\ = [C]\left(\{T\}_{n+1} - \{T\}_n\right).\end{aligned} \tag{50}$$

This equation was then rearranged so that all the unknowns were on one side:

$$[\text{Unknown}]\{T\}_{n+1} = [\text{Known}],$$

or

$$\begin{aligned}&\Big([C] + \Delta t_{n+1}\theta[K+P]_{n+1}\Big)\{T\}_{n+1}\\ &= \Big([C] - \Delta t_{n+1}(1-\theta)[K+P]_n\Big)\{T\}_n + \Delta t_{n+1}\Big(\theta\{F\}_{n+1} + (1-\theta)\{F\}_n\Big).\end{aligned} \tag{51}$$

The symbols can be simplified by adapting the notation

- $T_n = \{T\}_n = T(t_n)$,
- $T_{n+1} = \{T\}_{n+1} = T(t_n + \Delta t)$,
- $\tilde{F}_n = \{F\}_n = F(t_n)$,

- $\tilde{F}_{n+1} = \{F\}_{n+1} = F(t_n + \Delta t)$,
- $\tilde{C} = [C]_n = [C]_{n+1} =$ constant , and
- $(\tilde{K} + \tilde{P})_i = [K + P]_i$.

Equation 51 simplified to

$$\Big[\tilde{C} + \theta\Delta t_{n+1}(\tilde{K} + \tilde{P})_{n+1}\Big]T_{n+1} = \Big[\tilde{C} - (1-\theta)\Delta t_{n+1}(\tilde{K} + \tilde{P})_n\Big]T_n + \Delta t_{n+1}\Big[\theta\tilde{F}_{n+1} + (1-\theta)\tilde{F}_n\Big]. \tag{52}$$

III.5 Physical Significance of Terms

The physical significance of the primary terms in this chapter were explained by heat transfer Equation 20 and its finite element formulation of Equation 43. The final formulation in Equation 52 used the vector formulation of Equation 44 to combine all the unknown terms at time step $n + 1$.

III.6 Computation of Matrices

The numerical problem shown in Equation 52 was solved by first computing the matrices $\tilde{C}, \tilde{K}_i, \tilde{P}_i$, and $\tilde{F}_i$. Next, the matrix problem was formulated and separated into the knowns and unknowns in Equation 51. Finally, the problem was solved to sequentially march from each known solution at time t_n to the next time step at t_{n+1}.

III.7 Time-stepping Scheme Theory

This model was 2-D finite element in space, but 1-D finite difference in time. Different values of θ were used depending on the desired time-stepping scheme Özişik (1980) and Reddy (1993).

- *Explicit* or *forward difference* method ($\theta = 0$). It is conditionally stable because the maximum step size of Δt is limited by the restriction imposed on the Fourier parameter

$$Fo \equiv \frac{\alpha_h \cdot \Delta t}{(\Delta x)^2} \leq \frac{1}{2}. \tag{53}$$

The error for the first time derivative was of the order (Δt). Using a "larger" Δt required compensation by a smaller Δx. The Δx was the largest length or width of an element. So for each mesh there was a maximum allowable Δt.

- *Crank-Nicolson* or *central difference* method ($\theta = \frac{1}{2}$). This was unconditionally stable but required more computational effort (this was the selected scheme). It had a larger truncation error (when $\Delta t \geq 1$) which was of the order $(\Delta t)^2$. A "large" Δt can cause non-physical oscillations. Again, the accuracy was improved by utilizing a smaller Δt.
- *Galerkin* ($\theta = \frac{2}{3}$) method. This method was also stable, required more computational effort, and had a larger truncation error (when $\Delta t \geq 1$) which was of the order $(\Delta t)^2$. Most studies in this thesis utilized this value.
- *Fully implicit* or *backward-differencing* method ($\theta = 1$). This scheme had lower order accuracy than the Crank-Nicolson, but was unconditionally stable. There was a practical limit to the desired time step size because the error was proportional to the time step. The error, as in the explicit method, was of the order of (Δt).

III.8 Summary

This chapter derived the FE formulation theory for the heat model, QT. Appendix A explains the coding of the finite element method, while Appendix B contains the flowchart.

The chapter began by introducing the two point boundary value problem and its general boundary conditions. Next, time dependence was incorporated. Then the Galerkin method converted the equation into a first degree variational calculus format. The variational problem was first discretized by FE spatially, and then discretized in time using FD. Finally, the specific heat equation was presented, although QT is general enough to solve any other diffusion process. And in closing, the chapter outlined the matrix formulation flowchart.

CHAPTER IV

VALIDATION OF HEAT TRANSFER MODELS

Heat transfer models have been developed in Appendix D for finite difference, and Chapter III for finite elements. This chapter discusses the validation of the heat transfer models with bench mark problems which have analytical solutions.

This chapter compared the two heat transfer models developed in Chapter III with the analytical solutions available for steady state and transient problems and discusses leg spacing consideration. These included: overall U-value, single source heating, single source constant temperature, and dual source constant temperature solutions.

IV.1 Overall U-value

The overall heat transfer coefficient (UA) for a heat exchanger with fouling can be quantified utilizing the principles of Incropera and DeWitt (1985) as

$$(UA) = \frac{1}{\sum R} = \frac{1}{\frac{1}{2\pi r_o L \eta_o h} + \frac{R_{foul}}{2\pi r_o L \eta_o} + \frac{ln(r_{b'fil}/r_o)}{2\pi k_{b'fil} L} + \frac{ln(r_{soil}/r_{b'fil})}{2\pi k_{soil} L}}, \tag{54}$$

where

- η_o is the un-fouled heat exchanger efficiency, and
- "b'fil" is the abbreviation for backfill material.

Overall U-values are displayed in Figure 10 as $UA = \dot{Q}_r/(T_s - T_\infty)$. Both the FD and FE models (more thoroughly explained in the constant temperature section) maintained a constant source temperature of 35°C and a farfield of 22.2°C. U-values asymptotically decreased with time. What was not incorporated was that U-values were also a function of fraction on-time and farfield soil temperature (T_∞). As other

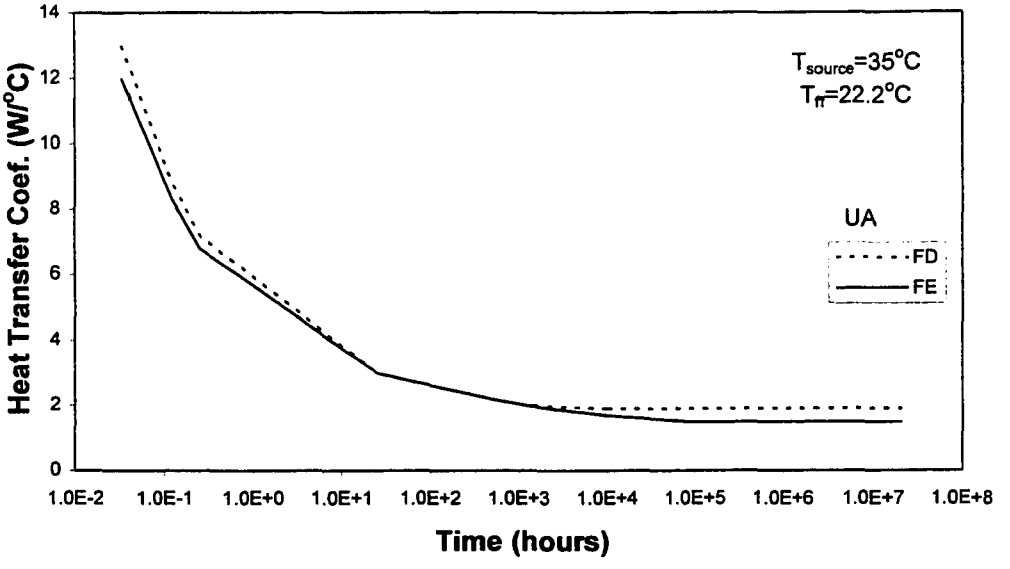

Figure 10. Overall heat transfer coefficient (UA) for constant temperature source in FD and FE models

researchers have also concluded, the large variation in U-Values rendered the method too simplistic to analyze the complexity of transient heat transfer.

IV.2 Single Source Heating

For single source heating, the transient cylindrical-solution of Ingersoll et al (1948) was presented in Equation 7, while the steady-state solution of Claesson and Dunard (1983) was explained in Equation 4. Both solutions were used for verification of the heat transfer model.

The Ingersoll solution for a pipe transferring a constant heat flux Q' per unit length yielded the temperature T at a given time and point (Z, R). The Jaeger (1942) solutions to the Ingersoll equation were used for transient verification.

The grid as configured for the Claesson solution was shown in Figure 5 (Chapter II), and the associated input parameters were:

- $\dot{Q}$ = heat generated in soil (48.1 W/ linear meter of pipe),
- ρ = density of soil (2082 kg/m^3),
- c_p = specific heat of the soil (858 $j/kg \cdot K$),
- T_o = initial soil temperature = T_∞ (22.2°C),
- k = thermal conductivity of the soil (1.73 $W/m \cdot K$), and
- r_o = radius of the heat source (0.01334 meters or nominal 1/2 inch pipe).

The steady-state temperature solution of Claesson was manually solved at each location (x,y) in accordance with Equation 4.

The FD and FE methods were meshed and coded to numerically approximate the analytical solutions for single source constant heating. The center sections of the grid areas are shown in Figure 11 for FE and Figure 12 for FD. Both meshes contained two sources. Therefore, the one source scenario was a special case of when only one of the sources was "turned on" (heat loaded).

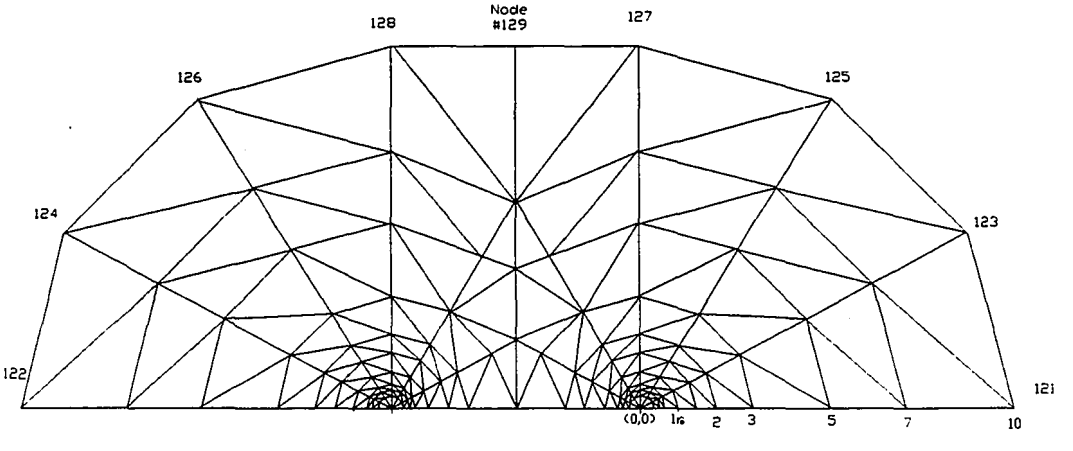

Figure 11. FE mesh for twin cylinders with three nodes per element (0-10r_o in grid of 1600r_o where r_o =0.0133 m)

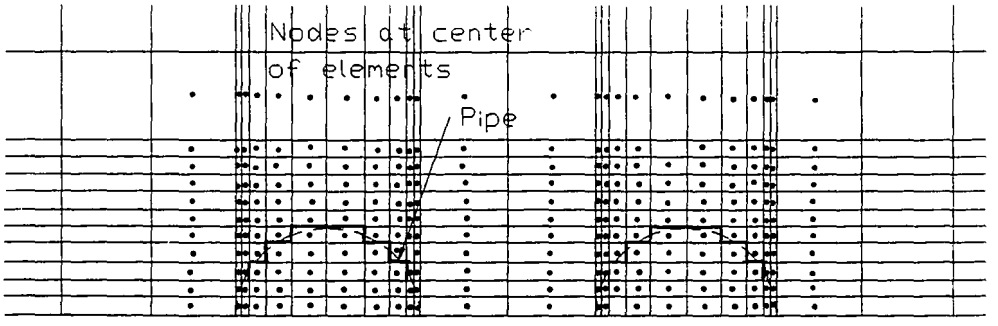

Figure 12. FD constant heat stair-step approximation of circular pipes with one node per element (0-3r_o in grid of 400r_o)

The most important FE and FD algorithm differences were in the meshes, mesh size and boundary conditions. As shown in Figures 11 and 12, FD used one-node quadrilateral elements while FE used triangular three-node elements (with dormant options of 4,6,8, and 9 nodes). Both meshes have options of cartesian or cylindrical coordinates. However, because it was much more complicated to use cylindrical coordinates with a two-cylinder mesh, only cartesian coordinates were utilized. In cartesian coordinates the FD model could only mesh right angle elements, and thus used a stair-step approximation for cylinders as shown in Figure 12. A visible drawback was the surface convection area exceeding that of a cylinder.

FD boundary conditions were superimposed point loads of strength watts/node (48.1 watts $\div$ 24 nodes). The FE method had options of point loads, surface value loads (temperature for heat transfer simulation), and surface flux loads (temperature gradients for heat transfer). As noted above, the FD code could not approximate the curved pipe surface in both shape and area (unless the pipe wall had right angles, or there was only one pipe so cylindrical coordinates could be enabled). Therefore, the FE method utilized the more realistic BC of imposing heat on the single side of each triangular element that approximated the pipe surface area with strength of watts/meter (48.1 watts $\div$ $2\pi r_o$).

The mesh sizes also varied. The FE farfield boundary location was 1600 radii (which is equivalent to 21.3 meters), contained 223 nodes, 378 elements, and an execution time of 40 seconds (VAX 9000-210V during low use time, 157 iterations to one million hours). The FD grid size was 400 radius (which is equivalent to 5.3 meters), contained 1800 nodes, 1800 elements, and required a run time of 90 seconds. The FD grid required more nodes because the element width cannot vary horizontally or vertically. Conformal mapping with FD was not attempted.

Figure 13 plots the temperature variation with time for the FE, FD, and Ingersoll solution. The transient solution provided by Jaeger was available up to a Fourier number of 25,000 (1274 hours). Similar results are shown for the surface and at 10 radii. However, at 10 radii the temperature did not begin to increase until 400 minutes. The time to reach steady state was a function of grid size. The 400 radii FD grid temperatures leveled off after 1,000 hours, while the 1600 radii FE temperature leveled off after 10,000 hours. The steady state temperature profile is presented in Figure 14. The 400 radii temperatures were lower because the Claesson solution was a function of the farfield boundary location. Figure 15 presents the FD and FE excess errors which were computed as

$$\left(\frac{T_{solution} - T_{numerical}}{T_{solution} - T_o} \cdot 100\% \right). \tag{55}$$

Because the excess error formula was intrinsically skewed, the error was magnified at temperatures close to T_o. The excess error for more than 25 hours ranged from 4% to 8% for FE and -7% to 3% for FD. The average FE error was 0.6°C.

Steady-state temperatures were reached in both algorithms (Figure 15) after 100,000 hours. Since this time was over 10 years, the comparison produced limited useful information for GCHPs. Both sets of numerical values show under-prediction of the Claesson steady-state temperatures by 13% to 16% for FE and 5% to 10% for FD.

IV.2.1 Line Solution vs Cylindrical Solution

An important result in Figures 13 and 15 was that the excess error was not a strong function of the distance $(y - d)$ from the origin (the geometry is shown in

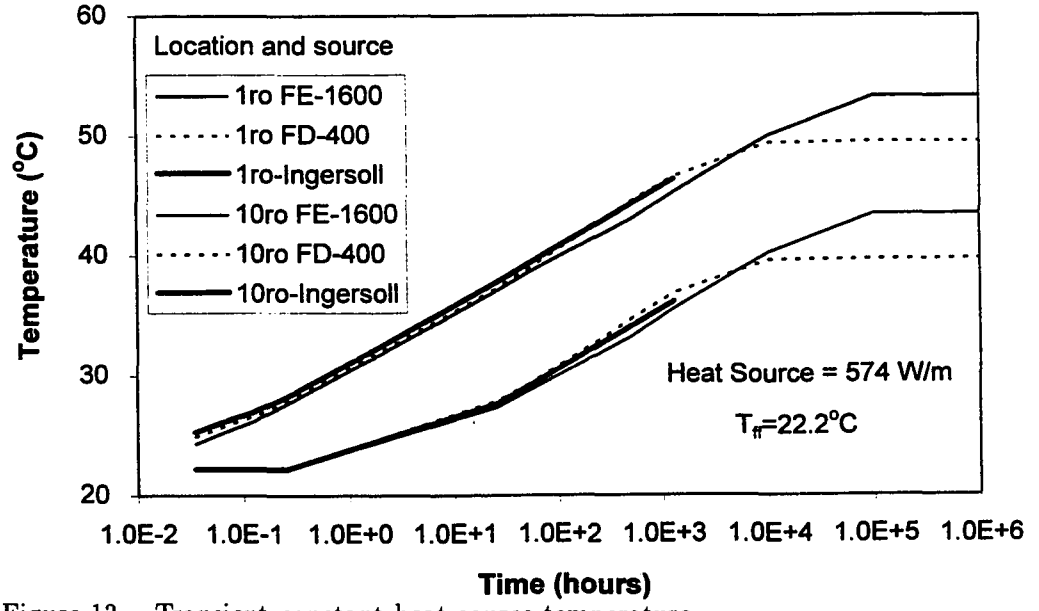

Figure 13. Transient constant heat source temperature

Figure 5, Chapter II). While Ingersoll provided the required cylindrical solution, the Claesson line source should only approximate a cylindrical source at large distances. The author expected the Claesson line solution accuracy to depend on the validity of the assumption that the radius was much smaller than the depth ($r_o \ll y - d$). This unexpected line solution accuracy will be utilized for validation because the only dual source solution found was that of Claesson. However, the excess errors in Figure 15 were about 5% higher for the steady-state values than the transient values. The average errors for FE was 0.6°C for transient and 4.3°C for steady state temperatures. The author suspects that the line solution error was 5%, although a lesser possibility was the accumulation of numerical error over time with a limited size boundary. However, the Claesson solution accounted for the boundary size. In addition, proportionally larger time steps only required another twenty iterations to reach steady state.

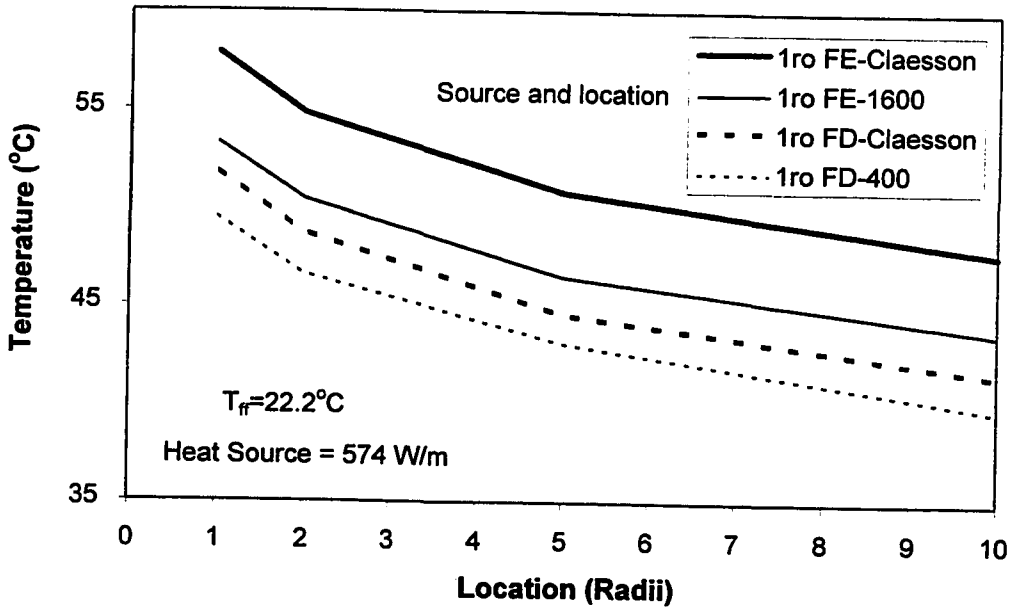

Figure 14. Steady state constant heat source temperature

IV.2.2 Error Minimization

The most crucial question on errors was why FD values were slightly more accurate than FE values. One would have expected the more powerful, larger and sophisticated FE algorithm to produce better values. In addition, transient accuracy should have improved with larger boundary sizes because the analytical Ingersoll solution (and real case) had an infinite boundary. And finally, the FD element geometry had length to width ratios of over 400 due to the rectangular stair-step at the origin. One would expect this abnormally to cause numerical error or even instability. However, error minimization involves more than just grid size, absolute accuracy and numerical scheme in a very simple problem.

The FD was only more accurate because it consisted of a longer run-time mesh (700% more nodes and more computations), and the simplicity of the bench mark problem. Both numerical models produced the expected pattern in Figure 15. The FD values were scattered both above and below the Ingersoll solutions while

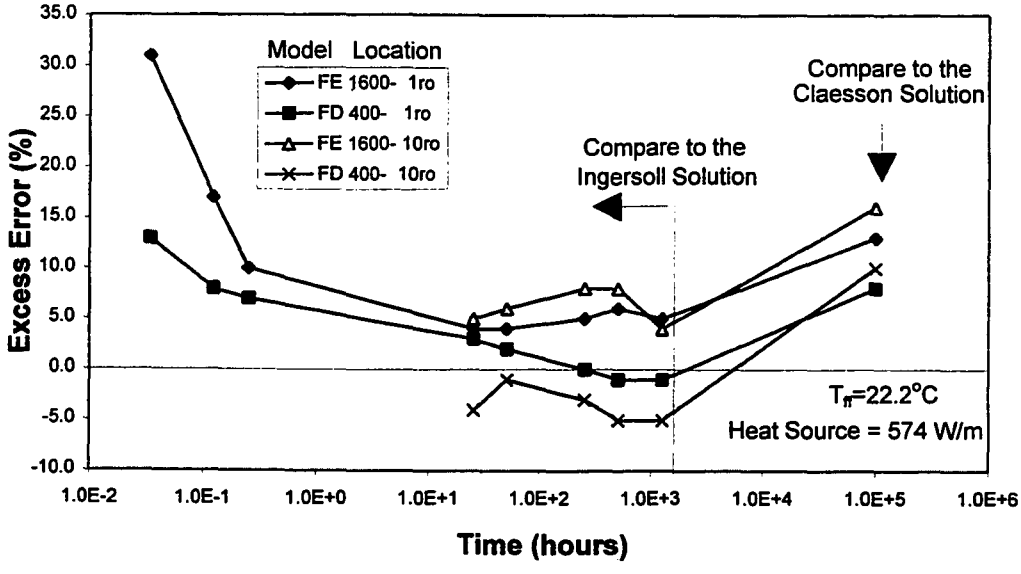

Figure 15. Excess error for FE and FD

the FE values converged from the *stiff side* (under-predict temperature). The FE method converged from the *stiff side* because linearization truncated the higher order polynomial contributions. Therefore, with the option of post-processing results or adding more nodes, the FE's consistent pattern of under-predicting values was better than the FD scatter. In addition, the FD model was more accurate than the FE model for both the transient and steady-state cases, but took twice as long to run. Theoretically, the FE's consistent pattern of under-prediction should be able to converge with more nodes to achieve less error than FD with an equivalent number of nodes and run-time. Sequentially more complicated problems required FE's more powerful attributes such as: robust boundary conditions, ability to handle moisture, solve a variety of different problems and geometries, and being entirely written by the author. For example, the FD error would have been much greater if convection was being modeled (instead of inputting point loads) because it could not approximate both the geometry and the surface area.

IV.2.3 Farfield Boundary Size Optimization

Different sizes of grids were examined to optimize between an infinite farfield temperature boundary condition and minimizing execution time. Figure 16 presents FE results at a radius of five for meshes of 100, 400, and 1600 radii. The Ingersoll solution for Bessel functions was only available for under a Fourier number of 25,000. Results showed that the difference in execution time was virtually identical for the three grids because the geometric increase in element size only required about 20 more nodes for each four fold increase in grid size. As expected, the grids provided the same accuracy at short elapsed times, while the larger grids were closer to the Ingersoll solution of infinite farfield temperature at longer run-times.

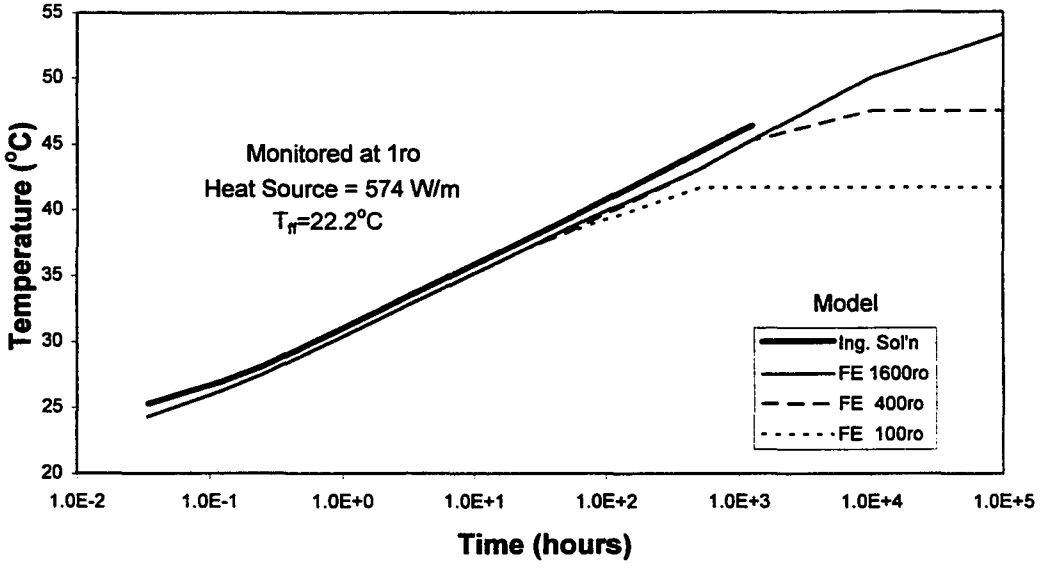

Figure 16. Transient finite element boundary size temperature accuracy

The most important result of Figure 16 was the quantification of the boundary size required for a chosen cumulative simulation time span. For the Ingersoll solution

with a Fourier number up to 25,000 (53 days), any grid size over 400 radii was sufficient. However, for the steady-state temperature in an infinite grid, even the 1600 radii grid was clearly insufficient (temperatures tapered off after 10,000 hours).

Similar results for FD grid size optimization are shown in Figure 17. However, the FD results were more accurate. In addition, the FD temperatures did not taper off as quickly and reached 5°C higher at steady state and a boundary of 400 radii. Clearly, long-term temperatures improved with larger boundary sizes for both FE and FD.

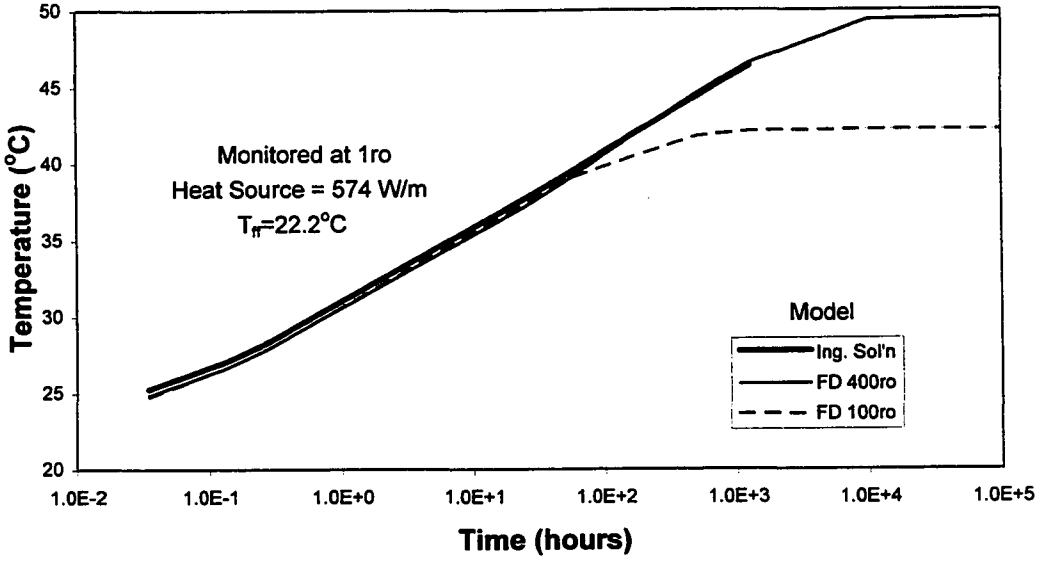

Figure 17. Transient FD boundary size temperature accuracy

IV.2.4 Number of Nodes vs Accuracy

If a numerical model was internally consistent (mesh and equations), then accuracy should be improved (up to optimization) by refining the grid with more elements or nodes. Figure 18 examines the effect of the number of nodes on the

accuracy of the models. Three models with farfield boundaries of 100 radius were compared with each other and the Ingersoll transient solution. The least accurate model was FE 100 radii 132 nodes, the one with the least number of nodes. It contained 3 nodes per element and under-predicted the temperature at 1276 hours by 15°C. The middle accuracy model was the FD model which had the most number of nodes. It contained 1400 nodes and under-predicted the temperature at 1276 hours by 7°C. The most accurate model was the FE 1600 radii 538 nodes. The mesh used 6 and 8 node elements for a total of 638 nodes, and under-predicted the temperature at 1276 hours by only 4°C. Therefore, increasing the number of nodes (and run-time) improved the accuracy. In addition, the FE model with about half as many nodes appeared to be more accurate than the FD model. The FD model also required more nodes to mesh the same farfield distance from the origin because the square area was greater than the semi-circle region.

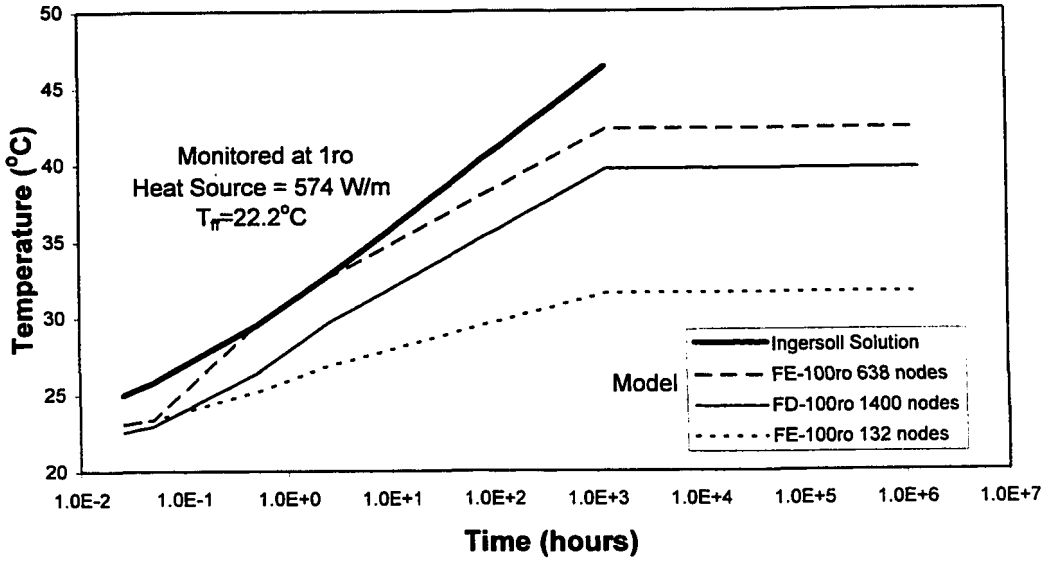

Figure 18. Number of nodes vs accuracy in 100 radii models

IV.3 Dual Cylindrical Source Heating

The more realistic case of two parallel cylindrical heat sources was examined. Unfortunately, no analytical transient solution was found. However, the steady-state temperature in the ground can be obtained directly from the superposition of the single cylinder solution of Claesson and Dunard. The previous single cylinder results indicated that the Claesson solution was about 5% higher than the extrapolated Ingersoll solution. The associated Claesson grid was presented in Figure 6, and the superpositioned temperature at each location (x, y) was manually calculated from Equation 5.

Numerical simulation was performed with the FE and FD meshes which were shown in Figures 11 and 12. The two sources were separated by four radii in the FD model and 6.85 radii in the FE model.

The steady-state results for FE and FD are shown in Figure 19 and are consistent with the single source results. In both models, the monitored temperatures were located at $1r_o$ and directly above Q_1. There were three data points for the constant heat input ratios of Q_1/Q_2 equal to zero, one-half, and one.

IV.3.1 Dual Source Conclusions

Results showed that the FE error ranged from 13% to 22% below the solution (an average of 4.8°C). The FD results were more accurate and under-predicted by 8% to 10%. Like the single source results, these discrepancies were also independent of location at each radii; i.e. whether the temperature was monitored closer to the influence of one of the legs or equidistant to both legs. Superposition accounted for thermal short-circuiting and there was no indication of increasing error in the equation with thermal short circuiting. What was not quantified (until the next chapter) was the effect of different source separation distances. With the same separation distance, the FD model should have had less error as in the single source case.

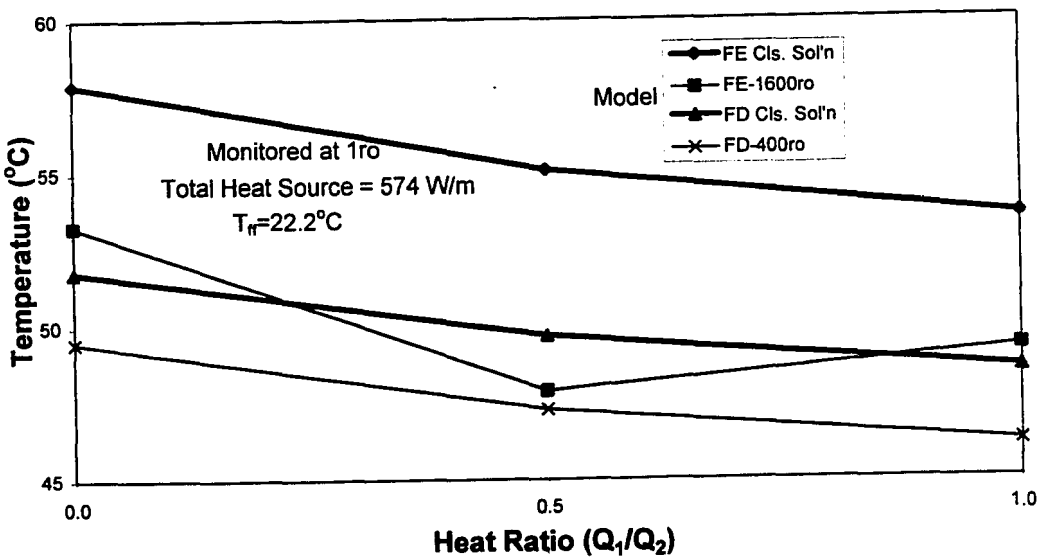

Figure 19. Dual heat source models for FE and FD

IV.4 Single Source Constant Temperature

The transient cylindrical constant temperature solution was given by Ingersoll et al (1948), but a steady-state solution was apparently not available

The solution for *constant surface temperature* for an infinite cylinder was presented in Chapter II. The time rate of heat exchange per unit length (Q') for a long isolated cylinder held at constant temperature deviation (ΔT) from the initial soil temperature was given in Equation 8 as $Q' = k\Delta T F(Z)$. Equation 8 was also solved by Jaeger (1942) up to a Fourier number of 25,000. Single cylinder grids with a superimposed temperature of 35°C were coded for both finite elements (Figure 11) and finite difference (Figure 20). The finite difference model did not use symmetry. Although this allowed better FD boundary condition imposition of constant temperature at all pipe locations, the improvements were not significant. Figure 21 shows the transient results for both numerical methods. The FD heat extractions were always higher than the Ingersoll solution, while the FE was more accurate. The FE

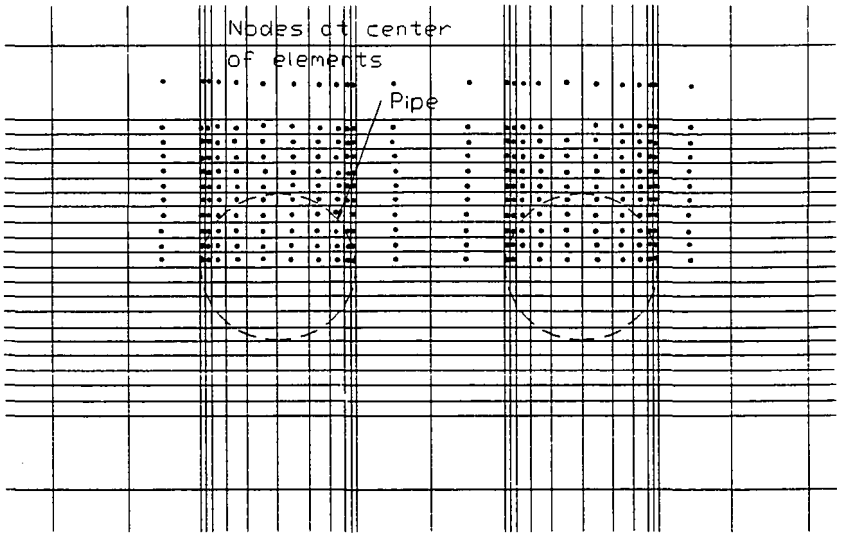

Figure 20. FD constant temperature stair-step approximation of circular pipes (0-$3r_o$ in grid of $400r_o$)

heat transfer was within 3% excess error of the solution for times greater than five minutes.

IV.4.1 Error Analysis

There were several reasons why FE was more accurate than FD. The FE method was more accurate as the heat transfer became more complicated partially because the FE method had a superior method of imposing a temperature on a single elemental surface area. In addition, the FD grid approximation of boundary conditions was limited to orthonormal elements (Figure 20). Therefore, with the FD stair-step approximation of the cylindrical surface, the surface area was much greater than that of a circle. As a result, the heat transfer rate (proportional to surface area) was unrealistically high.

There were other minor causes for less accuracy in FD (minor because they did not significantly influence the single heat source). First, because orthonormal elements were used, the FD grid required the same fine mesh width even when their

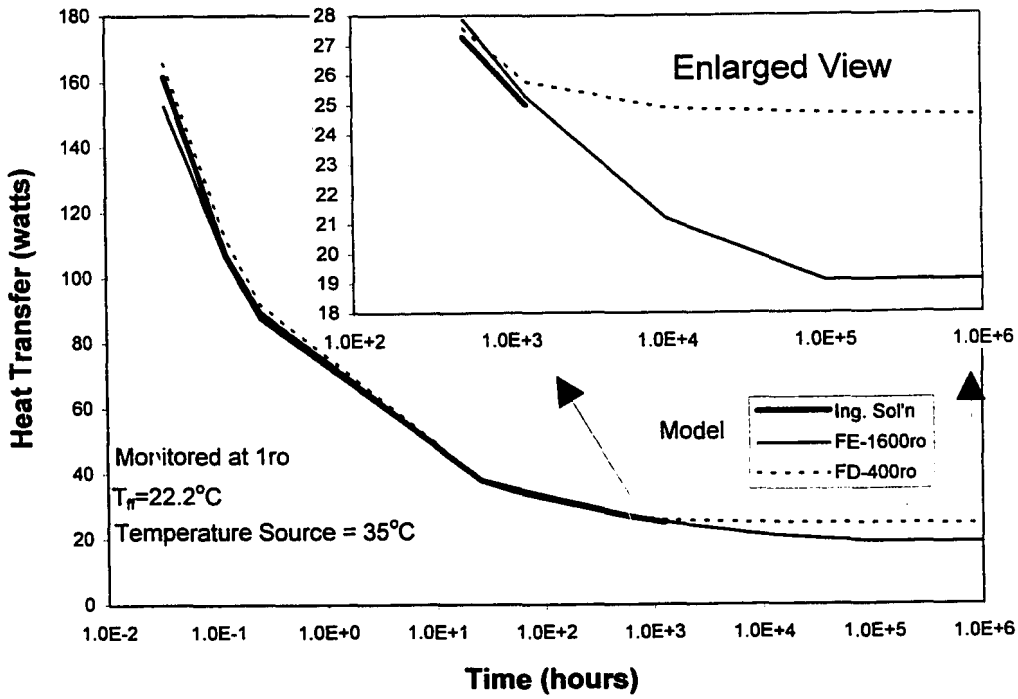

Figure 21. Transient single source constant temperature (35°C) for FD and FE

length had increased geometrically towards the farfield. Therefore, as previously mentioned, the length to width ratios were as high as 400 to one. Second, the FD farfield distance from the origin to 400 radii had to be represented by the larger square area containing this circle. Therefore, the excess area caused more numerical roundoff error, and longer execution time. In addition, FD symmetry was not used (by choice) to reduce the mesh size in half. As a result the FD grid size incorporated a farfield boundary of only $400r_o$ while utilizing 2600 nodes. By comparison, the FE model used 223 nodes and achieved a farfield location of 1600 radii. Consequently, the FD model took twice as long to execute and was less accurate.

The FD model had two advantages over FE. The model and computations were simple and intuitive. Another advantage was that the model was dimensionless, and used the Fourier number for time. This allowed easy switching between metric and English units or comparisons with other related problems.

IV.5 Dual Cylindrical Constant Temperature

Both numerical schemes were set up to simulate twin cylindrical temperature sources. However, the author could not locate analytical solutions for transient or steady-state values. Therefore, this phenomena was examined in the next chapter.

IV.6 Summary

In this chapter, the FE and FD heat transfer models were validated with the analytical solutions for U-value, single source heating, single source constant temperature, and dual source constant temperature.

The large variation in U-values rendered the method too simplistic for transient heat transfer. In simulating a constant temperature source, the FD method was slightly more accurate than FE. For both models the steady state temperature deviation from the Claesson solution (about 4.3°C for FE) was higher than the transient deviation from the Ingersoll solution (about 0.6°C for FE). Larger farfield boundary locations allowed longer simulation times before the temperature tapered off. However, for any given boundary size, accuracy was improved with more nodes per element. The dual cylindrical source models deviated from the Claesson steady-state line solution by about 4.8°C. No transient solution was available. The single source constant temperature models yielded higher accuracies than for constant heat flux. The FE model had the lowest average transient error of about 0.6 watts/m. Overall, the FE model became more accurate than the FD model as the heat transfer modeling became more complicated.

CHAPTER V

APPLICATIONS OF THE HEAT TRANSFER MODELS

In the previous chapter, the finite element (FE) and finite difference (FD) heat transfer models were validated for problems with analytical solutions. This chapter applies the model to analyze thermal short circuiting between adjacent tubes, develop an equivalent diameter for multiple tube heat exchangers, and heat transfer with backfill. The first section discusses using the model to determine the equivalent diameter of a single tube that could produce the same heat transfer as a multiple tube heat exchanger. The next section examines thermal short circuiting between tubes. The spacing between sources is varied and an equation is developed to estimate the associated equivalent radius. Finally, the performance of common backfills is quantified.

V.1 Equivalent Diameter

Previous researchers with GCHPs have attempted to model the heat transfer from the ground coil with an "equivalent diameter" single pipe that would produce the same heat transfer produced by the multiple pipes found in the ground heat exchanger. The equivalent diameter simplified an insoluble multi-pipe heat pump configuration so that it was represented reasonably by the known single source solutions of Ingersoll et al (1948), Claesson and Dunard (1983), etc.

Claesson and Dunard (1983) are often credited with deriving an analytical expression for equivalent radius. The author located the steady-state dipole solution but no rigorous derivation of equivalent radius. However, on page 46, Claesson and Dunard (1983) argued that the equivalent diameter must be between one and two. Since their dipole solution used the natural logarithm of distance ($\ln(r)$), the median value of $\sqrt{2}$ minimized the maximum possible error to 8%. Therefore, they proposed an expression for equivalent radius as

$$r_{eqv} = \sqrt{n} r_o, \tag{56}$$

where

r_{eqv} = equivalent outside pipe radius,

n = number of pipes in loop bundle, and

r_o = outside radius of the nominal pipe.

Therefore, for two pipes, $r_{eqv} = \sqrt{2}r_o = 1.414r_o$.

Mei (1988) examined the transient equivalent radius approach for the water loop. He arrived at an average value of $1.3r_o$ over five days. His value was for two sources separated by rubber insulation. He used this equivalent diameter in the Reynold number to calculate a convective heat transfer coefficient and determine the entry water temperature. Mei concluded that the equivalent diameter was a function of

- type of model (constant heat flux or constant temperature),
- separation distance (influences short circuiting), and
- backfill material.

For the reasons above, there were complications in determining an equivalent diameter in the soil. Furthermore, one might only expect a meaningful equivalent diameter for phenomena observed far away from the twin source (distance$\gg$ than radii). However, in one reference, AIEE (1960), it was stated that 20% of the earth's thermal resistance was in the first six inches of soil around the pipe. For the case of a one-inch diameter pipe this distance would be ten radii. Therefore, analysis of heat transfer would probably require dual source analysis close to the tubes.

V.1.1 FE Numerical Analysis

V.1.1.1 Constant temperature

An attempt was first made to analytically determine the equivalent radius. There appeared to be two alternatives for developing an equivalent diameter. The

first is based on an equivalent outer surface area and the other is based on the cross sectional area of the pipe.

In the first case, the heat flux required to maintain a constant temperature on the outer boundary surface of the pipe is proportional to the surface mass to be heated. Under this assumption, the equivalent radius should be the $2r_o$ shown in Figure 22 because the surface area of two one-radius sources is equal to the surface area of one two-radii source, or

$$2 \cdot (2 \cdot \pi r_o) = 2 \cdot \pi(2 \cdot r_o) = 4\pi r_o. \tag{57}$$

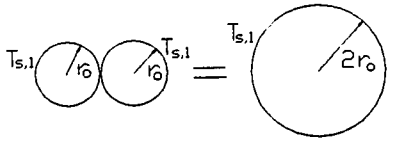

Figure 22. Boundary condition on surface

In the other case, the heat flux required to achieve a constant temperature throughout a disk area is proportional to the circular cross sectional area. Therefore, the equivalent radius may be calculated as $1.414r_o$ in Figure 23 because the area of two sources is equal to $\sqrt{2}$ times the area of one source, or

$$2 \cdot (\pi r^2{}_o) = (\sqrt{2}r_o)^2 \cdot \pi. \tag{58}$$

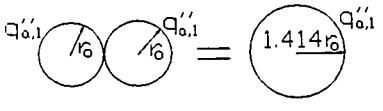

Figure 23. Boundary condition on cross sectional area

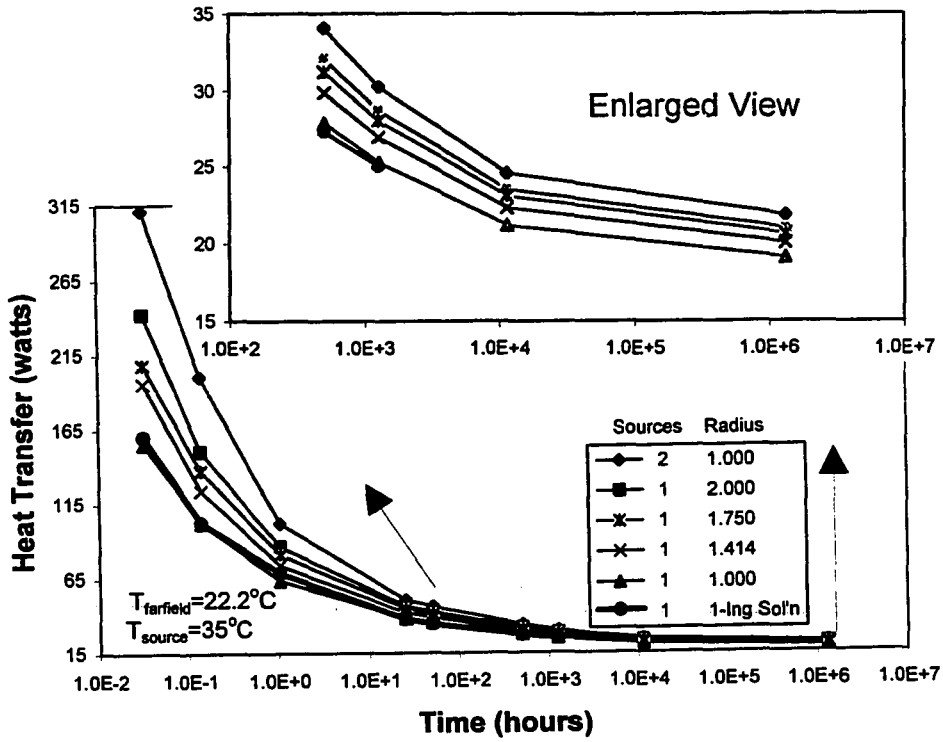

Figure 24. Heat transfer as a function of time and radius

This is the value frequently quoted in the literature by Claesson and Dunard (1983), etc.

The numerical model examined both of the constant temperature boundary conditions. The most elementary method of determining equivalent radius was to separately model sources of different radii. The simplified heat pump scenario was plotted in Figure 24 as two one-radius sources at the same temperature. The separation of the sources was set as 6.9 radii. Interestingly, the heat output was independent of whether the constant temperature was imposed only on the outer surface area, or both the outer surface area and three other inside surface areas. This was expected because the heat flux at 1.25 radii was monitored between the surface area at one radius and an arbitrary area at 1.5 radii. Therefore, imposing additional inside temperatures only caused the inside temperature to reach the imposed temperature faster.

Probably the reason most investigators used the $r_{equ} = 1.414r_o$ method was because they were modeling the water flow in the pipe while this study was examining the soil heat flux. Water flow heat balance was proportional to the mass of water which depended on the cross sectional area.

For completeness, the Ingersoll solution for the single source using one radius is shown in Figure 24. The same graph shows numerical heat output in the possible equivalent radius region of one to two radii ($1.414r_o$, $1.75r_o$, and $2.0r_o$).

The results in Figure 24 show that the equivalent diameter was not $1.414r_o$ at a separation distance of 6.9 radii. The heat transfer from all sources followed the same basic pattern of decreasing with time to converge in the range of 19-21 watts. In the transient region, the heat output appeared to be proportional to surface area which in turn was proportional to radius. Analytically, this was because more surface mass must be heated to impose a higher temperature. In addition, the perturbation of heat transferred to the soil was in "surface area front waves." Therefore, it was proposed that the equivalent radius *in the soil* for constant temperature should be a function of surface area under transient conditions. For this assumption, $r_{equ} = 2r_o$.

For all times, the two-source one-radius heat flux values in Figure 24 were closer to the two radius source than the $1.414r_o$. The simulated heat output of the two sources exceeded the two-radii source by 22% initially and decreased to 4% at steady-state. The steady-state value was approximately equivalent to a 2.5 radii source by extrapolation. The deviation of the $2.5r_o$ source was hypothesized to be caused by short circuiting due to the finite separation distance.

Unfortunately, there was no dipole solution for constant temperature given by Claesson and Dunard (1983) or anyone else, to the author's knowledge,

V.1.1.2 Assumptions for constant temperature sources

The model estimated heat flow as $Q = -k(T_1 - T_2)/(r_1 - r_2)$. For example, to estimate the heat flux at 18.5 radii for the grid shown in Figure 25, node set 1 would be at 15 radii while node set 2 would be at 22 radii. Then the energy would be summed from the two sets of nodes encompassing the semi-circle. However, for

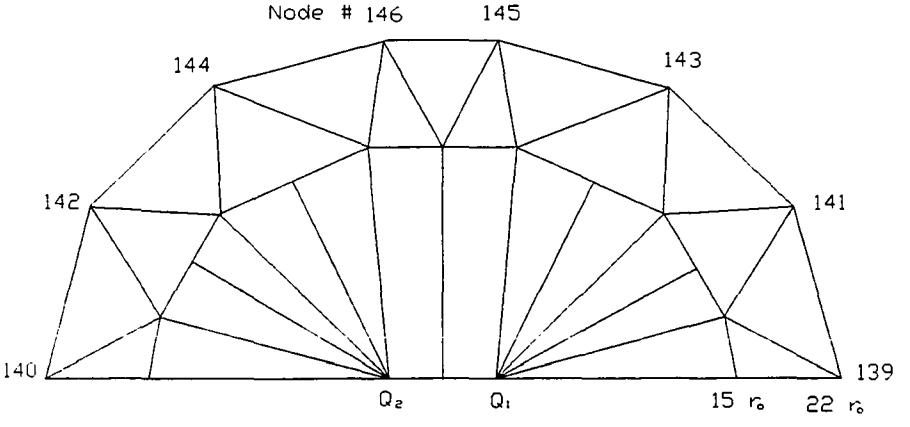

Figure 25. Grid for two constant heat sources

accuracy, the two sets of semi-circle nodes were always chosen to be radial as well as equi-distance (radially and angularly) from the source.

There was some ambiguity associated with the locations where the heat flow was calculated. The constant temperature boundary condition was imposed at the one radius location. While most of the resulting temperature perturbation traveled towards the farfield, some of it also heated the region inside the cylinder (until it reached the imposed temperature). As a consequence, there could be further complications when this model incorporated additional conductivities k for pipe material and backfill. These local phenomena were ignored in this simple model and the energy balances were taken between one and 1.5 radii. A comparison of heat flux summation from one radius to 1.5 radii versus heat from 1.5 to 2 radii yielded a difference of less than 1%.

V.1.1.3 Constant Heat Flux

Deriving an equivalent diameter in the soil for the constant heat flux was not straight forward. Quantifying the change in soil temperature was not as simple as quantifying net heat flux. Studies that examined the pipe interior for a water balance

often and more easily arrived at an equivalent diameter proportional to the cross sectional area $r_{eqv} = 1.414r_o$.

An attempt was made to examine temperature effect in the soil far away from the sources, so the effect of one or two sources could be compared. Two simulation models were prepared for a single source and a dual source, respectively. Both models dissipated a total and constant heat flux of 48.1 watts/m (the two source model consisted of two 24.05 watts/m sources). Figure 25 shows the two sources (Q_1 and Q_2) and the monitored nodes that are located 22 radii from each source (nodes 145 and 146). Both results were virtually identical for all times at $22r_o$, and the steady-state temperature was 40°C. The values at $10r_o$ were previously shown in Figure 13. In addition, the values were uniform (within three digits) directly above either source (node 145 or 146).

Because both the single source and the double source produced the exact same temperature at node 145/146, the dual source was exactly equivalent to the single source. As a consequence, no search for an equivalent diameter was necessary in a constant heat simulation of the ground temperature far away from the source. The resulting soil temperatures (far away from the source) were only dependent on the heat flux and not the shape or size of source.

V.2 Short Circuiting and Equivalent Diameter

V.2.1 Two Cylinder Leg Spacing

Heat pump installers should optimize leg spacing to minimize thermal interaction between adjacent legs. Low cost small bore holes with the legs touching have maximum short circuiting. Conversely, higher cost bigger diameter holes have large leg separation distances and less thermal short circuiting. The cost effective standard bore drills are 4, 6, and 8 inches in diameter (0.10-.20 meters). Therefore, thermal short circuiting as a function of separation distance must be quantified to determine optimal spacing.

A mesh grid with different pipe leg spacings was generated to simulate the thermal interaction between two legs. The grid whose origin is shown in Figure 26 had nine available source locations in the fine grid region range of -10 radius to +10 radius. The study consisted of imposing constant temperature boundary conditions (35° C) on two sources. The grid allowed simulation of separation distances ranging from 0 to 14 radius, which should encompass the reasonable range.

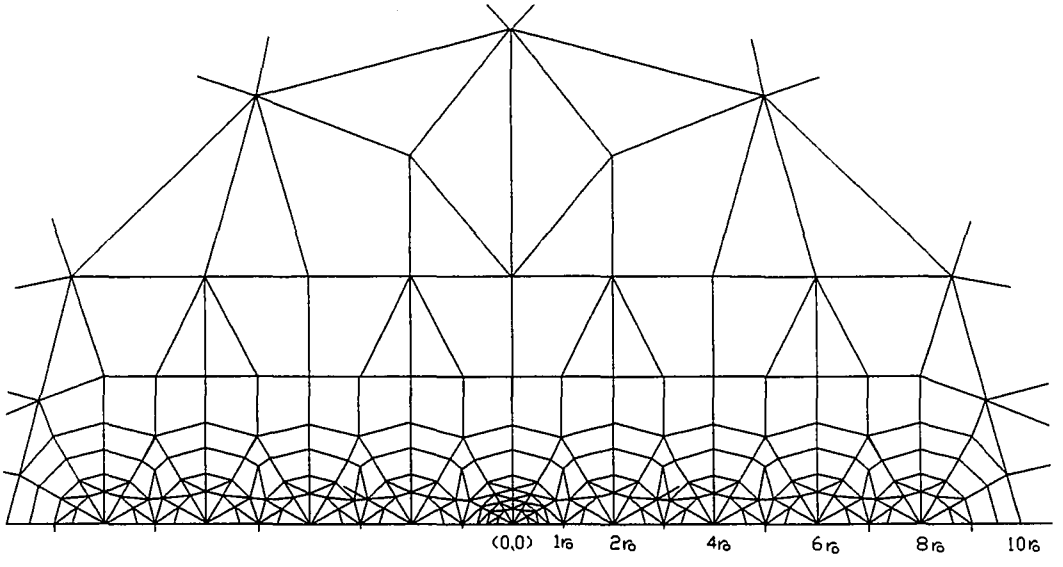

Figure 26. FE mesh grid with nine available source locations

The nine-source grid also extended to 1600 radii (21.3 m) like the previous two-source grid. In comparison, the nine-source model required 150% more nodes, and 114% more elements. In addition, quadrilateral elements were used (along with triangular elements) for two reasons. First, quadrilaterals allowed a more regular and

thus easier automated grid generation at distances far from the radius as is shown in Figure 27. Secondly, in theory, quadrilateral elements could mirror symmetry better, which improved the accuracy of the FE solution. Therefore, quadrilateral elements were used.

However, no boundary conditions could be imposed on quadrilaterals. Such an option would take a substantial amount of coding and was not required because triangles better approximated complex boundaries. Therefore, triangles were used for the elements with boundary conditions at the sources and on the outer layer at 1600 radii. The quadrilateral enhanced grid yielded similar accuracies as the triangular grid. However, the algorithm to generate the elements for the range from 22 radii to 1100 radii was much simpler and incorporated less elements.

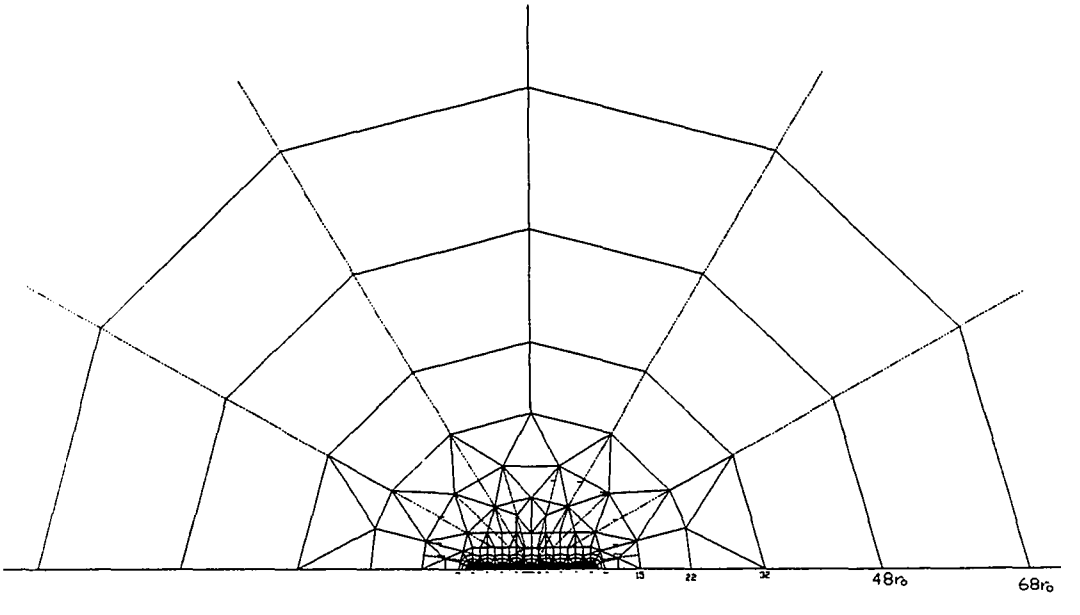

Figure 27. Use of quadrilateral four-node elements to extend grid

The major variables for the separation distances and heat flux short circuiting were non-dimensionalized. Two non-dimensional separation parameters were presented in Figure 28: $x_{sep} = (x + 2r_o)/r_o$ or $x_{sep} = l/D_o$. The l/D_o parameter passed through zero, had a shorter range and was simpler to conceptualize.

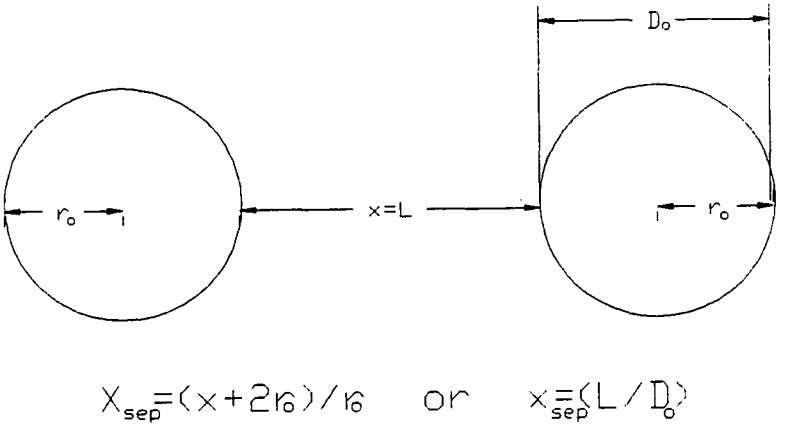

Figure 28. Non-dimensional separation parameters, $x_{sep} = (x + 2r_o)/r_o$ and l/D_o

The grid in Figure 27 allowed examination of separation distances of 0 to 14 radii. The maximum pipe separation was limited by two factors. First, since the two pipe legs must communicate, they are usually connected at the bottom and then inserted into the same bore hole. Spacers were required to maintain a constant separation distance. Secondly, it was only cost effective to use standard bore hole sizes. Heat pump pipes had typical outer diameters of 2.7cm (1 inch nominal pipes) and standard bore holes ranged from 10 to 20 cm. Therefore, the economical operation separation range was only 0 to 13 radii (l/D_o=6.6). Figure 29 shows the associated x_{sep} parameters in the valid range. A larger range of over 14 radii would have required

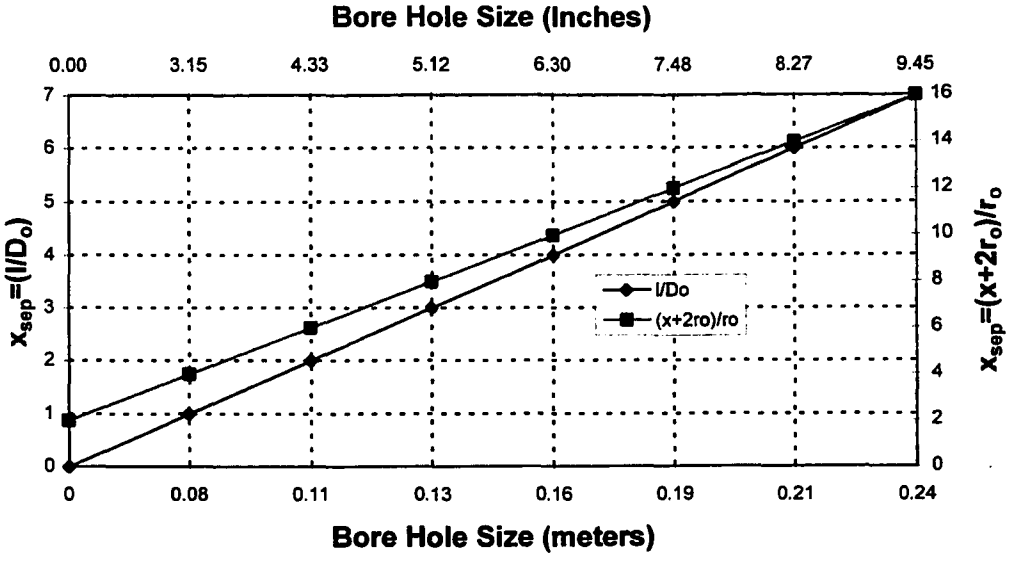

Figure 29. Separation parameters for one-inch nominal pipes (2.7cm o.d.)

using a more expensive bore hole, or drilling two parallel bore holes and establishing communication at the bottom of the holes.

Another non-dimensional variable, the heat exchanger effectiveness (ε_Λ), was developed to help in the evaluation of heat transfer for the legs. The heat exchanger effectiveness (ε_Λ) was defined as the ratio of the actual heat transfer rate to the maximum possible heat transfer without thermal interaction (Incropera and DeWitt, 1985). To quantify thermal short circuiting, heat exchanger effectiveness was given as:

$$\varepsilon_\Lambda = \frac{Q_{\text{actual}}}{Q_{\text{max}}} = \frac{Q_{\text{short circuiting}}}{Q_{\text{isolated}}} = \frac{Q_{1+2,\text{ net}}}{Q_{1,\text{ isolated}} + Q_{2,\text{ isolated}}} \tag{59}$$

ε_Λ was the ratio of the heat transfer to the ground from two simultaneous sources to the sum of heat transfer if the two sources were independent isolated sources. In the limit as the separation distance increases, $Q_{1+2,net}$, approached the sum $(Q_{1,isolated} + Q_{2,isolated})$. Therefore, ε_Λ approached unity.

The thermal short circuiting (Λ) was defined as the complement of heat effectiveness:

$$\Lambda = 1 - \varepsilon_\Lambda = 1 - \frac{Q_{1+2,net}}{Q_{1,\,isolated} + Q_{2,\,isolated}}. \tag{60}$$

The potential heat loss was a maximum for touching sources of different temperatures. As the separation distance increased, thermal interaction decreased and Λ approached zero.

The thermal ratios for two equal temperature sources at 35°C are shown in Figure 30 for separation parameters $x_{sep} = l/D_o$ and $x_{sep} = (x + 2r_o)/r_o$. The generation of each data series required three simulations. First, T_1 was imposed to yield $Q_{1,isolated}$. Second, T_2 was imposed to yield $Q_{2,isolated}$. Finally, both T_1 and T_2 were imposed simultaneously to obtain $Q_{1+2,net}$. As the separation distance increased, ε_Λ increased from 52% to 62%, while Λ decreased from 48% to 38% (for the grid size of $1600r_o$). The effectiveness increased by 10% from a zero separation to four radii, and then only decreased by another 10% over the remaining 10 radii.

Grid size had only a small influence on thermal effectiveness. Figure 30 shows the variation in both ε_Λ and Λ with both separation distance and grid size. Decreasing the grid size by 30% to 1100 radii only increased ε_Λ by a maximum of 1% at a separation of 14 radii. The reason for this was that increased heat flux at 1100 radii dominated changes in thermal source interaction. The Fourier heat conduction equation was $Q = -k(T_1 - T_2)/(r_1 - r_2)$. In this problem, T_2 was imposed at $r_2 = 1600r_o$ while T_1 was at $r_1 = 1r_o$. Therefore, decreasing the distance $\overline{r_2 - r_1}$ increased the heat transfer rate which increased ε_Λ (and decreased Λ).

There was substantial thermal short circuiting throughout the separation range of 0 to 14 radii. Even at 14 radii, installers should compensate with 38% over-sizing based on single coil calculations. In addition, attempts should be made to allow a minimum separation of four radii to increase ε_Λ by 10%. However, there was a larger cost associated with the larger separation due to the larger drilling costs.

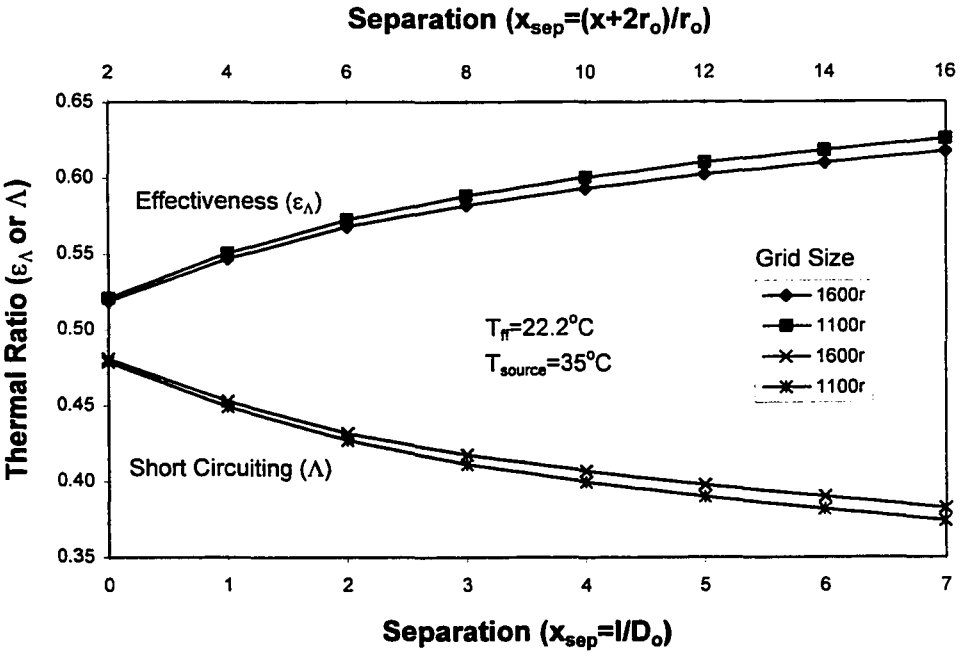

Figure 30. Thermal effectiveness and thermal short circuiting vs separation distance and grid size

V.2.1.1 Equivalent Radius

The theoretical equivalent radii were previously derived for constant heat transfer ($\sqrt{2}r_o$) and constant temperature sources ($2r_o$). Both results were compared with analytical and numerical models for various separation distances.

An analytical geometric equivalent radius can be derived using Fourier's heat conduction equation in cylindrical coordinates,

$$Q_1 = \frac{2 \cdot \pi Lk(T_{s,1} - T_{s,\infty})}{ln(r_\infty / r_1)}. \tag{61}$$

For a typical heat pump scenario, there are two pipe (cylinders) at the origin and a farfield constant temperature. The two concentric cylinders are shown in Figure 31. Because $r_\infty \gg r_1, r_2$, and $r_{g,eqv}$, the inner cylinders are virtually concentric with

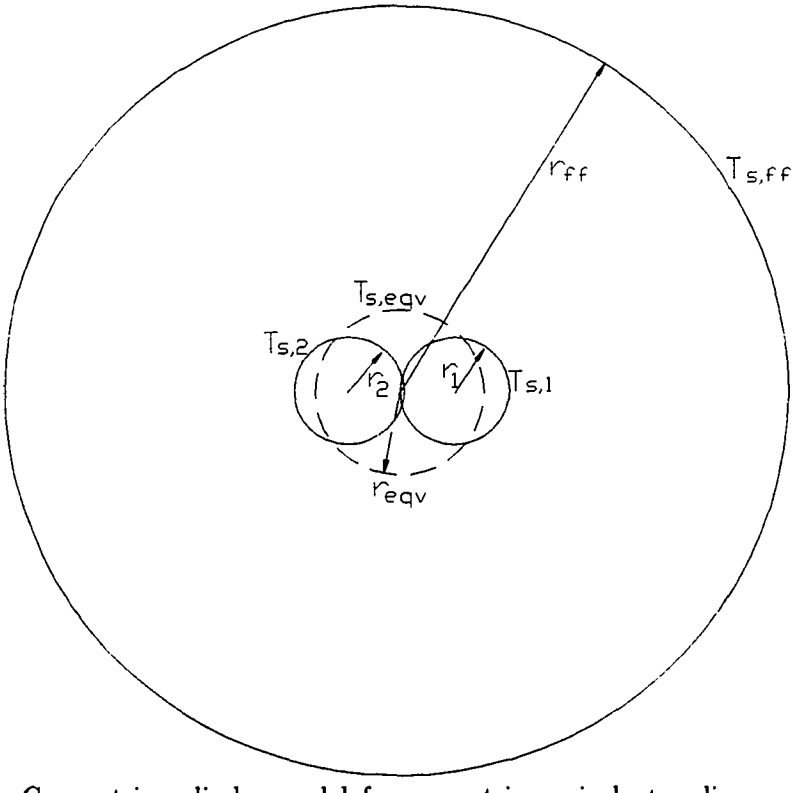

Figure 31. Concentric cylinder model for geometric equivalent radius r_{eqv} of two sources

the farfield cylinder. The equivalent single source is theoretical and unrealistic for analyzing phenomena close to the origin.

A geometric equivalent radius can be derived from the equivalent heat fluxes. The ratio of a heat source to the equivalent heat source can be written from Equation 61 as

$$\frac{Q_1}{Q_{eqv}} = \frac{2 \cdot \pi Lk(T_{s,1} - T_{s,\infty})/ln(r_\infty/r_1)}{2 \cdot \pi Lk(T_{s,eqv} - T_{s,\infty})/ln(r_\infty/r_{g,eqv})}. \tag{62}$$

If $T_{s,1} = T_{s,2} = T_{s,eqv}$, then,

$$\frac{Q_1}{Q_{eqv}} = \frac{ln(r_\infty/r_{g,eqv})}{ln(r_\infty/r_1)}. \tag{63}$$

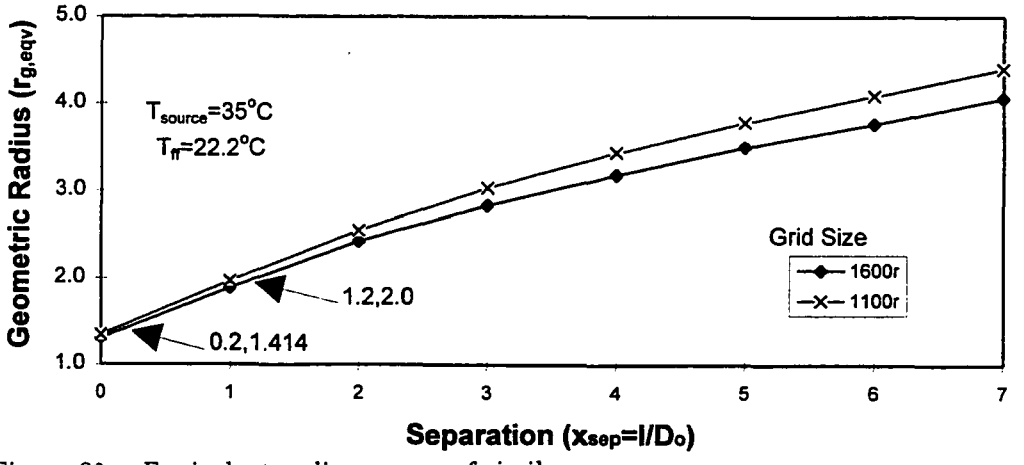

Figure 32. Equivalent radius, $r_{g,eqv}$, of similar sources

Equation 63 can be used if an equivalent radius is assumed (or possibly known). If one uses the common assumption that $r_{eqv} = \sqrt{2}r_o$, and an FE grid of $1600r_o$, then $Q_1/Q_{eqv} = 0.953$, $\varepsilon_\Lambda = Q_{eqv}/(Q_1 + Q_2) = 0.525$, and $\Lambda = 1 - \varepsilon_\Lambda = 0.475$. This analytical solution can be compared with the numerical values from Figure 30 at an l/D_o of zero: $Q_1/Q_{eqv} = 0.963$, $\varepsilon_\Lambda = 0.519$, and $\Lambda = 0.481$. Therefore, the analytical and numerical solutions agree within 1.2%. This strong agreement verifies the use of $r_{eqv} = \sqrt{2}r_o$ when two source are touching.

Unfortunately, the analytical solution cannot adjust for varying separation distances when $r_{eqv} \neq \sqrt{2}r_o$. However, an Equation can be derived which will yield an equivalent radius from the numerical or experimental equivalent heat transfer. Equation 63 can be simplified to

$$\frac{r_\infty}{r_{g,eqv}} = exp\left(\frac{Q_1}{Q_{eqv}} \cdot ln(r_\infty/r_1)\right),$$

and using the definition that $a^x = e^{xlna}$ for all $a > 0$ and x real,

$$r_{g,eqv} = \frac{r_\infty}{(r_\infty/r_1)^{(Q_1/Q_{eqv})}}. \tag{64}$$

The geometric equivalent radius, $r_{g,eqv}$, extracted by Equation 64 from computational output was plotted in Figure 32 for grids of $1600r_o$ and $1100r_o$. The values at $1600r_o$ ranged from $1.31r_o$ for touching sources to $4.07r_o$ at an l/D_o of 7. The value of $\sqrt{2}r_o$ corresponds to an l/D_o of 0.18, while the value of $2r_o$ corresponds to an l/D_o of 1.21.

The geometric equivalent radius $r_{g,eqv}$ was abandoned for three reasons. The definition ignored the fact that Q_2 was not equal Q_1 and T_2 was not equal T_1. Also, $r_{g,eqv}$ was not unique (depended on the grid size), and there was no asymptotic limit. Equation 64 asymptotically approaches $40r_o$ for a grid size of $1600r_o$ and $33r_o$ for a grid size of $1100r_o$.

An alternate approach was developed for the equivalent radius based on the heat flux. A heat flux equivalent diameter $r_{h,eqv}$, was defined as the ratio of the equivalent heat transfer to the average isolated heat transfer:

$$r_{h,eqv} = \frac{Q_{eqv}}{(Q_{1,isolated} + Q_{2,isolated})/2}. \tag{65}$$

The minimum value was one and the maximum was two. Therefore, the asymptotic limit for two sources separated by a sufficient distance to negate short circuiting was two. The results are plotted in Figure 33 and can be compared with Figure 32. While the grid size still affected the number of equivalent sources, the asymptotic limit remained two.

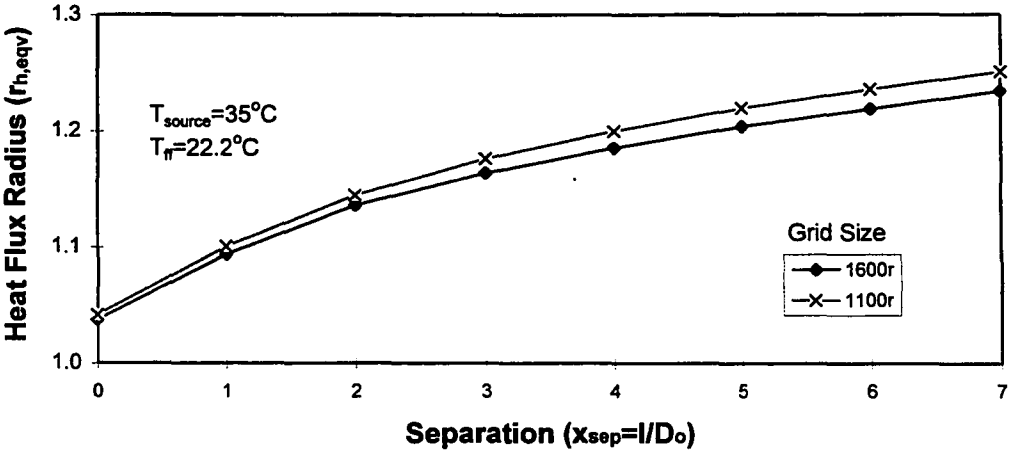

Figure 33. Equivalent heat flux radius $r_{h,eqv}$ of similar sources

Significant error could result from using $r_{h,eqv} = \sqrt{2}$ with separated sources. The equivalent radius of $\sqrt{2}r_o$ implies $Q_{eqv}/[(Q_1+Q_2)/2] = \sqrt{2}$. As separation ranged from l/D_o=0 to 7, the FE model $r_{h,eqv}$ as the ratio $Q_{eqv}/[(Q_1 + Q_2)/2]$, ranged from 1.05 to 1.23. Therefore, the Claesson solution would overestimate the heat transfer by 36% to 18%.

In conclusion, neither the author's constant temperature source, $r_{eqv} = 2r_o$, nor the common constant heat source $r_{eqv} = \sqrt{2}r_o$ was valid for all radii. This conclusion was not surprising as r_{eqv} must vary with separation because short circuiting is a function of separation distance. As a result, the constant equivalent diameter method approximated touching sources, but had only limited application as a rough estimate for separated sources. The geometric equivalent diameter was computed and verified mathematically. Unfortunately, it was highly dependent on the grid size, r_∞. Therefore, it was necessary to define a heat flux $r_{h,eqv}$ to yield the number of equivalent sources. In addition, short circuiting was defined and computed at various separation radii.

Heat dissipation at selected leg spacing distances could also be compared with other numerical models (such as the transient FD model of Dobson (1991)) as well as experimental monitoring sites.

V.2.1.2 Different Temperature Sources

In actual operation, the two heat pump legs operate at different temperatures. For example, during operation in July, 1990, temperatures from the heat pump installation in Abilene, Texas, averaged 33.1°C for entry water, and 28.4°C for outdoor air (Dobson, 1991). In the heat of the day, typical exit temperatures exceed 35°C. As a result, simulations were performed for an exit temperature of 37.8°C and a return temperature from the ground of 32.8°C. Since there were three sets of twin pipe legs, this represented the maximum possible temperature difference between legs. However, the author postulated that actual adjacent pipe leg temperatures differences should only be one or two degrees (in a three hole system this amounts to 3-6°C total).

Table 2. Parameters and results for different temperature sources

Source r-location	l/D_o	37.8°C Q_{hi}	32.8°C Q_{lo}	Q_{hi+lo}	Effectiveness ε_Λ	Short Circuiting Λ	r^*_{eqv}
-2,-4	0	23.05	15.71	21.34	0.551	0.449	1.101
-4,-8	1	23.13	15.88	22.22	0.570	0.430	1.139
-2,-8	2	23.08	15.88	22.86	0.587	0.413	1.174
+6,-2	3	23.05	15.66	23.58	0.609	0.391	1.218
+6,-4	4	23.05	15.71	23.99	0.619	0.381	1.238
+6,-6	5	23.05	15.70	24.33	0.628	0.372	1.256
+6,-8	6	23.05	15.88	24.63	0.633	0.367	1.265
+8,-8	7	23.35	15.88	25.07	0.639	0.361	1.278

Temperatures of 37.8°C and 32.8°C were inserted into the model to calculate thermal short circuiting and equivalent radius.

Table 2 shows the steady-state parameters and results from heat flux monitored at $40r_o$. The heat output with both T_{hi} and T_{lo} imposed is labeled as Q_{hi+lo}. The combined heat output increased with separation distance.

The transient and steady-state thermal effectiveness, ε_Λ, is shown in Figure 34. The effectiveness increased with separation as expected. The range was from 55% for touching sources, to 62% at an l/D_o of 7. The transient ε_Λ curves in Figure 34 were labeled with heat flux locations of one radius, with one exception of 40 radii. The mesh shown in Figure 26 provides circumferential radial nodes for temperature monitoring around each source (at the surface and at 1.5 radii). However, for touching sources the nodes at 1.5 radii overlap and the next available radial node distribution is at 40 radii. However, temperature gradients took 51 hours to reach 40 radii.

The definition of geometric equivalent radius in Equation 64 did not designate which of the two dissimilar temperatures should be used. Arbitrarily, the high source was chosen. Therefore, the single radius at T_{hi} that would produce the equivalent heat flux was

$$r_{hi,g,eqv} = \frac{r_\infty}{(r_\infty/r_1)^{(Q_{hi}/Q_{eqv})}}. \tag{66}$$

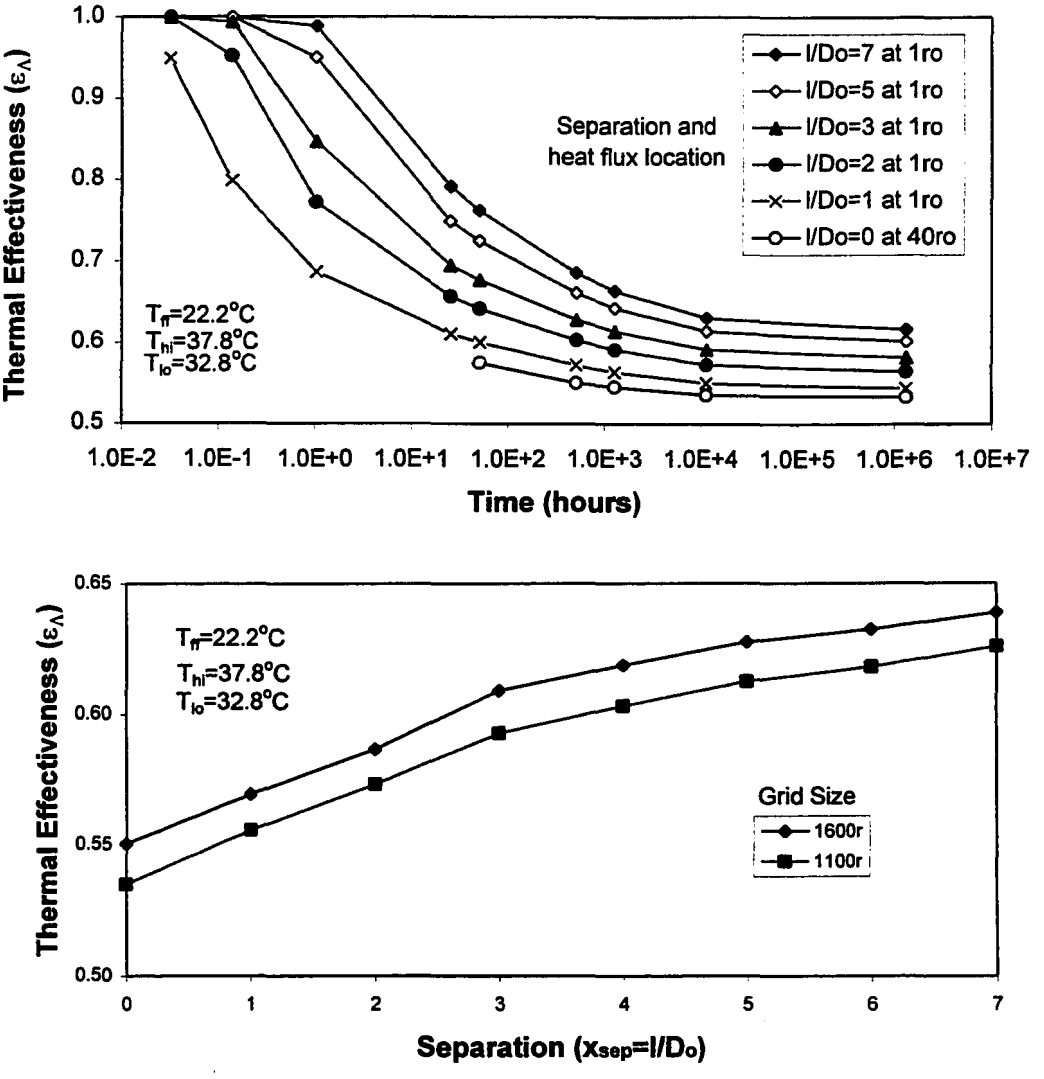

Figure 34. Thermal effectiveness ε_Λ for different sources (above) transient and (below) steady-state

The transient equivalent radius, $r_{hi,g,eqv}$ was plotted in Figure 35, while the steady-state values were graphed in Figure 36. The equivalent radius decreased with time and the steady-state range was from two to five radii (at $1600r_o$). The transient nature of the equivalent diameter caused complications in its use. Only after thousands of

operating hours (steady-state) were the commonly cited equivalent radii approached. The commonly cited r_{eqv} of 1.414r_o would occur at an l/D_o of 0.56, while the alternative r_{eqv} of 2.0r_o occurred at 0.42 l/D_o.

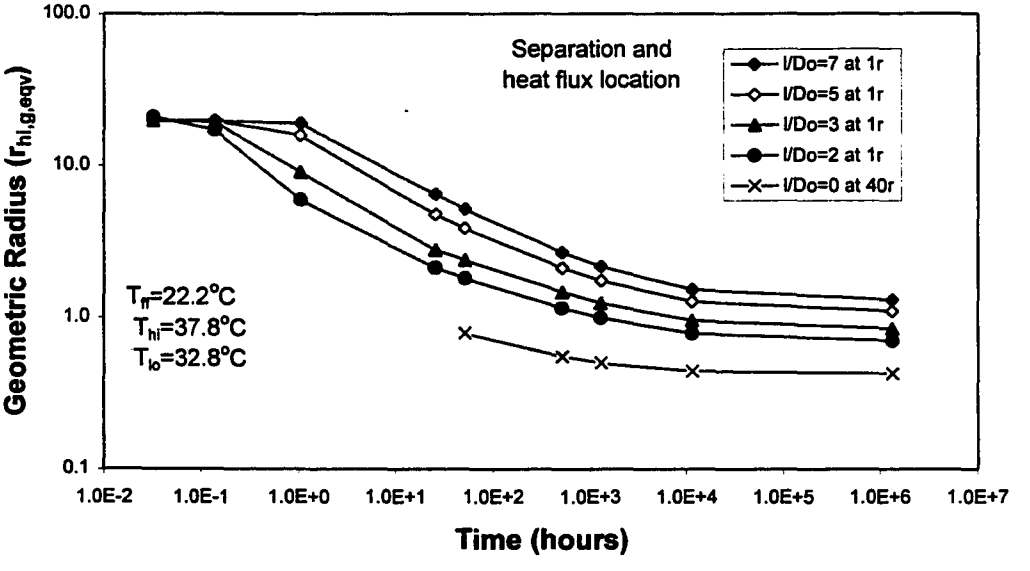

Figure 35. Transient geometric equivalent radius $r_{hi,g,eqv}$ for different sources

The preferred heat flux equivalent radius, $r_{h,eqv}$, was plotted in Figure 37. The range of values was from 1.1 at an l/D_o of zero to 1.28 at an l/D_o of seven (at 1600r_o). This curve had a similar shape to the $r_{h,eqv}$ of the same temperature sources in Figure 33. However, the different temperature $r_{h,eqv}$ was higher by 2% to 7%. In addition, decreasing the grid size to 1100r_o decreased $r_{h,eqv}$. The reason for this was that changing the grid size had a larger effect on individual sources than on net sources with short circuiting. Decreasing the grid size by 30% to 1100r_o increased $Q_{1,isolated}$ and $Q_{2,isolated}$ by 9%, while $Q_{1+2,net}$ only increased by 6%.

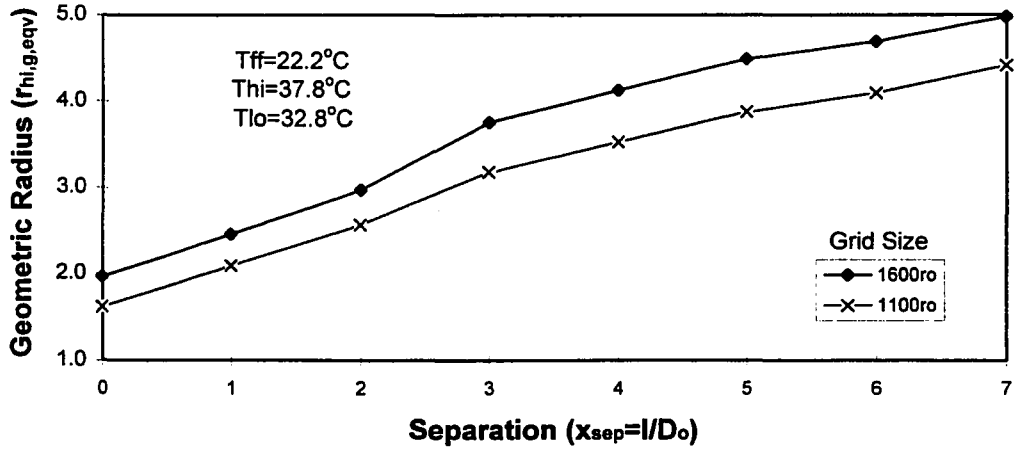

Figure 36. Steady-state equivalent geometric radius $r_{hi,g,eqv}$ for different sources

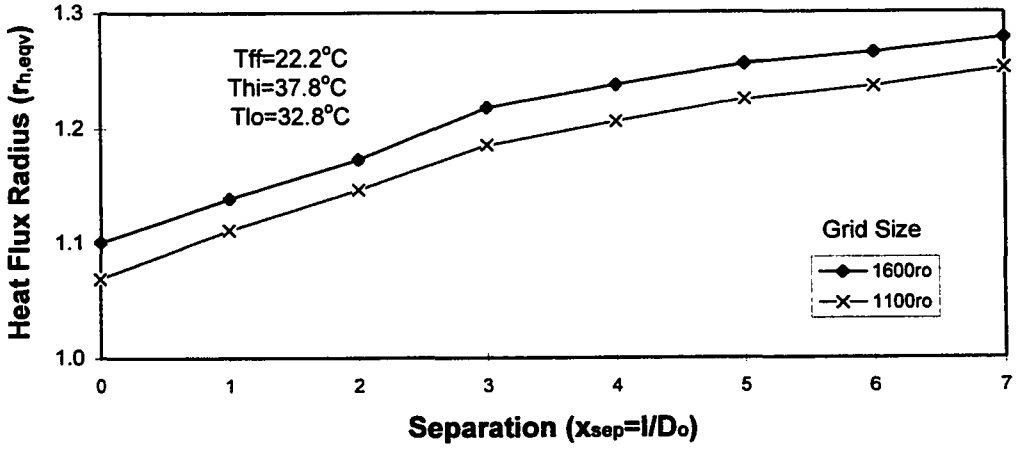

Figure 37. Steady-state heat flux equivalent radius $r_{h,eqv}$ for different sources

The discrepancy resulting from using Claesson's solution was also computed for both $r_{hi,g,eqv}$ and $r_{h,eqv}$. The error was a minimum for touching sources and increased with separation. The deviation of Q_{eqv} computed from $\sqrt{2}r_o$ for $r_{hi,g,eqv}$ ranged from

-5% to -21%. And the deviation from $r_{h,eqv}$ ranged from +9% to +22%. Therefore, the Claesson solution underestimated $r_{hi,g,eqv}$ and overestimated $r_{h,eqv}$.

V.2.2 Effect of Temperature on Short Circuiting

The temperatures of the heat pump coils and ground vary with operation and seasons. Therefore, short circuiting should be examined as a function of these temperatures. The possible variation of temperature can be consolidated into two categories: variation of the ground temperature from the coil temperature, and variation of the temperature difference between the adjacent coils.

The variation of ground temperature was analyzed in the possible range of 0 to 30°C. Below 0°C, moisture in the soil would freeze and the model was not configured to handle phase change. The outdoor temperature in contact with the top soil layer might be as high as 50°C. However, below the surface soil temperatures would not be expected to exceed 30°C and T_{low}=32.8°C must be above $T_{farfield}$=30°C. The results in Figure 38 show that thermal effectiveness estimated with the finite element program did not vary by more than 2%. Therefore, it can be concluded that the effectiveness was independent of the farfield temperature at all separation distances within the temperature range of 0 to 30°C.

The other possible temperature variation was between the two adjacent coils. The interaction of thermal effectiveness and coil temperature difference was plotted in Figure 39. The higher coil temperature was maintained at 35°C while the return coil temperature varied from 35 to 22.2°C (T_{ff}). The maximum variance was 3% at l/D_o=3. Therefore, ε_Λ appeared to be independent of the farfield temperature at all separation distances within the temperature range of 0 to 30°C. One should note that the variations were smaller than the 4% FE model accuracy from comparison with the Ingersoll solution. However, the FE model consistently under predicted values as the convergence was approached by refining the grid. Therefore, the variation pattern should be correct while the values were consistently under predicted.

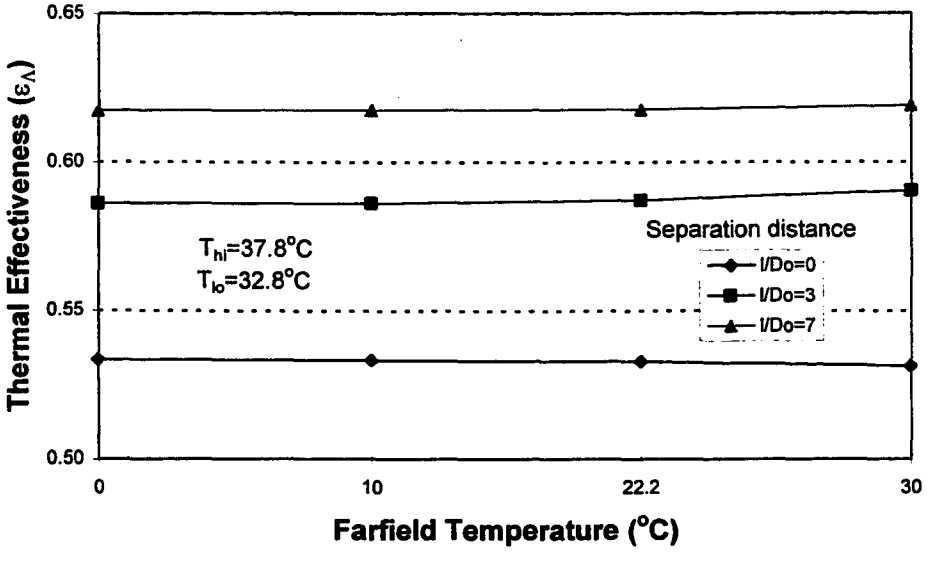

Figure 38. Effect of farfield temperature on thermal effectiveness

The two curves in Figures 38 and 39 were combined by defining a dimensionless temperature:

$$\varphi_T = \frac{T_{hi} - T_{lo}}{T_{hi} - T_{ff}}. \tag{67}$$

The overall effect of temperature variation on thermal effectiveness was plotted in Figure 40. The curves duplicated those in Figure 39. These were also congruent curves (same values) for T_{ff}=15, 20, and 25°C, within two decimal points. Therefore, within the operating range examined, ε_Λ was only a function of dimensionless temperature φ_T. This was an important and useful conclusion because it allowed prediction of effectiveness for any given temperatures. Table 3 presents the generalized numerical thermal effectiveness as a function of separation and dimensionless temperature.

V.2.3 Numerical Validity- Heat Balance

The energy balances for the nine-source FE model were examined. Validity of a numerical model required conservation of energy. The monitored heat fluxes at $1.25r_o$,

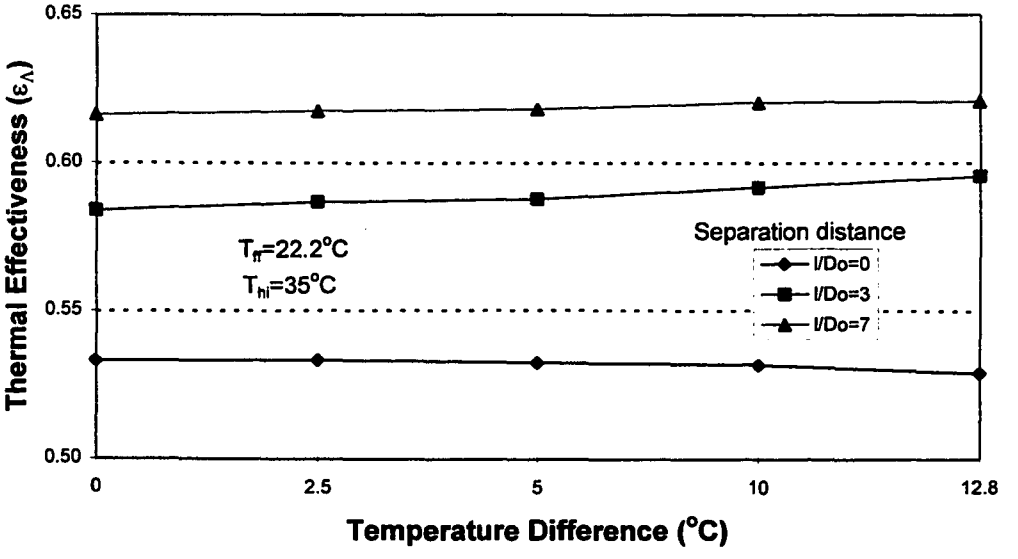

Figure 39. Effect of coil temperature difference on thermal effectiveness

$27r_o$, $53r_o$, and $84r_o$ are shown in Figure 41. The energy required a finite amount of time for a perturbation to reach the larger radii location. All values attained steady-state after 100,000 hours. An irregularity was observed at $27r_o$ which marked the transition from rectangular elements to quadrilateral elements. The steady-state temperature converged to 21 watts while the other three locations converged to 24 watts. As was usual for finite elements, the irregularity was localized and dissipated without affecting the rest of the grid. In fact, the discrepancy in heat flux between $1.25r_o$ and $84r_o$ was only 3%. The integrity of the model was satisfactory, especially in the region of $\pm 10r_o$ containing the measured phenomena of interest.

V.3 Backfill (Non-homogenous properties)

The thermophysical properties of the surrounding media impact the performance of a vertical heat exchanger. Heat pump installations include non-homogenous

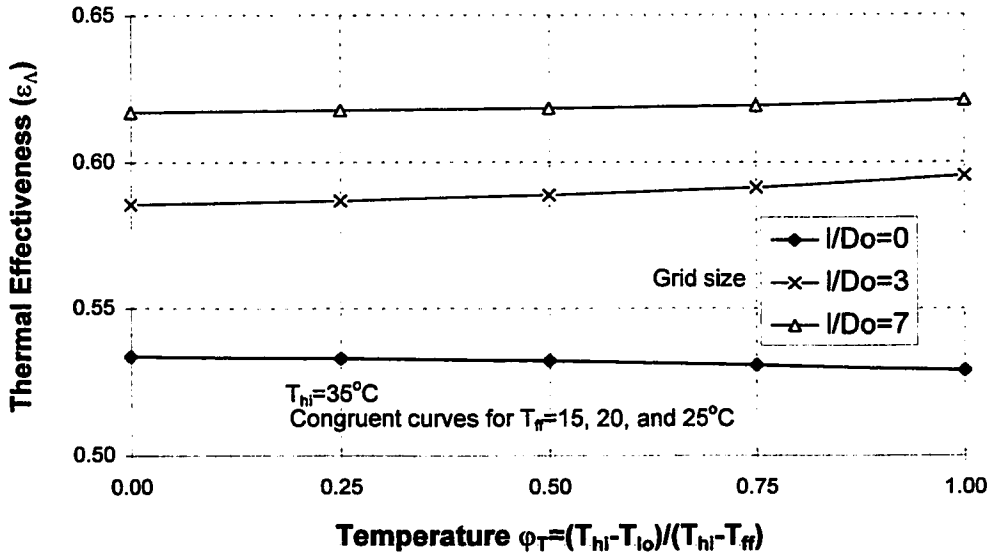

Figure 40. Thermal effectiveness as a function of separation and temperature

Table 3. Thermal effectiveness as a function of separation and temperature

Temperature	Thermal Effectiveness		
φ	ε_Λ	ε_Λ	ε_Λ
	l/Do=0	l/Do=3	l/Do=7
0.000	0.534	0.586	0.617
0.250	0.533	0.587	0.618
0.500	0.532	0.589	0.619
0.750	0.531	0.591	0.619
1.000	0.529	0.595	0.621
Average	0.53	0.59	0.621

materials of water, pipe, backfill, and various soil compositions. The numerical approximation of a heat exchanger with backfill is shown in Figure 42. Water, polyethylene pipe, backfill, and soil are all included.

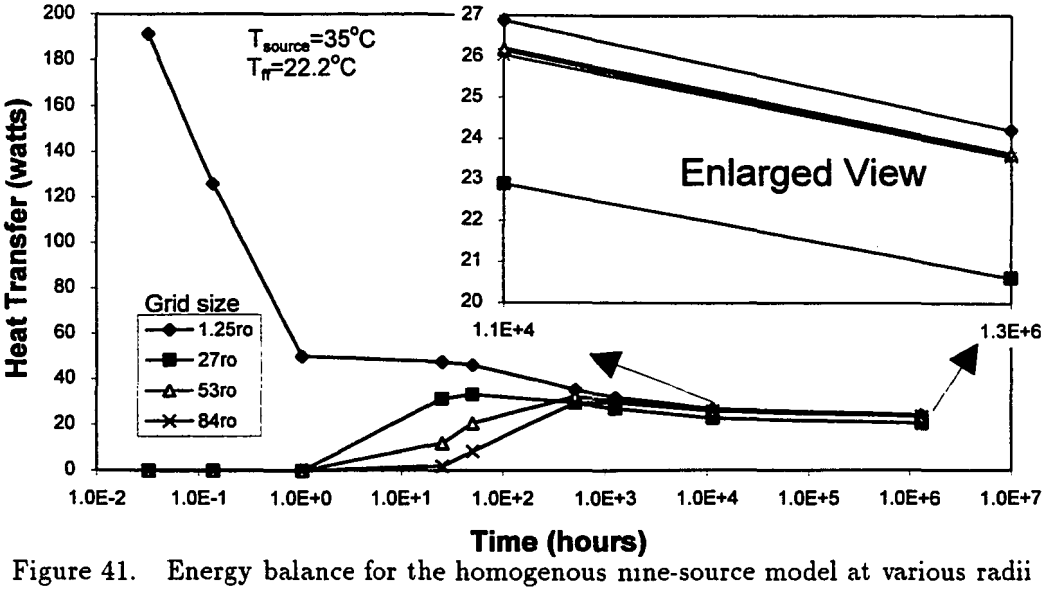

Figure 41. Energy balance for the homogenous nine-source model at various radii

Backfills are used to seal the drilled well and provide an efficient thermal bridge from the heat exchanger to the soil. The backfills examined were bentonite grouts which were commonly used with vertical heat pumps.

Laboratory tests were performed by Remund and Lund (1993) to determine the thermal conductivities of various bentonite combinations and the selected additives of quartzite, masonry sand, limestone, iron ore, mica flakes, barium sulfate and clay. The nine most common bentonite product labels were measured at various compositions of bentonite, water and catalyst (if required). Figure 43 shows that the thermal conductivities ranged from 0.6 to 0.9 W/(m-°C). In comparison, the conductivities of soils used in the design of GCHP systems ranged from 0.35 for light, dry soil to 2.42 W/(m-°C) for heavy, saturated soil. Bentonite without additives had a lower conductivity than all but light, dry soils.

The effect of thermal enhancing additives was also measured by Remund and Lund (1993). Additives are used to

> ... enhance the thermal characteristics of a bentonite grout by resulting in a mixture with high sustained thermal conductivity, low shrinkage coefficient, low susceptibility to drying

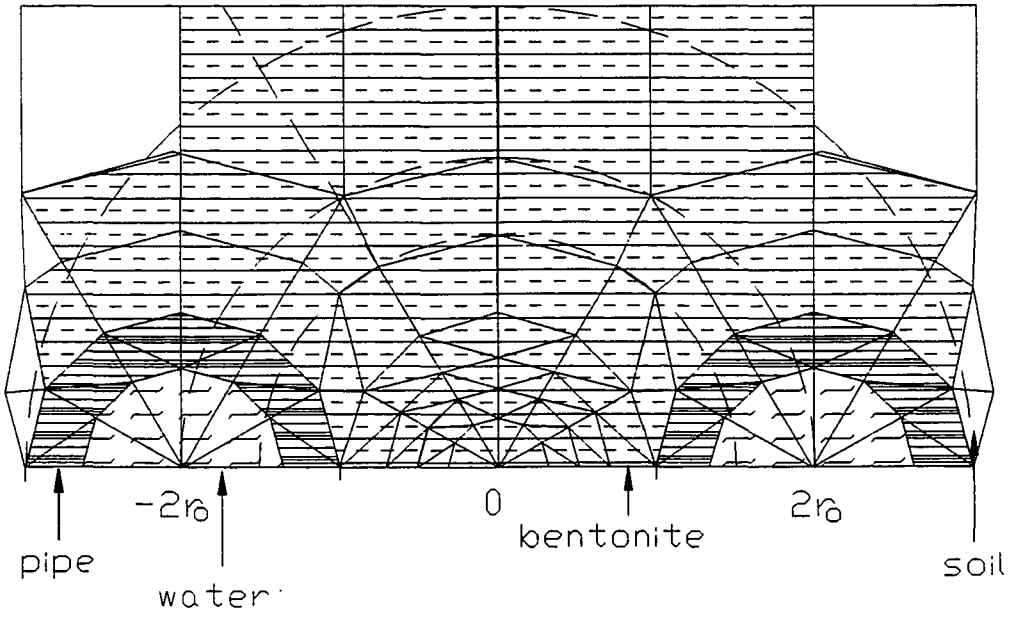

Figure 42. Non-homogenous material composition

> with capability of natural rewetting if dried, extremely low permeability, and pumpability characteristics that allow easy insertion into the bore hole. In addition, the additive must be readily available, economically justifiable, nontoxic, chemically inert, and nonpolluting with respect to the groundwater. (Remund and Lund, 1993)

The main chemical composition of bentonites was SiO_2 (54 to 64%), followed by Al_2O_3 which accounted for 14 to 20%.

Numerical simulations were performed with the four values of backfill thermal conductivity listed in Table 4: 0.782, 1.6, 8.65, and 1,000 W/m-K. Remund's experimental values for bentonite are a minimum of 0.782 W/m-K for pure bentonite. The Texas A&M installation at College Station utilized bentonite mixed with masonry sand. The measured thermal conductivity was 1.6 W/m-K, which was near Remund's maximum possible conductivity of 1.74 W/m-K with a 70% quartz mix. It should be noted that the bentonite and sand mixture thermal conductivities were lower than that of the soil. Because there was much room for improving backfill conductivity,

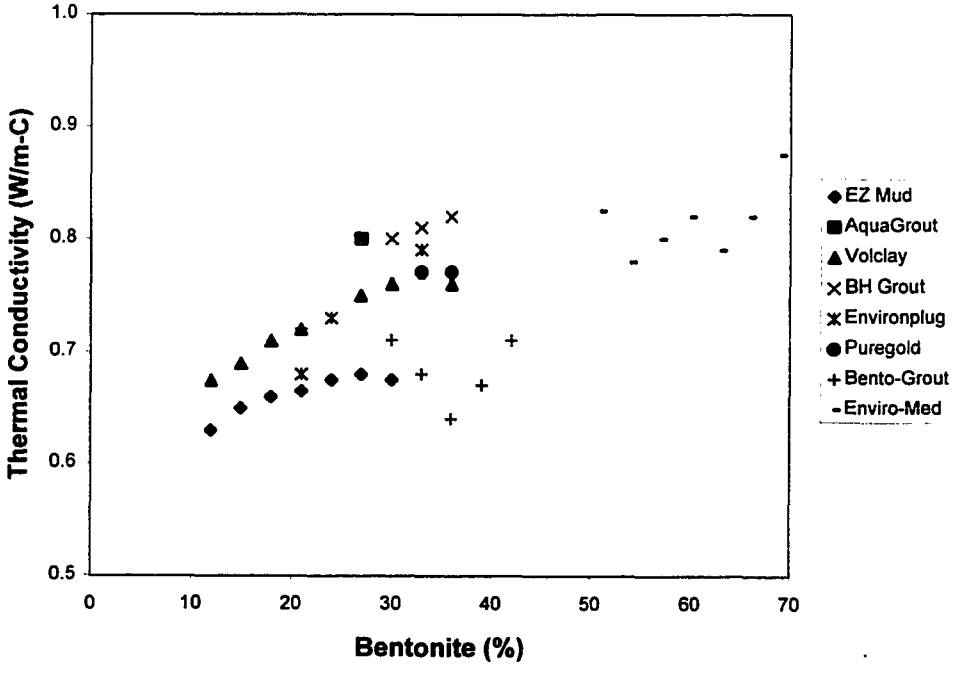

Figure 43. Thermal conductivity of bentonite grouts

8.65 W/m-K was selected to study the possible benefits. In addition, enhancing thermal conductivity affected the competing phenomena of increased heat transfer and increased thermal short circuiting. As a result, the maximum heat transfer for this FE grid was found to occur at 1,000 W/m-K. The four numerical simulations used the same backfill density and specific heat.

Three simulations were performed for each of the four backfill conductivities to determine Q_{lo}, Q_{hi}, and Q_{eqv}. The previously explained equivalent diameter parameters were also computed. The total heat transferred to the ground and monitored at 40 radii is shown in Figure 44. This deviation from the previous monitoring at one radius allowed realistic measurement of heat flow for touching sources. At all separation distances, increasing the thermal conductivity from 0.782 W/(m-°C) (0% sand) by 105% to 1.60 W/(m-°C) (60% sand) increased the heat

Table 4. Thermophysical data for non-homogenous grid

Material	k W/m-k	α m^2/sec	ρ Kg/m^3	Source
Water	0.613	1.32E-07	997	Incropera, (1985), Table A.6
Polyethylene	0.390	0.960E-07	2,200	Estimated
Soil	1.73	9.70E-07	2,082	Measured at Texas A&M University
Bentonite	0.782	2.44E-07	1,091	Remund and Lund, (1993), 0% sand
Bentonite	1.60	4.98E-07	1,091	Remund and Lund, (1993), 60% sand
Backfill	8.65	27.0E-07	1,091	Theoretical -- five times k_{soil}
Backfill	1,000	3120E-07	1,091	Theoretical -- optimum

transfer by about 5%. If a material with a thermal conductivity of five times (500%) the soil had been used, the heat transfer would have been 8% higher than the current backfill. Finally, the maximum possible heat transfer at a conductivity of 1,000 W/m-K raised the heat transfer above the soil value by 18%. Thus, the thermal conductivity of backfill could be increased to maximize the amount of heat dissipated to the soil. However, diminishing incremental increases in the heat transfer rate occurred for thermal conductivities above that of the surrounding soil.

The equivalent heat flux radius ($r_{h,eqv}$) was plotted in Figure 45. At the l/D_o of zero, k=8.65 and 1.000 W/m-K backfills yielded $r_{h,eqv}$ of 1.03 and 1.00, respectively. The lower conductivity backfills produced $r_{h,eqv}$ of 1.09 and 1.10 for k=1.6 and 0.782 W/m-K, respectively. Overall, $r_{h,eqv}$ increased with separation distance for lower backfill conductivities. If high conductivity backfills could be identified, there would not be any need for the expense of increasing the separation distance. For k=0.782 W/m-K, $r_{h,eqv}$ rose from 1.10 to 1.33. Therefore, $r_{h,eqv}$ varied with conductivity and separation by a maximum of 33%. In general, $r_{h,eqv}$ should be maximized to maximize heat transfer. However, maximizing $r_{h,eqv}$ was not a sufficient criteria to rank backfills because the overall heat dissipation to the soil decreased in Figure 44.

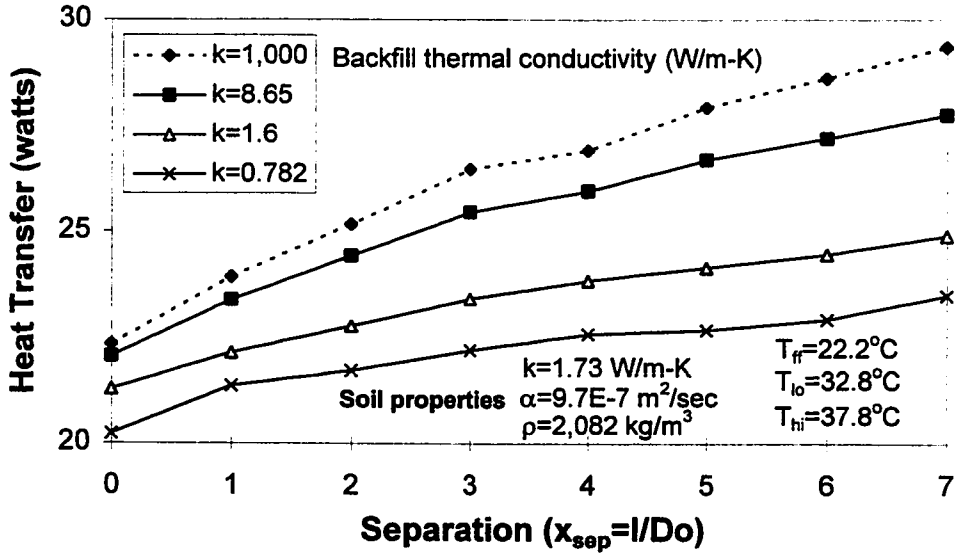

Figure 44. Net heat dissipated in the soil

The deviation of $r_{h,eqv}$ from Claesson's solution was also computed. The deviation was computed as the difference between $r_{h,eqv}$ and $\sqrt{2}$. The minimum deviation from $\sqrt{2}$ was 1.33 (k=0.782 W/m-K and l/D_o=7) which was 8%. On the other extreme the maximum deviation was 42% at $r_{h,eqv}$=1.0 (k=1,000 W/m-K and l/D_o=0). Therefore, the equivalent diameter varied widely with backfill conductivity and separation (at low conductivities).

The resulting thermal effectiveness shown in Figure 46 ranged from 55% up to 62% (at k=1.6 W/(m-°C)). As in previous cases the effectiveness increased with separation distance. However, effectiveness increased by a maximum of 33% with lower thermal conductivity. Again, the overall performance criteria was the net heat transfer. Therefore, while ε_Λ should be maximized, the lower conductivities resulted in less heat dissipation to the soil in Figure 44. Physically, increasing the conductivity in the backfill that contained the two sources enhanced heat transfer and thermal short circuiting. Therefore, ε_Λ decreased.

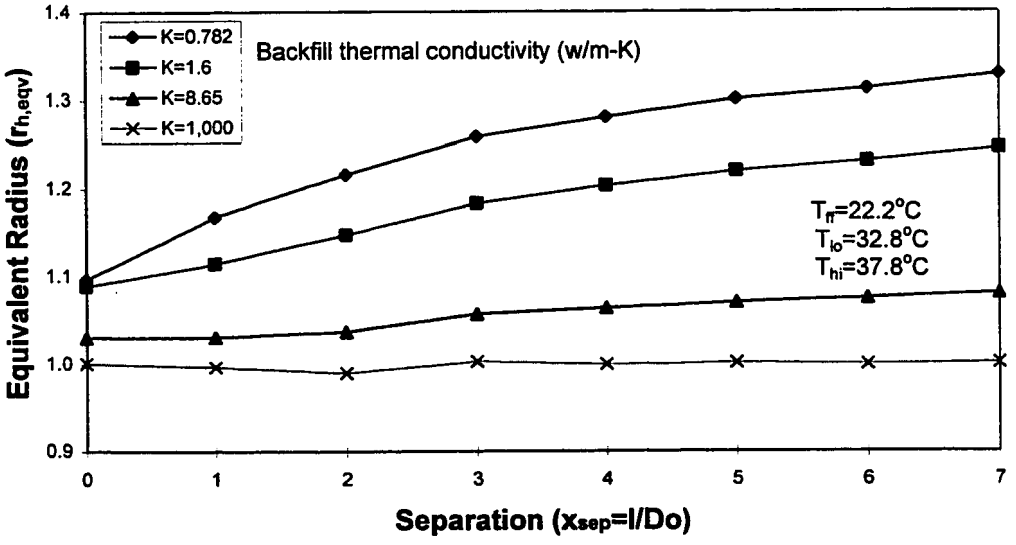

Figure 45. Heat flux equivalent radius $r_{h,eqv}$

Neither $r_{h,eqv}$ nor ε_Λ was sufficient for evaluating backfills because they decreased with higher thermal conductivities which increase heat transfer. Another method of ranking backfill materials was given by Couvillion and Cotton (1990) as:

$$\text{backfill effectiveness} = \varepsilon_{b'fil} = \frac{\sum |Q'/k|}{\sum |T_c - T_{ff}|}, \tag{68}$$

where in our case,

Q' = the net heat dissipated numerically (watts),

k = thermal conductivity of the backfill-3 cases (W/m-°C)

T_c = temperature imposed at the nodes (°C), and

T_{ff} = the temperature imposed at the farfield boundary.

While this definition yielded fractions between zero and one, the physical significance was not straight forward. Presumably, an effectiveness of one would correspond to heat flux crossing an area of one m^2 in a media of one meter of backfill.

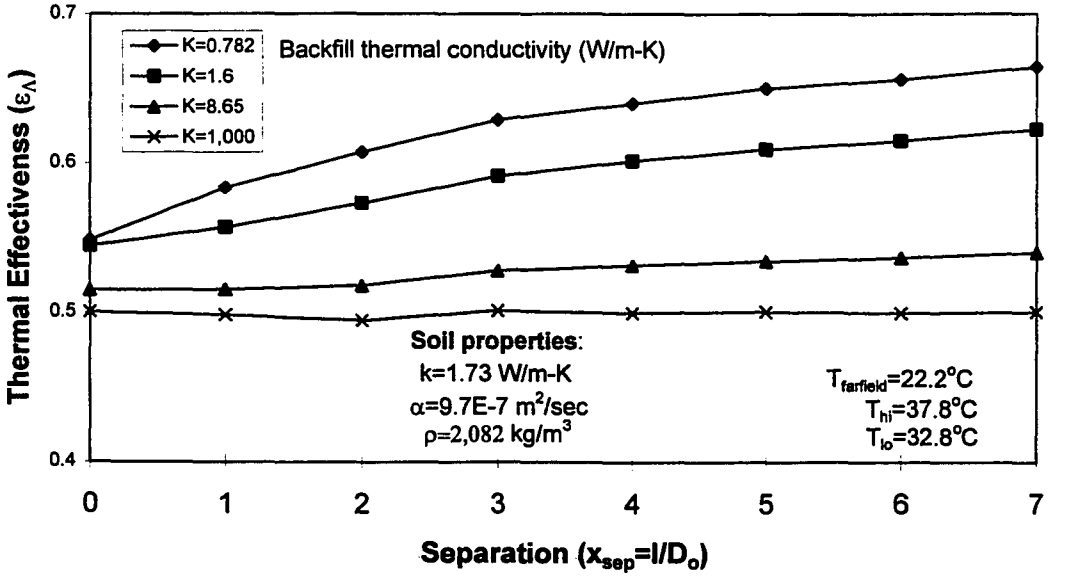

Figure 46. Thermal effectiveness

The numerical ranking of the four backfill conductivities was plotted in Figure 47. The backfill effectiveness $\varepsilon_{b'fil}$ ranged from 0.47 to 0.55 (at k=1.6W/m-K) as the separation distance increased. Backfill effectiveness increased by 25% as the thermal conductivity increased from k=0.782 to 1,000 W/m-K. The maximum possible $\varepsilon_{b'fil}$ was 0.648 at k=1,000 W/m-K and l/D_o=7. Therefore, $\varepsilon_{b'fil}$ increased with thermal conductivity which was consistent with more heat dissipation to the soil.

In conclusion, $\varepsilon_{b'fil}$ was a better method of ranking backfill than thermal effectiveness (ε_Λ) or heat flux equivalent radius ($r_{h,eqv}$) because of correlation with heat dissipation.

V.4 Case Study: Comparison with Mei Experiment

A case study was performed to incorporate backfill, equivalent diameter, and experimental data. The backfill model was compared with experimental data from Mei (1988). For comparison with Mei, the author's nine-source grid was modified as

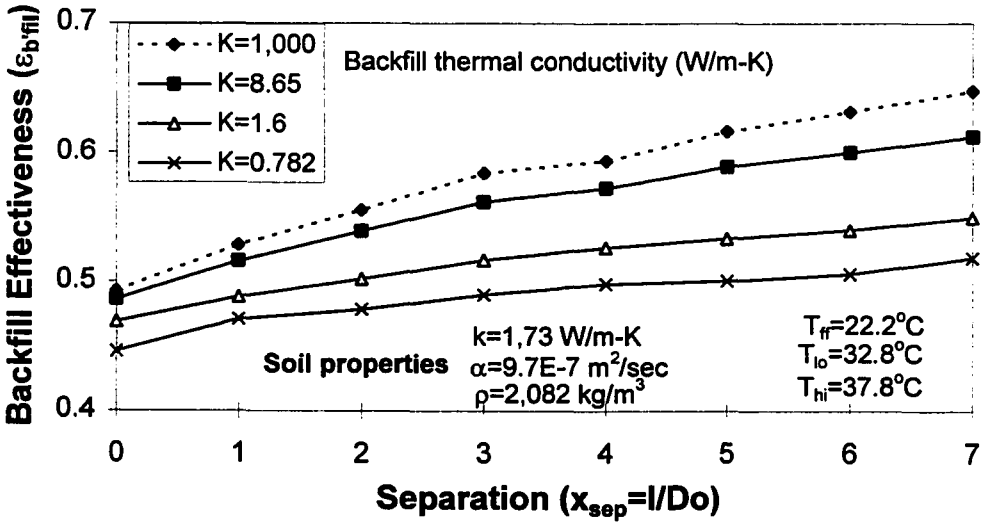

Figure 47. Backfill effectiveness

shown in Figure 48. The two pipes were separated by rubber insulation, and iron encases the bore hole. The six material properties are given in Table 5.

The FE calculated equivalent radius $r_{h,eqv}$ was plotted in Figure 49. Replacing the rubber insulation with 14 times higher conductivity cement in three elements (the other four elements reverted to polyethylene pipe) only increased the heat transfer monitored at $40r_o$ by 0.04%. This implied that the insulation had negligible effect on the overall heat transfer.

The equivalent radius (in Figure 49) after one hour was 1.18. The radius declined with time to reach a steady-state value of 1.04. Therefore, at all times, $r_{h,eqv}$ was lower than the Mei value of 1.3 which was monitored between 120-720 hours (5-30 days). However, one must note that Mei solved for $r_{h,eqv}$ by comparing his models calculated fluid exit temperatures with experimental fluid exit temperatures. In addition, Mei did not explain the verification of the single isolated source of $r_{h,eqv} = 1$. Finally, Mei's method examined the entire water loop, while the author's model only examines a cross-section with constant imposed temperatures. While

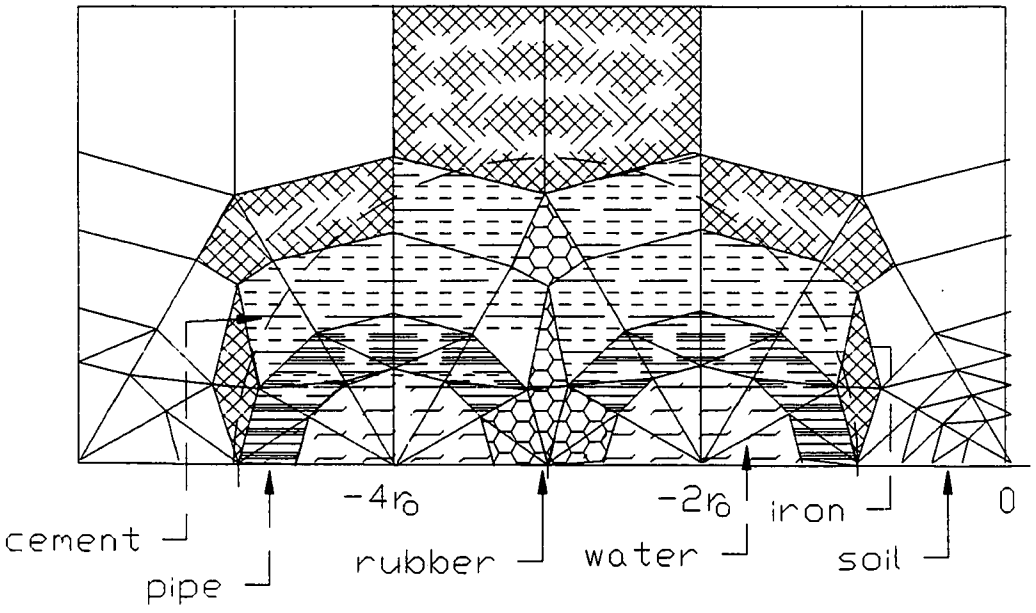

Figure 48. FE grid to simulate Mei's experiment

Table 5. Properties for simulating Mei's experiment

Material	k W/m-K	α m^2/sec	ρ kg/m^3	Source
Water	0.613	1.32E-07	997	Incropera, (1985), Table A.6
Polyethylene	0.046	2.25E-07	940	Mei (1988)
Soil	0.121	6.17E-07	1149	Mei (1988)
Concrete	0.433	6.3E-07	2240	Mei (1988)
Rubber	0.032	2.3E-07	70	Incropera, (1985), Table A.6
Iron	80.2	2.31E-7	7870	Incropera, (1985), Table A.6

it was advantageous to examine the entire loop, Mei's $r_{h,eqv}$ was a function of the varying soil properties of clay at shallow depth, a 60° slope limestone shelf, a water table at 9 m, and three wells bordering at a 30° slope decline. In conclusion, the two equivalent radii deviated by 8% to 19% partly because they were derived differently. Mei did not present a transient analysis.

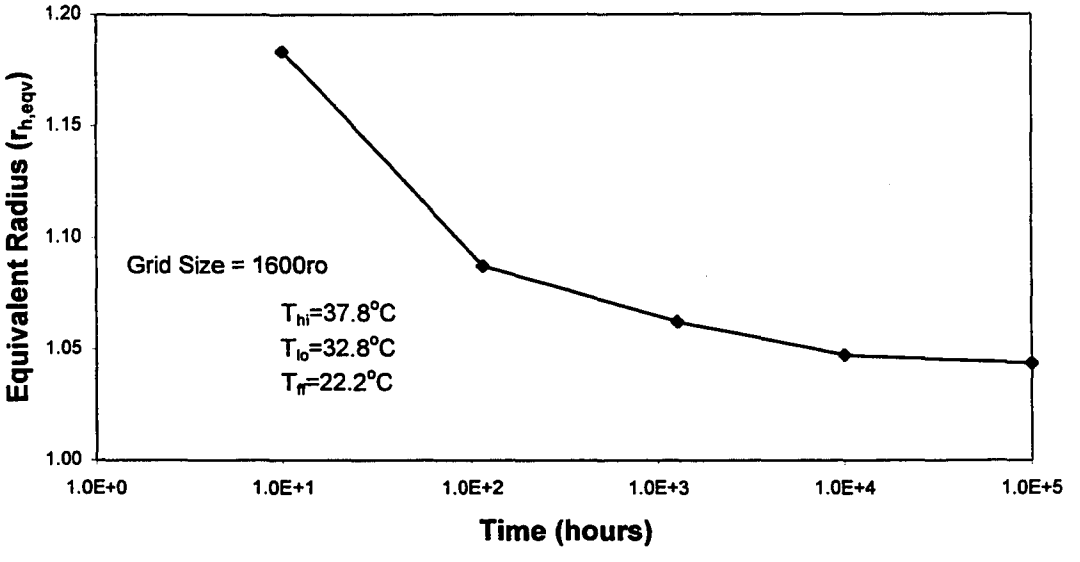

Figure 49. Transient equivalent radius simulating Mei's experiment. Equivalent values for insulated or un-insulated

V.5 Multi-pipe Installations

Some researchers have proposed installing more than two pipes in the same bore hole to minimize drilling costs. A potentially practical arrangement would be four pipes consisting of two supply pipes (higher temperature) and two return pipes (low). The two options are shown in Figure 50. The author's nine-source grid allowed

examination of up to nine pipes in the same hole using the flat spacing method of Figure 50. These four pipes were incorporated into the FE grid shown in Figure 51. The model allowed examination of hole size range of l/D_o=4 to 9 and hot versus cold pipes separation distance of l/D_o=0 to 5. The results for backfill conductivities of K=0.782, 1.6, and 8.65 W/m-°C are shown in Figure 52. For the bentonite backfill conductivity of 1.6, the ratio of four pipes heat transfer to two pipes ranged from 1.02 to 1.06 ($Q_{4\text{pipes}}/Q_{2\text{pipes}}$). This increase was very small, and even the use of very high conductivity backfills (k=8.65 W/m-°C) only increased the ratio to 1.12. Therefore, at steady-state, the author would only recommend more than two pipes with high conductivity backfills. For a given hole size, the four pipes allowed more convective surface area, but also a shorter separation by two diameters. Therefore, short circuiting negated the effect of more surface area.

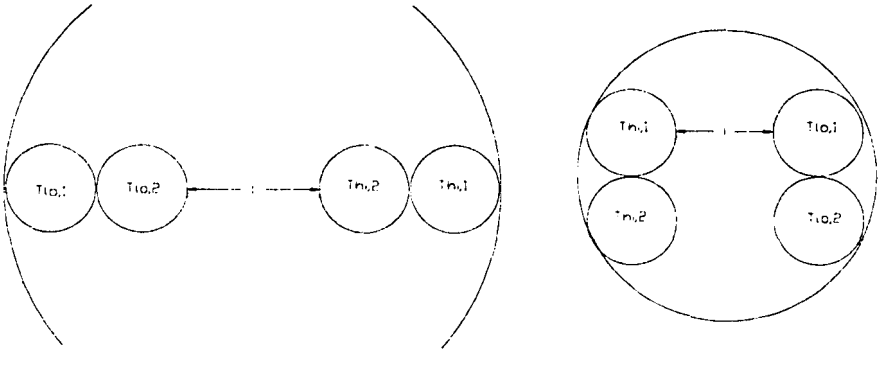

Figure 50. Flat and bundle multi-pipe arrangements

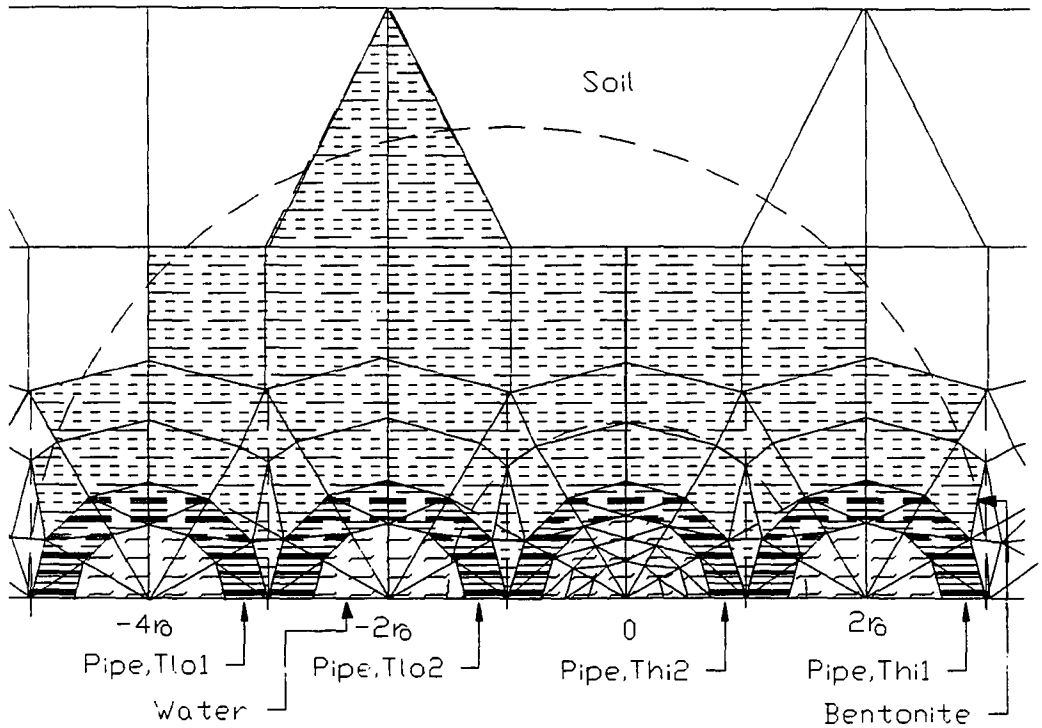

Figure 51. Typical four pipe FE grid. The hole size is l/D_o=4 and the hot vs cold pipe separation distance is l/D_o=0.

V.6 Summary

This chapter first examined equivalent diameters by simulating different diameter sources in a two-source grid. For constant temperature sources, two, $1r_o$ sources yielded the same heat flux as one, $2r_o$ source. For constant heat flux sources, the resulting temperatures in the soil farfield depended only on the heat flux imposed and was independent of number or size of sources. Next, a nine-source grid was developed to determine the effect of variable separation distances on equivalent diameters and short circuiting. For two similar temperature sources, the thermal effectiveness ranged from 52% at an l/D_o of 0 to 62% at an l/D_o of 7.

The equivalent radius was solved from an equation for equivalent heat (Q_{eqv}). The geometric equivalent radius $r_{g,eqv}$ ranged from $1.37r_o$ for touching sources to

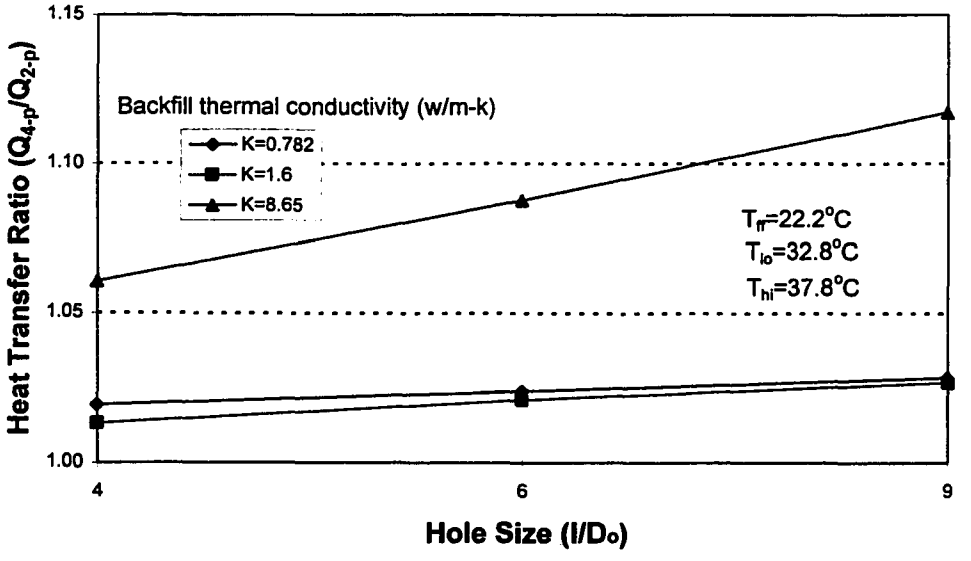

Figure 52. Steady-state heat transfer ratio of four pipes vs two pipes

$4.07r_o$ at an l/D_o of 7. The geometric equivalent radius for touching sources (at constant temperature and thousands of operation hours), $1.37r_o$, was comparable to the analytical solution of $1.414r_o$ by Claesson and Dunard, and the experimental value of $1.3r_o$ by (Mei, 1988). The geometric equivalent diameter was abandoned because it was a function of grid size and approached large numbers as short circuiting decreased. A heat flux equivalent radius $r_{h,eqv}$ was defined as the equivalent number of sources, and more logically ranged from one to two.

Next, the case of two different constant temperature sources was examined. The thermal effectiveness decreased with time until convergence. The steady-state effectiveness ranged from 55% for touching sources to 64% at an l/D_o of seven. Unfortunately, the high temperature equivalent geometric radius $r_{hi,g,eqv}$ was a strong function of operation hours. The range of $r_{hi,g,eqv}$ was from zero for touching sources to four at an l/D_o of seven. The heat flux equivalent radius $r_{h,eqv}$ was found to be close to the values of constant temperatures for $l/D_o \geq 4$.

The effect of temperature variation on thermal effectiveness was investigated. There was no significant change in ε_Λ from varying the farfield temperature, or the temperature deviation between two coils. And most importantly, the thermal effectiveness was produced numerically in Table 3 as a function of separation distance.

Finally, the numerical consistency of the homogenous model was determined to be 3% deviation from energy conservation in the first 100 radii.

Thermal conductivity of backfill needs to be improved. The Texas A&M University bentonite backfill possessed lower thermal conductivity than the native soil. In ranking backfills, the $r_{h,eqv}$ and ε_Λ must be compared with the overall performance criteria of net heat dissipated to the ground. A better ranking of backfill performance was $\varepsilon_{b'fil}$ because of consistency with the overall heat exchanger performance.

A case study was performed to compare the FE model with the experiments of Mei (1988). The author's $r_{h,eqv}$ was 7-18% lower, and reasons for the discrepancy were noted.

V.7 Conclusion on Equivalent Diameter

Many formulations of equivalent diameter have been proposed that are internally consistent with their heat transfer model. The types of r_{eqv} examined in this chapter were Mei's convective experimental set up, Claeson's dipole solution, the author's models for analytical constant temperature and constant heat source, and the author's numerical FE models for constant heat or constant temperature (geometric and heat flux radius). The author concluded that the most universal and meaningful equivalent diameter was $r_{h,eqv} = Q_{eqv}/[(Q_1 + Q_2)/2]$. This allowed direct expression of the equivalent radius as the equivalent heat flux (e.g. $r_{h,eqv} = 1.414$ implies that the Q_{eqv} was 41.4% greater than the average single coil heat flux).

V.8 Further Work

Some further studies are required. Most importantly, an overall performance variable or model must be defined and used to evaluate thermal effectiveness, backfill effectiveness, and equivalent diameter. Other criteria that could affect performance are magnitude of variable heat pump load, proper backfilling technique, and moisture migration.

CHAPTER VI

FINITE ELEMENT HEAT AND MASS TRANSFER EQUATIONS

This chapter expanded the previously developed heat transfer model to include moisture transport. The moisture transport model was based on the theory of Phillip and de Vries (1957) and the numerical adaptation by Hampton (1989). The work of Phillip and de Vries (1957) and Hampton (1989) were reviewed in Chapter II: *Literature Survey.* This chapter was organized into four sections: (1) Phillip and de Vries theory, (2) Hampton's numerical model, (3) heat transfer equation, and (4) moisture migration.

VI.1 Phillip and de Vries Model

Phillip and de Vries developed the fundamental equations for coupled heat and water transport in incompressible saturated media. This study used their theory of soil physics laws to explain the known primary mechanisms responsible for heat and moisture transport in the soil. Eight assumptions were used in deriving the model:

1. The liquid in the porous media had the properties of pure bulk water. This implied the absence of solutes or surfactants.
2. Liquid moved by viscous flow under the influence of capillary and adsorptive forces.
3. Vapor moved by diffusion in the gas-filled pores, which contained vapor and air as an inert gas.
4. Free convection in the gas phase was neglected.
5. The total pressure was constant and uniform.
6. Local thermodynamic equilibrium prevailed throughout the porous medium. In particular, this applied to the liquid in contact with vapor.
7. Radiation heat transfer was negligible.

8. The temperature dependence of ρ_l, C, H and L was neglected.

The physical limitations resulting from these assumptions were explained by de Vries (1987) as:

1. Hysteresis was not accounted for in the relation between the moisture potential and the moisture content.
2. The theory only applied to a rigid matrix.
3. The medium was porous, homogeneous, and isotropic in a macroscopic sense.
4. The phenomena of boiling, freezing and thawing were not included.
5. The model did not account for surface phenomena at the interface between the matrix and the liquid, nor the Knudsen effects in the gas phase.

VI.2 Hampton: FE with Moisture

Hampton (1989) continued the work of Walker (1981) in adding the Phillip and de Vries moisture theory to the problem of storing heat in soil supplied by a cylindrical heat source. Hampton improved the liquid-vapor interactions model of Phillip and de Vries, and then produced computational formulations. Additional advantages included applicability to inhomogeneous soils, explicit consideration of the temperature dependence of matric suction head, and the inclusion of the effects of temperature and pressure on water storage.

In this chapter, the coupled partial differential equations for heat transfer and moisture flow were derived separately. First, the energy transport equation was formulated because it was an extension of the earlier heat transfer equation derived in Chapter III. Then the water transport equation was developed.

VI.3 Heat Transfer Equation

The fundamental equations of heat transfer were derived from conservation of energy

$$\dot{E}_{in} + \dot{E}_{generated} - \dot{E}_{out} = \dot{E}_{stored}$$
$$\text{or } -\Delta Q = \frac{\partial U}{\partial t}. \tag{69}$$

First, the energy storage gradient was derived. Then the heat flux components were derived. Finally the heat flux gradient was imposed and the two formula combined.

VI.3.1 Internal Energy

The increase in internal energy stored in the soil (s), water (w), and vapor (v) in units of J/(sec-m^3) was

$$\frac{\partial U_{total}}{\partial t} = \frac{\partial U_s}{\partial t} + \frac{\partial U_w}{\partial t} + \frac{\partial U_v}{\partial t}$$
$$\approx \frac{\partial}{\partial t}[\rho_s c_{vs}(T - T_o)(1 - \phi)] + \frac{\partial}{\partial t}[\theta_w \rho_w c_{vw}(T - T_o)],$$

where ϕ was the porosity. The thermal energy of the gas was assumed negligible because the relative mass of the gas phase was miniscule and therefore its increase $\frac{\partial U_v}{\partial t}$ was small and could be disregarded ($\frac{\partial U_v}{\partial t} \approx 0$). The derivative was computed using the notation of $C_{s+w} = \rho_s c_{vs}(1 - \phi) + \rho_w c_{vw}\theta_w$,

$$\frac{\partial U_{total}}{\partial t} = \frac{\partial}{\partial t}[C_{s+w}(T - T_o)]$$
$$= C_{s+w}\frac{dT}{dt} + (T - T_o)\frac{dC_{s+w}}{dt}. \tag{70}$$

De Vries (1963) reduced experimental data to mathematical expressions for the heat capacity C_{s+w}. The value of c_{vw} was 4190 J/kg with a maximum error of 1% in the range of 0 to 100°C. In addition, the solid phase was divided into mineral (m) and organic (o) fractions. The de Vries equation for heat capacity in consistent mks units of J/kg-°C was

$$C_{s+w} = (1890 + 4.29T_c)\theta_m + 2510\theta_o + 4.19\rho_w\theta_w. \tag{71}$$

Therefore, the derivative for combined specific heat was,

$$\frac{dC_{s+w}}{dt} = 4.29\theta_m\frac{dT}{dt}. \tag{72}$$

Equations 71 and 72 were incorporated into the overall heat capacity term of equation 70 to give

$$\frac{\partial U_{total}}{\partial t} = [1890 + 4.29(2T_c - T_o)]\theta_m + 2510\theta_o + 4.19\rho_o\theta_w\frac{dT}{dt},$$

which can be written as

$$\frac{\partial U_{total}}{\partial t} = C_{pg}\frac{dT}{dt} \tag{73}$$

where

C_{pg} = generalized specific heat which can change with moisture content ($J/m^3-°C$),

T_c = temperature (° C),

T_o = reference temperature (27 °C),

θ_o = volumetric fraction of organic matter, and

ρ_o = density at the reference temperature (kg/m^3).

This expression's value for specific heat depended on the relative amounts of water and solid (volumetric water content), but not the type of soil. Therefore, the equation may have to be modified to reflect different types of soils and non-homogenous materials such as pipes and backfill. In addition, the equation was approximated with constant coefficients of $\theta_o = 0.6$ and $\theta_m = 0.46$ (for soils in general). De Vries (1963) determined these values at 10°C. They varied by 13% between 0 and 60°C for his data.

VI.3.2 Total Energy Transport

Thermal energy ($\dot{E}_{in} - \dot{E}_{out}$) entered each element in four ways: (1) conduction through the soils, (2) latent heat of vaporization, (3) advection of water at a temperature other than T_o, and (4) heat generation:

$$Q = Q_{conduction} + Q_{latent} + Q_{advection} + Q_{generated} \tag{74}$$

VI.3.2.1 Heat Conduction

De Vries (1958, Eq. 18) derived a comprehensive energy balance for soils. However, the contributions of water vapor and the heat of wetting to internal energy

were omitted because they were negligible in most applications (Hampton, 1989). Additionally, de Vries replaced λ with $\lambda_{bone-dry} + L\rho_w D_T$. Therefore, the soil conduction was separated from the latent heat transport:

$$Q_{conduction} = -(\lambda - L\rho_w D_T)\nabla T. \tag{75}$$

The apparent (and measured) thermal conductivity, λ, accounted for conduction and thermally-induced vapor flow (distillation). Therefore, λ was a function of water content and temperature. The numerical code must be provided with apparent thermal conductivity values throughout the possible range of water content and temperature.

VI.3.2.2 Latent Heat Transport

The latent heat transported was a product of the heat of evaporation and the rate of evaporation:

$$Q_{evap} = L\rho_v q_v, \tag{76}$$

where, q_v was the Darcian water vapor flux (m/sec).
However, the FE formulation required a relationship with suction pressure (Ψ). The evaporation rate was given by the mass continuity equation for water vapor transport:

$$E = \nabla \cdot \rho_v q_v + \frac{D\theta_a \rho_v}{Dt} + \theta_a \rho_v \nabla \cdot v_s. \tag{77}$$

It was assumed that $\theta_a \rho_v$, $E \approx \nabla \cdot \rho_v q_v$, where E = evaporation, ρ_v = density of vapor, and q_v= volumetric water vapor flux.

The first term in equation 77 was simplified by Phillip and de Vries (1957) as

$$\rho_v q_v = -\rho_w D_{Tv} \nabla T - \rho_w K_{\Psi v} \nabla \Psi. \tag{78}$$

Both terms were small and often neglected. The temperature gradient term was omitted under the assumption that it was dwarfed by the thermal conductivity. However, the matric suction gradient term was retained to give moisture coupling through suction pressure to the heat equation. Therefore, the model used the

approximation $\rho_v q_v \approx -\rho_w K_{\Psi v} \nabla \Psi$, where the isothermal vapor conductivity was given by

$$K_{\Psi v} = \frac{D_{atm} \nu \theta_a \alpha \rho_v g}{\rho_w R_v T}. \tag{79}$$

The resulting heat transferred by evaporation was the product of the latent heat and the evaporation rate

$$Q_{evap} = L \rho_v q_v \approx -L \rho_w K_{\Psi v} \nabla \Psi. \tag{80}$$

VI.3.2.3 Heat Advection

The advective heat transport was the energy resulting from water transported due to bulk fluid motion at a temperature other than T_o:

$$Q_{advection} = c_{vw}(T - T_o)\rho_w q_m, \tag{81}$$

VI.3.2.4 Heat Generation

The possible sources of heat generation were given by

$$\dot{E}_{generated} = S_h + c_{vw} S_L (T_L - T_o), \tag{82}$$

where,

S_h = heat sources - positive when heat was released (J/m^2-sec),

S_L = source of liquid water (kg/m^3-sec), and

T_L = temperature of the liquid source (°K).

Finally, the total energy transport equation was reduced to its elementary form. The heat flux equation (74) with substitution of the three mechanisms for heat conduction (75), latent heat (80), heat advection (81), and heat generation (82) was given by de Vries, (1958, Eq. 18) as:

$$Q = -(\lambda - L\rho_w D_T)\nabla T + L\nabla \cdot (\rho_w K_{\Psi v} \nabla \Psi) + c_{vw}(T - T_o) + S_h$$
$$+ c_{vw} S_L (T_L - T). \tag{83}$$

The only remaining addition was for imposed heat flux such as $Q = -h(T_\infty - T)$. Therefore, the gradient of the heat flux was

$$-\nabla Q = -\nabla Q_h - \nabla \cdot [-\lambda \nabla T - L\rho_w k_{\Psi v} \nabla \Psi + c_{vw}(T - T_o)\rho_w q_w] + S_h + c_{vw} S_L (T_L - T_o). \quad (84)$$

VI.3.3 Energy Balance Equation

Therefore, the total heat balance of equation 69 with terms substituted from equations 73 and 84 become

$$C_{pg} \frac{\partial T}{\partial t} = -\nabla Q_h + \nabla \cdot \lambda \nabla T + L \nabla \cdot \rho_w K_{\Psi v} \nabla \Psi - c_{vw} \rho_w q_w \cdot \nabla T + S_h + c_{vw} S_L (T_L - T). \quad (85)$$

where,

λ = apparent (or measured) thermal conductivity (J/m-sec-° C),

S_h = heat flux (J/m^2-sec),

L = latent heat, or heat of vaporization, of water (J/gm),

T_o = initial temperature (°C),

D_T = thermal vapor diffusivity (m^2/sec), and

ρ_o = density of water at T_o (kg/m^3).

This was the final equation for coupled heat and mass transfer. Next, the equation was formulated into finite elements and coded. The temperatures were in $°C$.

VI.3.4 FE formulation of Heat Equation

The right hand side of equation 85 was converted to finite element formulation with first order derivative approximations:

$$\int_s \psi_{si} Q_h dS - \int_V \left\{ C_{pg} \psi_i \psi_j \dot{T}_j + \left[\lambda \frac{\partial \psi_i}{\partial x} \frac{\partial \psi_j}{\partial x} T_j + \lambda \frac{\partial \psi_i}{\partial y} \frac{\partial \psi_j}{\partial y} T_j \right] + \left[L \frac{\partial \psi_i}{\partial x} \frac{\partial \psi_j}{\partial x} \rho_w K_{\Psi v} \Psi_j + L \frac{\partial \psi_i}{\partial y} \frac{\partial \psi_j}{\partial y} \rho_w K_{\Psi v} \Psi_j \right] + c_{vw} \rho_w q_{wx} \psi_i \frac{\partial \psi_j}{\partial x} T_j + c_{vw} \rho_w q_{wy} \psi_i \frac{\partial \psi_j}{\partial y} T_j - \psi_i S_h - c_{vw} S_L \psi_i (T_L - \psi_j T_j) \right\} dV = \bar{0}. \quad (86)$$

One final boundary condition change was needed for convective terms in the volume integral:

$$\left[c_{vw}\rho_w q_{wx}\psi_i\frac{\partial\psi_j}{\partial x}T_j + c_{vw}\rho_w q_{wy}\psi_i\frac{\partial\psi_j}{\partial y}T_j\right] \Longrightarrow Q_{conv} = H\left(T_\infty - \psi_{sj}T_{sj}\right)$$
$$= \int_s \psi_{si}HT_\infty ds + \int_s \psi_{si}H\psi_{sj}ds. \tag{87}$$

This change was made because the two terms were not symmetric and could not be stored or solved using banded matrix principles. Without the change, storage requirements would have doubled and execution time quadrupled. In addition, the sensible heat transfer due to fluid flow (in the unsymmetric term) was usually negligible in relatively dry soils.

However, some portions of the control surface were subjected to a *convective* heat loss or gain that was different from the previous sensible heat transport by liquid convection. Therefore, the final symmetric global finite element equation including both distributed heat flux and *convective* heat loss or gain was

$$\int_s \psi_{si}Q_h dS - \int_V \left\{C_{pg}\psi_i\psi_j\dot{T}_j + \left[\lambda\frac{\partial\psi_i}{\partial x}\frac{\partial\psi_j}{\partial x}T_j + \lambda\frac{\partial\psi_i}{\partial y}\frac{\partial\psi_j}{\partial y}T_j\right]\right.$$
$$+\left[L\frac{\partial\psi_i}{\partial x}\frac{\partial\psi_j}{\partial x}\rho_w K_{\Psi v}\Psi_j + L\frac{\partial\psi_i}{\partial y}\frac{\partial\psi_j}{\partial y}\rho_w K_{\Psi v}\Psi_j\right]$$
$$\left.-\psi_i S_h - c_{vw}S_L\psi_i(T_L - \psi_j T_j)\right\}dV + \int_s \psi_{si}HT_\infty ds + \int_s \psi_{si}H\psi_{sj}ds = \bar{0}. \tag{88}$$

VI.3.5 FE Coding of Energy Equation

The temperature dependence of ρ_w was accounted for in the $\partial(\rho_w\theta_w)/\partial t$ term of equation 71, and T was the temperature in $^\circ C$. The S_L term vanished whenever the temperature of the liquid source was not the same as that of the volume element. The symmetric finite element formulation later discarded the unsymmetric convection (i. e. , $q_w \cdot \nabla T$). Additionally, the source terms remained available but were not utilized. The code began by initializing θ_w and Ψ, and setting $S_h, S_l = 0$.

VI.3.6 Heat - Temperature, FE -T Equation

The combined heat flux in porous medium due to conduction, distillation and sensible heat convection was given by equation 85. Therefore, the finite element matrix for energy transport was

$$[C_{pg}]\{\dot{T}\} + \Big([K_{T\lambda}] + [K_{bct}]\Big)\{T\} = -[F_L]\{\Psi\} + \{F_{Qh}\} \tag{89}$$

where,

$$[C_{pg}] = \int_V \psi_i \rho c_{pg} \psi_j dV,$$
$$[K_{T\lambda}] = \int_v \left[\frac{\partial \psi_i}{\partial x}\lambda\frac{\partial \psi_j}{\partial x} + \frac{\partial \psi_i}{\partial y}\lambda\frac{\partial \psi_j}{\partial y}\right] dV,$$
$$[K_{bct}] = \int_v \psi_{si} H \psi_{sj} dS + c_{vw}\int_v S_L \psi_i \psi_j dV,$$
$$[F_L] = L\int_v \rho_w K_{\Psi v}\left[\frac{\partial \psi_i}{\partial x}\frac{\partial \psi_j}{\partial x} + \frac{\partial \psi_i}{\partial y}\frac{\partial \psi_j}{\partial y}\right] dV, \text{ and}$$
$$[F_{Qh}] = \int_s \psi_{si} Q_h dS + \int_s \psi_{si} H T_\infty dS + \int_v \psi_i S_h dV + c_{vw}\int_s \psi_i S_L T_L dV.$$

The $[C_{pg}]$ matrix contained the capacitance which usually needs to be *lumped* for numerical stability. The stiffness matrices were $[K_{T\lambda}]$ for conduction (λ) and $[F_L]$ for latent heat (L). Each of the terms in $[K_{bcT}]$ complemented a term in $[F_{Qh}]$; $[K_{bcT}]$ was the variable temperature portion while $[F_{Qh}]$ was the constant. The first term in $[K_{bcT}]$ was part of the convection boundary condition, while the second term was half of the the terms for injecting water at a temperature different from the media. $[F_{QH}]$ contains four constant loads. The first was the boundary heat flux (except convection) while the second term was for convective heat flux. The third term was for a heat source, and the final term was for injecting water at a different temperature. The S_l and S_h refer to point and distributed source/sinks.

The expanded problem with the addition of boundary conditions becomes

$$\int_{\Omega} \rho_e C_{p,e} \phi_i(x,y) \phi_j(x,y) \frac{dT(t)}{dt} d\Omega$$
$$+ \int_{\Omega} \left\{ k \frac{\partial \phi_i(x,y)}{\partial x} \frac{\partial \phi_j(x,y)}{\partial x} + k \frac{\partial \phi_i(x,y)}{\partial y} \frac{\partial \phi_j(x,y)}{\partial y} \right\} T(t) d\Omega$$
$$+ \int_{\Omega} \left\{ L \frac{\partial \phi_i(x,y)}{\partial x} \frac{\partial \phi_j(x,y)}{\partial x} \rho_w K_{\Psi v} + L \frac{\partial \phi_i(x,y)}{\partial y} \frac{\partial \phi_j(x,y)}{\partial y} \rho_w K_{\Psi v} \right\} \Psi_j d\Omega$$
$$= \int_{\partial\Omega_2} \left\{ k \frac{\partial \phi_i(x,y)}{\partial x} n_x + k \frac{\partial \phi_j(x,y)}{\partial y} n_y \right\} T(t) d\Omega + \int_{\Omega} \{ \dot{q} \phi_i(x,y) \phi_j(x,y) \} T(t) d\Omega$$
$$+ \int_{\Omega} f(x,y,t) \phi_i(x,y) d\Omega. \qquad (90)$$

There are several ways to solve this system of linearized (first order) differential equations. Here, the time derivatives, $\dot{T}$, were replaced by a numerical approximation, and the nonlinear differential equations were reduced to nonlinear algebraic equations. These equations were then linearized and solved iteratively.

The time derivative can be approximated numerically using finite differences or finite elements. The finite element method was used above to replace the spatial derivatives because of its ability to handle complex boundary shapes and different coordinate systems. In the time dimension, these attributes of the finite element method were not necessary. Thus finite difference methods are customarily used to approximate time derivatives.

The most general way to apply transient finite differences to equation 89 was to replace derivatives such as $\dot{T}$ by

$$\{\dot{T}\} = \frac{1}{\Delta t} \{ \{T\}_{t+\Delta t} - \{T\}_t \}, \qquad (91)$$

and to replace state variables such as T by

$$\{T\} = \{ (1-\theta)\{T\}_t + \theta \{T\}_{t+\Delta t} \}. \qquad (92)$$

Here, the time dimension was discretized into steps of duration Δt. At time, t, the state variables (T and Ψ) were known. The values of the state variables at time $T + \Delta t$ were unknown. Using the parameter θ, $\{T\}$ in equation 89 was replaced by

the values of T at time level $t + \Delta t$. If $\theta = 0$, the approximation was called explicit, while $\theta = 1$ was fully implicit, and $\theta = 1/2$ was the Crank-Nicolson method that was used below.

Substituting equations 91 and 92 into 89, the resulting matrix algebraic equation for code QM was

$$[Cp] * \frac{1}{\Delta t}\Big(\{T\}_{t+\Delta t} - \{T\}_t\Big)$$
$$+ ([K_T] + [K_{bcT}]) * ((1-\theta)\{T\}_t + \theta\{T\}_{t+\Delta t}) = [F_L]\{\Psi\} + \{F_{Qh}\}. \qquad (93)$$

The matrices were strategically re-arranged as

$$\left[\frac{[Cp]}{\Delta t} + \theta([K_{T\lambda}] + [K_{bct}])\right]\{T\}_{t+\Delta t}$$
$$= \left[\frac{[Cp]}{\Delta t} - \Big(1-\theta\Big)\Big([K_{T\lambda}] + [K_{bcT}]\Big)\right]\{T\}_t - [F_L]\{\Psi\} + \{F_{Qh}\} \qquad (94)$$
$$\text{or } [Gk] * \{T_{t+\Delta t}\} = [GF].$$

The unknown in this equation was $T_{t+\Delta t}$. Note that T_t and Ψ were considered known. Therefore, the solution to the energy equation was

$$\{T_{t+\Delta t}\}_{t+\Delta t} = [Gk]^{-1}[GF].$$

Iterations were accomplished using the model until convergence between solving equation 94 for energy and the equation for water transport developed.

VI.4 Water Transport

The equation to solve for water content in incompresible media was developed by Phillip and de Vries (1957). However, Hampton (1989) proposed that in unsaturated media it was more useful to solve this equation for suction pressure which can be related to temperature gradient. Therefore, Hampton (pg 113) performed a variable

change and added a term to relate the gradient of water content and suction pressure to the gradient of suction pressure and temperature to yield

$$\left[\left(\frac{\partial\theta_w}{\partial\Psi}\right)_{T,\sigma'}+\frac{\theta_w S_s}{\Phi}\right]\frac{\partial\Psi}{\partial t}-\left[\theta_w\beta_T+\left(\frac{\partial\theta_w}{\partial\Psi}\right)_{T,\sigma'}\left(\frac{\partial\Psi}{\partial T}\right)_{\theta_w,\Phi}\right]\frac{\partial T}{\partial t}=$$
$$\nabla\cdot(\bar{K}_w\cdot\nabla\Psi)+\frac{\partial K_{wz}}{\partial z}+\nabla\cdot(K_{\Psi_v}\nabla\Psi+D_T\nabla T)+\frac{S_L}{\rho_w} \qquad (95)$$

The control volume for water flow was constructed in Figure 53. Because the mass flow equation was coupled to the heat transfer equation, the suction pressure (Ψ) and temperature (T) were known (or estimated) as a function of x. The y-direction terms were similarly defined, and there was only one term in the z-direction. The terms on the left hand side (LHS) of equation 95 represented the rate of increase of water stored in the control volume due to various temporal changes. The first term was usually the largest term and represented the change in water content in an isothermal rigid medium when water was assumed incompressible. The second term was identified by Neuman (1973) and stated that as Ψ increased, the compressibility of the fluid and soil skeleton (soil structure without moisture) allowed more water storage in a given volume. The third and usually minor term implied that thermal expansion of the fluid caused less mass to be stored in a given volume. The last term was significant for most non-isothermal flow problems in unsaturated media. Hampton (1989) proposed this term to consistently consider suction pressure as a function of water content and temperature. Figure 54 shows how less water is stored in a given volume when heated because matric suction head, Ψ, increases ($|\Psi|$ decreases) with temperature.

Each of the first three terms on the right side was the negative divergence of a flux. Each term represented the net rate of flow into the volume element resulting from some process. The first term showed the the flow of liquid water induced by matric suction head gradients. The second term accounted for gravitationally induced drainage. Whenever K_{wz} increased in the positive upward (z) direction, this term was positive. The third term was for water vapor flow and the last term was for a source of liquid water.

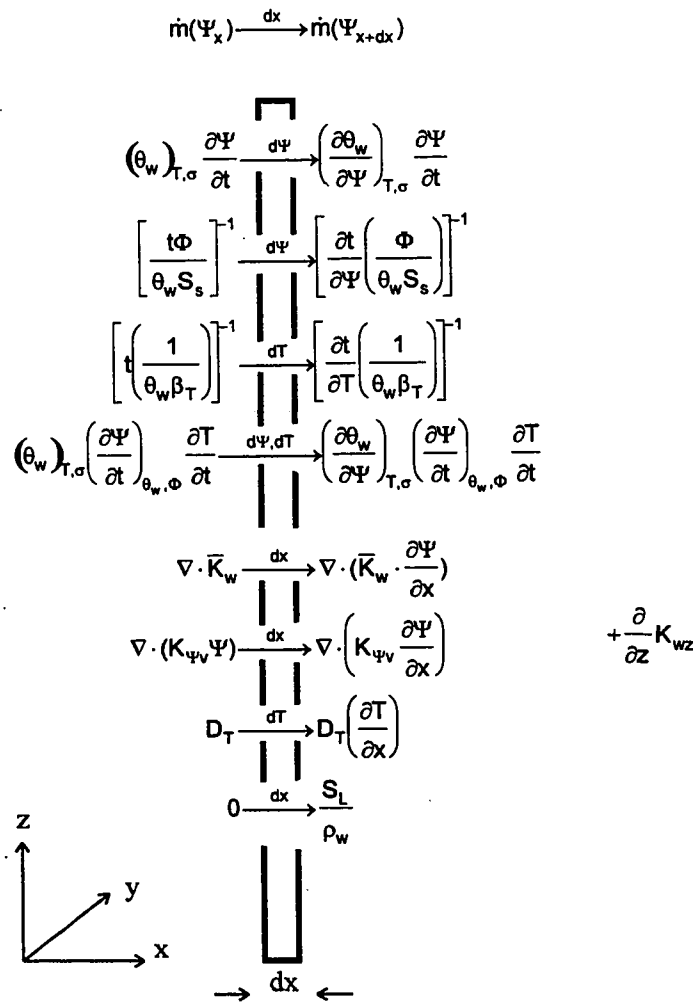

Figure 53. Control volume for water flow in x-direction. The y-direction was similar and there was only one z-direction term.

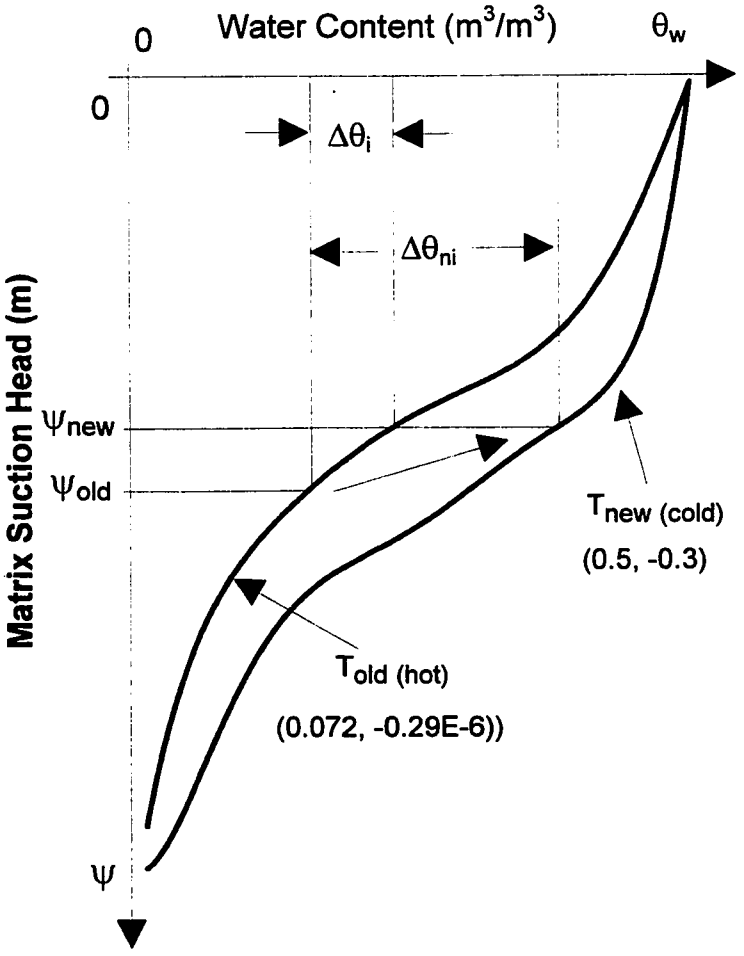

Figure 54. Comparison of water content changes when suction pressure increased. Pressure went from Ψ_{old} to Ψ_{new} isothermally ($\delta\theta_i$) and non-isothermally ($\delta\theta_{ni}$, where $T_{new} < T_{old}$. Suction was negative for unsaturated porous media.

The equation limitations included: (1) no solutes, (2) constant gas phase pressure, (3) approximate soil deformation (second term on LHS), and (4) no moisture hysteresis changing from drying to wetting soil (unlike Figure 54).

The water balance equation can be applied to nonhomogenous soils (unlike the Phillip and deVries theory), and included explicit consideration of the temperature

dependence of matric suction head, and the effects of temperature and pressure on water storage.

VI.4.1 FE water transport- Ψ equation

The derivation of a finite element moisture equation for Ψ was similar to that of the heat T equation. In fact, the same computation matrices were used to sequentially solve for both variables. The finite element matrix equation for water transport when converted into cartesian coordinates yielded:

$$\begin{aligned}
&\int_V \psi_i F \psi_j \dot{\Psi} dV \\
&+ \left\{ \int_v \left[\frac{\partial \psi_i}{\partial x} K_{\Psi x} \frac{\partial \psi_j}{\partial x} + \frac{\partial \psi_i}{\partial y} K_{\Psi y} \frac{\partial \psi_j}{\partial y} \right] \Psi_j dV \right. \\
&\left. + \int_v \left[\frac{\partial \psi_i}{\partial x} D_T \frac{\partial \psi_j}{\partial x} + \frac{\partial \psi_i}{\partial y} D_T \frac{\partial \psi_j}{\partial y} \right] T_j dV \right\} \\
&= \int_s \psi_{si} Q_B dS + \int_v \psi_i \frac{S_L}{\rho_w} dV - \int_v \psi_i G \psi_j \dot{T}_j dV + \int_v \frac{\partial \psi_i}{\partial z} K_{wz} dV = \bar{0}. \qquad (96)
\end{aligned}$$

This equation was written in a more compact form as:

$$\begin{aligned}
[F]\{\dot{\Psi}\} + [HK]\{\Psi\} &= \{QW\} - [TK]\{T\} - [Go]\{\dot{T}\} \\
\text{where}[F] &= \int_V \psi_i F \psi_j dV \\
[Go] &= \int_v \psi_i G \psi_j dV \\
[HK] &= \int_v \left[\frac{\partial \psi_i}{\partial x} K_{\Psi x} \frac{\partial \psi_j}{\partial x} + \frac{\partial \psi_i}{\partial y} K_{\Psi y} \frac{\partial \psi_j}{\partial y} \right] dV \\
\{QW\} &= \int_s \psi_{si} Q_B dS + \int_v \psi_i \frac{S_L}{\rho_w} dV + \int_v \frac{\partial \psi_i}{\partial z} K_{wz} dV \\
[TK] &= \int_v \left[\frac{\partial \psi_i}{\partial x} D_T \frac{\partial \psi_j}{\partial x} + \frac{\partial \psi_i}{\partial y} D_T \frac{\partial \psi_j}{\partial y} \right] dV. \qquad (97)
\end{aligned}$$

The shape functions were ψ_i and ψ_{si}, and the square matrices $[HK]$ and $[TK]$ were the stiffness matrices. $\{QW\}$ provided the boundary conditions for surface flux source at nodal point i. And finally, $[F]$ and $[Go]$ were the *capacitance* and *mass* matrices respectively.

Equation 97 was a vector of linearized partial differential equations. There was one first-order nonlinear ordinary differential equation for each node The nonlinearity stemmed from the functional dependence of [F] and [HK] upon Ψ. When an initial Ψ distribution was known, the unknown in equation 97 was $\dot{\Psi}$. That, in turn, allowed computation of Ψ at a later time.

The time integration of equation 97 followed the same steps as the integration of equation 89 over time. The transient finite difference form of the state variables derivatives was

$$\{\dot{\Psi}\} = \frac{1}{\Delta t}\{\{\Psi\}_{t+\Delta t} - \{\Psi\}_t\}, \tag{98}$$

and the state variable Ψ was formulated as

$$\{\Psi\} = \{(1-\theta)\{\Psi\}_t + \theta\{\Psi\}_{t+\Delta t}\}. \tag{99}$$

Here, the time dimension has been discretized into steps of duration Δt. At time t the state variables (T and Ψ) were known. The values of the state variables at time $T + \Delta t$ were unknown. Using the parameter θ, $\{\Psi\}$ in equation 97 was replaced by the values of Ψ at time level $t + \Delta t$. The Crank-Nicolson method with $\theta = 1/2$ was used.

Substituting equations 98 and 99 into 97,

$$\frac{[F]}{\Delta t}\Big\{\{\Psi\}_{t+\Delta t} - \{\Psi\}_t\Big\} + [HK]\Big\{(1-\theta)\{\Psi\}_t + \theta\{\Psi\}_{t+\Delta t}\Big\} = \{QW\} - [TK]\{T\} - [Go]\{\dot{T}\}. \tag{100}$$

Rearranging,

$$\left[\frac{[F]}{\Delta t} + \theta[HK]\right]\{\Psi\}_{t+\Delta t} = \left[\frac{[F]}{\Delta t} - (1-\theta)[HK]\right]\{\Psi\}_t + \{QW\} - [TK]\{T\} - [Go]\{\dot{T}\}. \tag{101}$$

The unknown in equation 101 was $\Psi_{t+\Delta t}$. All other terms were considered known. For example, T and $\dot{T}$ could have been replaced as in equation 98 and 99,

but they were treated as knowns. However, the values of T had to be determined at time $t + \Delta t$. Similarly, when the matrices and vectors in equation 101 were time independent, they had to be evaluated at time $t + \Delta t$. Nevertheless, one technique to improve the stability of a numerical solution was to evaluate the coefficient matrices at an earlier time than the state variables (Neuman, 1973). The time level for $\{QW\}$ had to be consistent with the other time levels used, but since boundary fluxes and point sources were taken as constants over a given time step, these quantities were independent of time level.

Program *QM* was coded to solve equation 101 with coefficient matrices as defined in equation 97. A flowchart can be found in Appendix C. The coefficient matrix on the left-hand side of equation 101 was the stiffness matrix. The whole right-hand side was evaluated as a vector of known numbers. Note that the composite stiffness matrix consisted of a capacitance matrix, $[F]$, and $[HK]$, also commonly called a stiffness matrix. The weighting of these two components by $1/\Delta T$ and by θ determined the relative importance of each in the overall stiffness matrix. The usual setting was for $\theta = 1/2$ for both the state variables and coefficient matrices. However, the optimum determination of Δt and θ remained an art more than a science, and was problem-independent.

Finally, it should be noted that the *global* stiffness matrix with Ψ was positive definite, an advantage that made numerical solution easier.

VI.5 Summary

The two coupled equations for heat transfer (94) and moisture migration (101) were derived for coding program *QM*. The heat flux portion of this model was an extension of the heat flux model verified in Chapters IV, but with additions of suction pressure, hydraulic conductivity, liquid sources, latent heat, and non-linear coefficients. The coupling of heat flux by suction pressure to moisture flow was quite weak. Therefore, the energy equation was virtually linear. The mass flow equation was highly non-linear. It consisted of Phillip and deVries's moisture model

and Hampton's variable change and an additional term to relate suction pressure to temperature. The two parabolic partial differential equations yielded T and Ψ, while the desired variables are T and ϕ_w. Although the variable ϕ_w also appeared in the mass equation, its value uniquely depended on Ψ and T because hysteresis was neglected.

CHAPTER VII

VALIDATION OF HEAT AND MASS TRANSFER MODELS

The theoretical equations for non-linear transient finite element heat and mass transfer in unsaturated compressible soils were developed in chapter VI. This chapter first presents (1) the model structure, followed by the (2) non-linear variables and then seeks to (3) validate and apply the numerical model.

The final model (QM- heat and mass transfer) combined the two coupled equations for heat transfer (Equation 94) and moisture migration (Equation 101) with the previous heat transfer model (QT - heat and temperature). In order to allow all simulations in this thesis to be performed by QM, it was designed with four options of operation:

- **QMode=0** Heat transfer with constant coefficients.
- **QMode=1** Heat transfer with non-linear (temperature dependent) coefficients.
- **QMode=2** Heat and mass transfer with non-linear coefficients.
- **QMode=3** Non-linear heat and mass transfer but with mass transfer limited to the temperature dependent terms of

$$-\left[\theta_w \beta_T + \left(\frac{\partial \theta_w}{\partial \Psi}\right)_{T,\sigma'} \left(\frac{\partial \Psi}{\partial T}\right)_{\theta_w,\Phi}\right] \frac{\partial T}{\partial t} = +\nabla \cdot (D_T \nabla T). \qquad (102)$$

VII.1 Model Structure

Unlike mass transfer, the energy equation was virtually linear since λ and C_{s+w} varied minimally with temperature and water content. Energy was always conducted and proportional to the temperature gradient.

Equations 94 and 101 formed a set of coupled, nonlinear, parabolic partial differential equations in T and Ψ. Although the variable θ_w also appeared, its value uniquely depended on Ψ and T because hysteresis was neglected.

The two dimensional finite element model was based on the Galerkin technique. The program should be compared with both analytical solutions and laboratory experiments on soil drying with a heat source. At the time of writing, there were no analytical solutions to the *coupled* heat and water flow equations available. However, Hampton (1989) experimentally measured temperature and moisture content at several points in a disk-shaped box of clay with a heating element in the center.

The general solution strategy was to first predict Ψ using either estimated or previously-determined values of Ψ and T. Then the updated Ψ values and previously-determined T values were used to solve the heat transfer or moisture equation. This procedure was repeated until convergence was achieved or the specified number of iterations was accomplished.

The matrix Equations 94 and 101 were solved using the direct solution technique of the Gaussian Elimination algorithm. Although this method used more computer time than iterative solutions, it yielded a more accurate solution. The coupled heat transfer and moisture transport equations could have been combined into one large matrix equation and solved simultaneously for Ψ and T. However, it was more efficient to solve such coupled equations separately and iterate between them. The use of smaller matrices required less storage space. Further efficiency was achieved by using most matrices to sequentially alternate their storage allocations between the separate equation-solving algorithms.

VII.2 Non-linear Model Calibration Variables

The heat and mass transfer model requires extensive calibration for the non-linear variables. Unfortunately, the author could not find sufficient data for one media to calibrate and validate the model. However, variable values were assembled from different sources and media to illustrate the method of calibration and to perform simulations.

If necessary, one can approximate the values of ρ_w and c_{vw} between 0 and 100°C as 1,000 kg/m^3-K and 4,190 J/kg-K, with uncertainties of four percent and one percent, respectively (Incropera and DeWitt, 1985).

Thermal conductivity, specific heat, and density as a function of temperature were experimentally measured at Texas A&M University (Lambert, 1994) for four media: (1) Mississippi river clay, (2) silt loam at 8% and (3) 14% moisture content, and (4) a mixture of 12% bentonite and 25% sand. At 22°C and 14% moisture content, the thermal conductivity was 1.18 W/m-°C, while the specific heat was 3406 J/kg-°C. The experimental uncertainty was 15% for thermal conductivity and 10% for specific heat. A best fit equation for the silt loam thermal conductivity was:

$$\lambda_{sc}(T,\theta_w) = -4.0172\theta_w^2 = 4.4239\theta_w + 0.00265T + 0.152, \tag{103}$$

from the two volumetric water content points and temperature equations at 22°C. Comparison of Equation 103 with the Lambert (1994) data yielded a maximum error of -4% in the range of $22 \leq T \leq 57°C$ and $0.172 \leq \theta_w \leq 0.3$. The backfill thermal conductivity at 22°C was 1.28 W/m-°C, and the moisture independent equation was

$$\lambda_{b'fil}(T) = 0.00202T + 1.24. \tag{104}$$

The specific heat equation as a function of volumetric water content was provided by Equation 71 while the associated generalized specific heat was given in Equation 73. The backfill specific heat was provided by Texas A&M University (Lambert, 1994) data and the resulting equation for C_{pg} was

$$C_{pg} = 23.06T + 3315.$$

The values used in Equation 85 for ρ_w (in kg/m^3) and L (in J/kg) are generated from the equations below:

$$\rho_w = 1000 + 0.0145T - 0.00515T^2, \tag{105}$$

and

$$L = 2.5 \times 10^6 - 2430T. \tag{106}$$

Here ρ_w (Finlay et al., 1978) may be calculated in the range $0 \leq T \leq 45°C$ and L (Hampton,1989) in the range of $0 \leq T \leq 120°C$. Other constants for the heat transfer equation were c_{vw}=4,190 kJ/kg, θ_o= 0.6 and θ_m= 0.46.

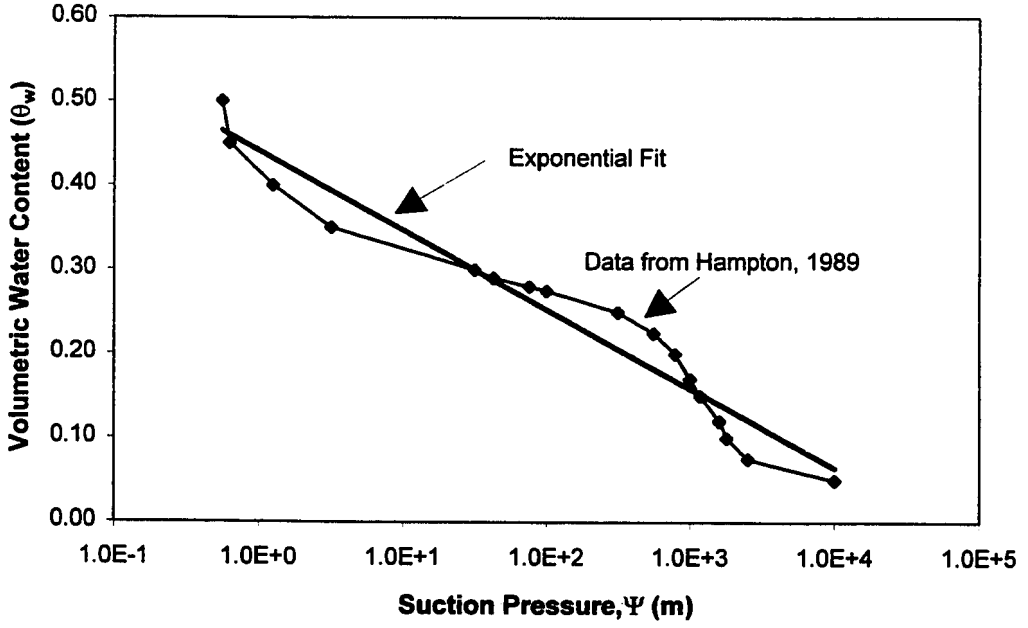

Figure 55. Volumetric water content (VWC) vs suction pressure. Estimated from Hampton (1989)

The moisture equation required additional equations for suction pressure, and hydraulic conductivity, expansivity, porosity, and specific storage. Perhaps the most important data were the suction pressure and hydraulic conductivity curves which were not available for silty loam. However, graphical values for a type of clay (from Solar Village, Colorado) were provided by Hampton (1989). The data is approximately reproduced in Figures 55 and 56. A commercial spreadsheet (Microsoft Excel) was used to approximate the curves with the exponential curve fit shown on the figures, and the associated equation for water content was

$$\theta_w = -0.0409ln(\Psi) + 0.4415, \tag{107}$$

while hydraulic conductivity was

$$\bar{K}_w = 9 \times 10^{-13} exp^{-0.0046\Psi}. \tag{108}$$

In Equation 107 and 108, the coefficient of determination (R^2) was 0.95 and 0.98, respectively. The gradients used in QM were derivatives of similar equations but more accurately valid over three sub-intervals.

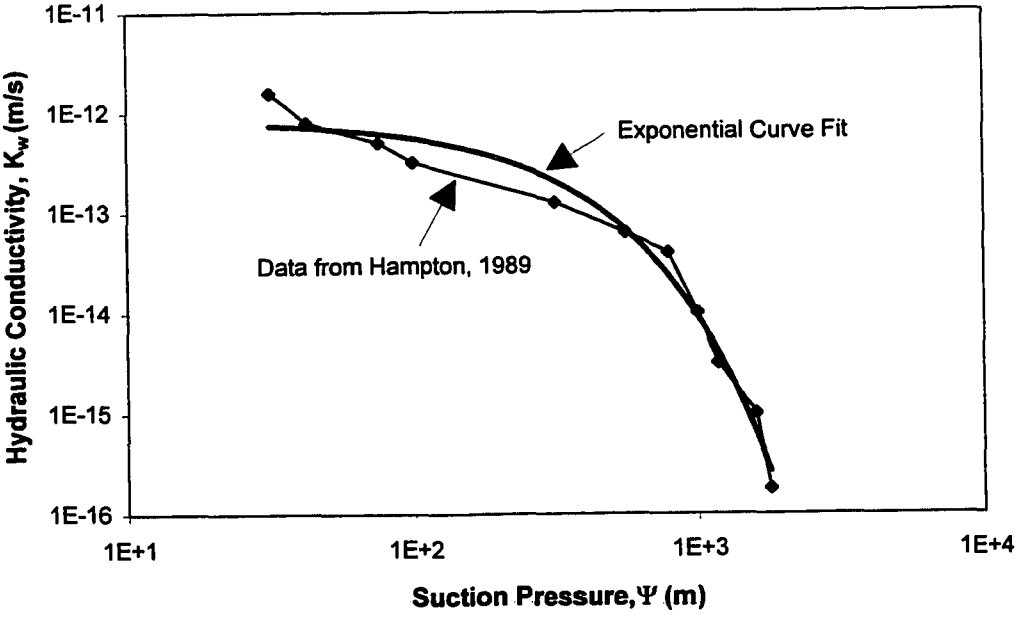

Figure 56. Suction pressure vs hydraulic conductivity. Estimated from Hampton (1989)

The author assumed that the most crucial missing data were that relating suction pressure to temperature, which was not available for any soil. The author approximated this value by calculating the ideal gas (air) gradient as

$$\frac{\partial \Psi}{\partial T} \approx \frac{\partial P_{air}}{\partial T} \approx 0.107 \frac{m}{^{\circ}C}. \tag{109}$$

The liquid thermal expansivity β_T for a general soil was provided by (Hampton, 1989) for the temperature range of $15 \leq T, \, ^{\circ}C \leq 122$ as

$$\beta_T = 2.2 \times 10^{-4} {}^{\circ}C^{-1}. \tag{110}$$

Porosity and specific storage were not available, so the values for Solar Village clay (Hampton, 1989) were used as 0.55 m^{-1} and 0.01 m^{-1}, respectively.

VII.3 Validation and Application

Heat transfer verification simulations were performed as a function of volumetric water content and Qmode. The results for heat transfer and backfill effectiveness ($\varepsilon_{b'fil}$) were plotted in Figures 57 and 58 respectively. The constant coefficient heat transfer (QMode=0) model did not show any changes as volumetric water content varied. However, the more realistic nonlinear heat transfer model (QMode=1) decreased heat transfer and backfill effectiveness by 17% and 16% respectively at steady state. Therefore, the use of a constant coefficient heat transfer model produced up to 17% overestimation of the heat transfer and backfill effectiveness when the volumetric water content decreased from 30% to 10%.

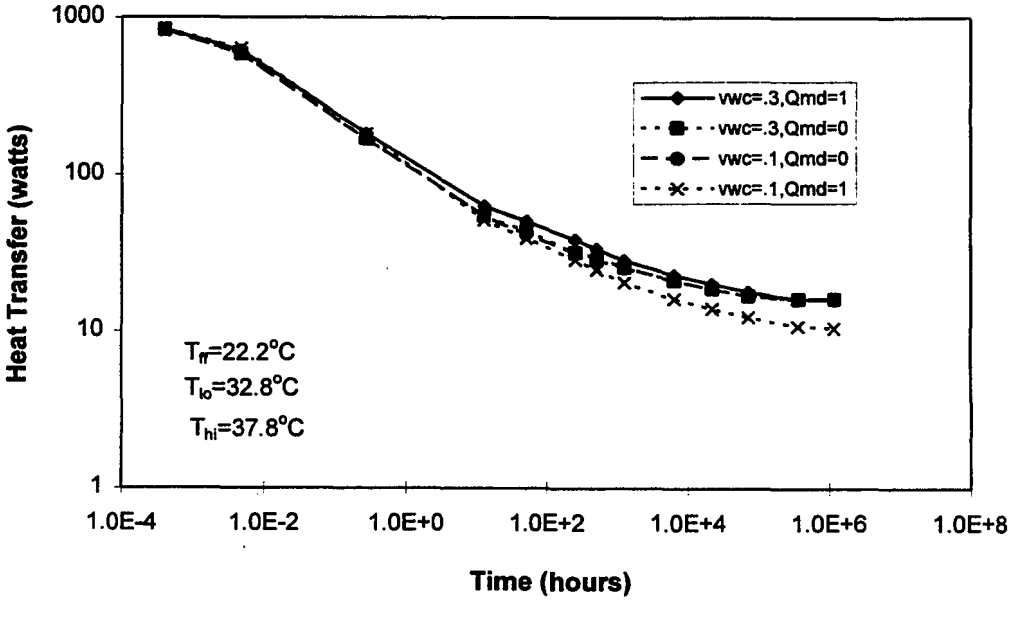

Figure 57. Heat transfer for various water contents and operation modes

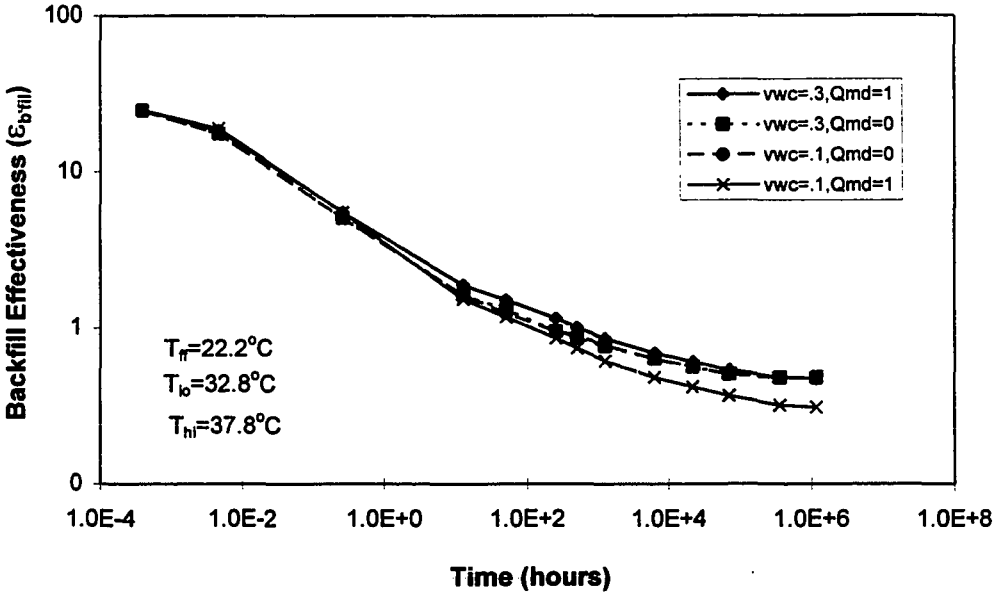

Figure 58. Backfill effectiveness for various water contents and operation modes

Finally, the heat and mass transfer model *QM* was compared with other GCHP models in Table 6. The major deficiency of *QM* was the lack of soil moisture freezing, and data to calibrate the mass transfer. However, *QM* was the only model that provided cylindrical source simulation and thermal effect of backfill material. In addition, the horizontal configuration, and model flexibility in handling boundary conditions and non-homogenous media allowed the robust parametric analysis in this thesis.

VII.4 Summary

This chapter first outlined the model structure and solution strategy. Next the non-linear model calibration coefficients were introduced. Finally simulations results were presented. The most important non-linear variables were the ones relating how increasing the temperature increased the suction pressure (suction pressure is

Table 6. Comparison of author's model with various models

REFERENCES	ANALYTICAL METHOD	INTERACTIONS OR FACTORS ACCOUNTED FOR						
		ON/OFF CYCLING	SOIL MOISTURE FREEZING	SEASONAL EARTH TEMPERATURE VARIATION	THERMAL INTERFERENCE EFFECTS	THERMAL EFFECT OF BACKFILL MATERIAL	FLUID TEMP. LEAVING GROUND HEAT EXCHANGER	SURFACE EFFECTS
Hackner, Hughes, Giffin	Kelvin Line-Source	No	Yes (empirical)	Yes	Yes	No	Yes	No
Mei	Numerical (FD)	Yes	Yes	Yes	Yes (two coils)	Yes	Yes	Yes
Metz, Andrews	Numerical (FE)	Yes	No	Yes	No	No	Yes	Yes
Claesson, Eskilson	Line-Source	Yes	No	Yes	Yes	Yes	Yes	Yes
Bose	Kelvin Line-Source	No	No	Yes	Yes	No	No	Yes
Hart, Couvillion	Kelvin Line-Source (FE)	Yes	Yes (approximate)	Yes (max, min only)	Yes	No	Yes	Yes
Muraya	Numerical Cylindrical Source (FE) Non-Linear	Yes	No	Yes (approximate)	Yes (up to seven coils)	Yes	Yes (Boundary Condition)	Yes

negative so actual pressure decreased), while the hydraulic conductivity ($K_{\Psi v}$) and water content (θ_w) decreased.

At the time of writing, the status of the model was to model the heat flux at any given moisture content. The variables were not all available for the same media, and $\partial\Psi/\partial T$ was not available for any media. Therefore, while the model predicted the moisture content variation with time for heat loading, this moisture flow was not verified for accuracy. The heat flux model was an extension of the linear model verified in Chapters IV, but with refinements of non-linear coefficients. The coupling of heat flux by suction pressure to moisture flow was quite weak.

CHAPTER VIII

APPLICATION TO GCHP SYSTEM DESIGN

This chapter provides guidelines for applying the results from the finite element heat and mass transfer computations in this thesis. The intent was to apply design theory to practical field situations.

A parametric analysis of overall performance for different spacings and backfill materials was performed in this thesis. These results are generalized here to allow GCHP installers to examine a wide range of configurations. Some of the physical data were provided by a three-ton GCHP that was installed at Abilene, Texas, and monitored via a remote data acquisition system for time intervals of one to 30 minutes.

VIII.1 Sizing Criteria

Chapter IV outlined how the numerical grid of Figure 27 was used to examine separation distances of 0 to 14 radii. The maximum pipe separation was limited by two factors. First, because the two pipe legs are usually connected at the bottom, they must be inserted into the same bore hole. Spacers would be required to maintain a constant separation distance. Secondly, it was only cost effective to use standard bore hole sizes. The cost effective standard bore drills are 4, 6, and 8 inches in diameter (0.1 to 0.2 meters). Therefore, if the heat pump pipes have a typical outer diameter of 2.7cm (1 inch nominal pipes), then the economical separation range would be 0 to 13 radii (l/D_o= 1 to 6.6). A larger separation would require a larger bore hole than available standard sizes, or drilling two parallel bore holes and establishing communication at the bottom of the holes.

Heat pump installers should optimize leg spacing to minimize thermal interaction between adjacent legs. Low cost, small bore holes with the legs touching have maximum short circuiting. Conversely, higher cost, bigger diameter holes have large leg separation distances and less thermal short circuiting. Therefore, thermal short

circuiting as a function of separation distance was quantified to determine optimal spacing.

VIII.2 Application of Heat Transfer Models

Most of the application issues come from Chapter V, *Applications of Heat Transfer Models*. The first issue is the type of boundary condition – whether the GCHP is at constant temperature or constant heat transfer rate. For touching sources and a constant temperature imposed on the outer surface, the equivalent radius was two radii. Therefore, a single two radii in size source had the same effect as two, one-radii sources because their surface areas were equivalent. The simulated heat output of the two sources exceeded the two-radii source by 22% initially and went down to 4% at steady state. For touching sources and a constant heat flux imposed on a cross sectional area, the equivalent radius was $\sqrt{2}$. Therefore, imposing a heat flux density (q''/A) on a 1.414 radii source was equivalent to imposing the same heat flux on two one-radii sources because their areas were equivalent.

To quantify GCHP performance, the short circuiting (Λ) and thermal effectiveness (ε_Λ) were defined in Equations 60 and 59. For two similar temperature sources, the thermal effectiveness (Figure 30) ranged from 52% for touching sources to 62% at an $l/D_o = 7$. Therefore, there was substantial thermal short circuiting throughout the separation range of 0 to 14 radii. Even at 14 radii, installers should compensate with 38% over-sizing based on single coil calculations. In addition, attempts should be made to allow a minimum separation of four radii to increase ε_Λ by 10%. However, there was an increased cost associated with the larger separation due to the higher drilling costs.

In actual operation, the two heat pump legs operate at different temperatures. For example, during operation in July, 1990, summer temperatures from the heat pump installation in Abilene, Texas, averaged 33.1°C for entry water and 28.4°C for outdoor air temperatures Dobson (1991). The condenser refrigerant temperatures were estimated as 3 to 6°C below entry water temperatures. In addition, sometimes

temperatures exceeded 37.8°C (100°F). Therefore, simulations were performed using an exit temperature of 37.8°C and a return temperature from the ground of 32.8°C. The thermal effectiveness (Figure 34) ranged from 55% for touching sources to 64% at an $l/D_o = 7$. Therefore, the thermal effectiveness for dissimilar sources increased over similar sources by about 2%.

Some installers size GCHPs on the basis of equivalent radii. The most common equivalent radius value was the $\sqrt{2}$, recommended by Claesson and Dunard (1983), Bose (1985), and others. A heat flux equivalent radius, $r_{h,eqv}$, was defined in Equation 65 as the equivalent number of sources, and logically ranged from one to two. The $r_{h,eqv}$ for similar temperatures was plotted in Figure 33 and ranged from 1.05 for touching sources to 1.2 sources for a separation of seven l/D_o. Dissimilar temperatures increased the $r_{h,eqv}$ range to 1.1 through 1.28 in Figure 37. The heat flux equivalent radius $r_{h,eqv}$ was found to be close to the values of constant temperatures for $l/D_o \geq 4$.

Significant error can result from using $r_{h,eqv} = \sqrt{2}$ with separated sources. The equivalent radius of $\sqrt{2}r_o$ for similar temperatures implies $Q_{eqv}/[(Q_1 + Q_2)/2] = \sqrt{2}$. As separation ranged from l/D_o=0 to 7, the FE model $r_{h,eqv}$ or the ratio $Q_{eqv}/[(Q_1 + Q_2)/2]$ ranged from 1.05 to 1.23. Therefore, the Claesson solution would overestimate the heat transfer by 36% to 18%.

The effect of temperature variation on thermal effectiveness was investigated. There was no significant change in ε_Λ from varying the farfield temperature or the temperature deviation between two coils. Most importantly, the thermal effectiveness was produced numerically in Table 3 as a function of separation distance.

VIII.2.1 Backfill (Non-homogenous properties)

Heat pump installations include non-homogenous materials of water, pipe, backfill, and various soil compositions. In addition, the soil properties vary with depth (3-D) and to a lesser degree with time and horizontally in the case of multiple bore holes. Other variances include the pipe material and contact resistances between the filler and the pipe or soil.

Soil replacement after trenching should minimize contact resistance (Bose, 1985). One reference, (AIEE, 1960), stated that 20% of the earth's thermal resistance is in the first six inches of soil around the pipe. Additives are used to

> ... enhance the thermal characteristics of a bentonite grout by resulting in a mixture with high sustained thermal conductivity, low shrinkage coefficient, low susceptibility to drying with capability of natural rewetting if dried, extremely low permeability, and pumpability characteristics that allow easy insertion into the bore hole. In addition, the additive must be readily available, economically justifiable, nontoxic, chemically inert, and nonpolluting with respect to the groundwater. (Remund and Lund, 1993)

Several soil thermal improvement additives (for particle bonding) have been identified (Bose, 1984) in the more advanced power cable industry and include:

- moisture insensitive thermal products,
- wax,
- cement, and
- non-swelling clays.

A study was performed to examine the impact on the performance from varying the thermophysical properties of the surrounding media (backfill). The numerical approximation of a heat exchanger with backfill was presented in Figure 42. Water, polyethylene pipe, backfill, and soil were all included. Since there were three sets of twin pipe legs, this represented the maximum possible temperature difference between legs. However, the author postulated that actual adjacent pipe leg temperatures differences should only be one or two degrees (in a three hole system this amounts to 3-6° C total). Temperatures of 37.8°C and 32.8°C were inserted into the model to calculate thermal short circuiting and equivalent radius.

The Texas A&M University installation at College Station, Texas, utilized bentonite mixed with masonry sand. The measured thermal conductivity was 1.6 W/m-K, which was near the maximum possible conductivity of 1.74 W/m-K with a 70% quartz mix (Remund and Lund, 1993). It should be noted that the bentonite and sand mixture thermal conductivities were lower than that of the soil.

Laboratory data for the thermal conductivity of bentonite grout backfills with additives was provided by Remund and Lund (1993). The results in Figure 43 showed the thermal conductivities ranging from 0.6 to 0.9 W/m-° C. In comparison, the conductivities of soils used in the design of GCHP systems ranged from 0.35 for light, dry soil to 2.42 W/m-° C for heavy, saturated soil. Bentonite without additives had a lower conductivity than all but light, dry soils.

Numerical simulations were performed with the four values of backfill thermal conductivity listed in Table 4: 0.782, 1.6, 8.65, and 1,000 W/m-K. Remund's experimental values for bentonite were a minimum of 0.782 W/m-K for pure bentonite. The Texas A&M University installation at College Station, Texas, utilized bentonite mixed with masonry sand. The measured thermal conductivity was 1.6 W/m-K, which was near Remund's maximum possible conductivity of 1.74 W/m-K with a 70% quartz mix. It should be noted that the bentonite and sand mixture thermal conductivities were lower than that of the soil. Because there was much room for improving backfill conductivity, 8.65 W/m-K was selected to study the possible benefits. In addition, enhancing thermal conductivity affects the competing phenomena of increased heat transfer and increased thermal short circuiting. As a result the maximum heat transfer for this FE grid was found to occur at 1,000 W/m-K. The four numerical simulations used the same backfill density and specific heat.

Three simulations were performed for each of the four backfill conductivities to determine the total heat transferred to the ground for Q_{lo}, Q_{hi}, and Q_{eqv}.

At all separation distances, increasing the thermal conductivity from 0.782 to 1.6 W/m-° C (0% sand) increased the heat transfer by 105%. Increasing the conductivity above 1.6 W/m-°C to 8.65 and 1,000 W/m-°C, increased the heat transfer by 8% and 18%. Therefore, the thermal conductivity of backfill should be increased to maximize the amount of heat dissipated to the soil. However, diminishing incremental increases in the heat transfer rate occurred for thermal conductivities above that of the surrounding soil.

The values for equivalent heat flux radius ($r_{h,eqv}$) and thermal effectiveness (ε_Λ) increased with separation distance and lower backfill conductivities. In general, $r_{h,eqv}$

and ε_Λ should be maximized to maximize heat transfer. However, maximization was not a sufficient criteria to rank backfills because the overall heat dissipation to the soil decreased while $r_{h,eqv}$ and ε_Λ increased.

As a result, neither $r_{h,eqv}$ nor ε_Λ was sufficient for evaluating backfills because they decreased with higher thermal conductivities which increase heat transfer. Another method of ranking backfill materials was given by Couvillion and Cotton (1990) in Equation 68.

The numerical ranking of the four backfill conductivities was plotted in Figure 47. The backfill effectiveness $\varepsilon_{b'fil}$ ranged from 0.47 to 0.55 (at k=1.6W/m-K) as the separation distance increased. Backfill effectiveness increased by 25% as the thermal conductivity increased from k=0.782 to 1,000 W/m-K. The maximum possible $\varepsilon_{b'fil}$ was 0.648 at k=1,000 W/m-K and l/D_o=7. Therefore, $\varepsilon_{b'fil}$ increased with thermal conductivity which was consistent with more heat dissipation to the soil. As a result, $\varepsilon_{b'fil}$ was a better method of ranking backfill than thermal effectiveness (ε_Λ) or heat flux equivalent radius ($r_{h,eqv}$) because of correlation with heat dissipation.

VIII.2.1.1 Summary of Backfill

Thermal conductivity of backfill needs to be improved. The bentonite backfill used at Texas A&M University possessed lower thermal conductivity than the native soil. In ranking backfills, the $r_{h,eqv}$ and ε_Λ must be compared with the overall performance criteria of net heat dissipated to the ground. A better ranking of backfill performance was $\varepsilon_{b'fil}$ because of consistency with the overall heat exchanger performance.

VIII.2.2 Case Study: Comparison with Mei Experiment

A case study was performed to incorporate backfill, equivalent diameter, and experimental data. For comparison with Mei (1988), the author's nine-source grid was modified as shown in Figure 48. The two pipes were separated by rubber insulation, and iron encases the bore hole. The six material properties were given in Table 5.

Replacing the rubber insulation with 14 times higher conductivity cement only increased the heat transfer by 0.04%. This implied that the insulation had negligible effect on the overall heat transfer.

The equivalent radius (in Figure 49) after one hour was 1.18. The radius declined with time to reach a steady-state value of 1.04. Therefore, at all times, $r_{h,eqv}$ was lower than the Mei value of 1.3 which was monitored between 120-720 hours (5-30 days). However, one must note that Mei solved for $r_{h,eqv}$ by comparing his models calculated fluid exit temperatures with experimental fluid exit temperatures. In addition, Mei did not explain the verification of the single isolated source of $r_{h,eqv} = 1$. Finally, Mei's method examined the entire water loop, while the author's model only examines a cross-section with constant imposed temperatures. While it was advantageous to examine the entire loop, Mei's $r_{h,eqv}$ was a function of the varying soil properties of clay at shallow depth, a 60° slope limestone shelf, a water table at 9 m, and three wells bordering at a 30° slope decline. In conclusion, the two equivalent radii deviated by 8% to 19% partly because they were derived differently. Mei did not present a transient analysis.

VIII.2.3 Multi-pipe Installations

Some GCHP installers have installed more than two pipes in the same bore hole to minimize drilling costs. One example is four pipes consisting of two supply pipes (higher temperature) and two return pipes (low). The two options were shown in Figure 50. The author's nine-source grid allowed examination of up to nine pipes in the same hole using the flat spacing method of Figure 50. These four pipes were incorporated into the FE grid shown in Figure 51. The model allowed examination of hole size range of l/D_o=4 to 9 and hot versus cold pipes separation distance of l/D_o=0 to 5. The results for backfill thermal conductivities of k=0.782, 1.6, and 8.65 W/m-°C were presented in Figure 52. For the bentonite backfill conductivity of 1.6 W/m-°C, the ratio of four pipes heat transfer to two pipes ranged from 1.02 to 1.06 ($Q_{4\text{pipes}}/Q_{2\text{pipes}}$). This increase was very small, and even the use of very high conductivity backfills (k=8.65 W/m-°C) only increased the ratio to 1.12.

Therefore, at steady-state, the author would only recommend more than two pipes with high conductivity backfills. For a given hole size, the four pipes allowed more convective surface area, but also a shorter separation by two diameters. Therefore, short circuiting negated the effect of more surface area.

VIII.2.4 Conclusions on Applications

The primary importance for the studies in this thesis was the rate of heat transfer between the GCHP and the surrounding soil. This rate of heat transfer was the ability of the fluid to approach the far field temperature. With knowledge of the soil conductivity and moisture content, an installer can use a table such as Table 7 to determine the required percentage increase in heat exchanger length for different types of soil. Changing from a heavy damp soil to the light dry soils requires doubling the heat exchanger length for horizontal GCHP. For vertical GCHP, ordinary rock requires 35% longer heat exchangers than dense rock.

VIII.2.4.1 Cost and Efficiency of Bore Holes

The primary design decision for GCHP installers is the bore hole length and width. The data from the non-homogenous grid was used to produce the associated costs in Table 8. Increasing the bore hole width decreases short circuiting and allows more heat transfer to the soil. Therefore, a shorter length is required. However, increasing the width increases the drilling cost, and amount of backfill to be purchased. Therefore, the pipe length should optimize the hole width. The most common bore hole sizes are 4,6, and 8 inches (0.1 to 0.2 m). Using larger drill bits has a substantial cost penalty. The resulting bore hole costs in Table 8 were proportionally varied with the bore hole width from $7,000 to $28,000.

To examine the entire economics, the cost of operation was added to the bore hole cost in Table 9. The consumption assumed a three-ton unit operating at 0.9 kW/ton and a fractional on-cycle time of 25energy cost of $0.05/kWh, the five year consumption cost ranged from $1,850 to $2,200. Therefore, the consumption cost was negligible compared to the capital cost of the bore holes which varied with width. Therefore, the increased heat transfer from wider bore holes was not economical.

Table 7. Earth loop size by configuration and soil type. (EPRI,1989)

a) Horizontal (Trench Feet per Nominal Ton) for Heavy Damp Soil Type--Percentage Increase in Length for Other Soil Types

Configuration	Heavy Damp	Heavy Dry	Light Damp	Light Dry
Horizontal-One-Pipe	353 ft	15%	24%	106%
Horizontal-Two-Pipe	216 ft	16%	25%	106%
Horizontal-Two-Pipe	218 ft	16%	26%	106%
Horizontal-Four-Pipe (Square)	144 ft	18%	27%	107%
Horizontal-Four-Pipe (In-LIne)	148 ft	17%	27%	114%

b) Vertical (Bore Feet per Nominal Ton) for Dense Rock--Percentage Increase in Depth for Ordinary Rock

Configuration	Dense Rock	Ordinary Rock
Vertical	135 ft	35%

Next, the costs were computed as a function of backfill thermal conductivity in table 10. The backfill conductivities are from Chapter V for a separation of seven l/D_o. The bordered row in each of Tables 8, 9, and 10 was equivalent. The major assumption is that fictitious high conductivity backfills (k=8.65 and 1,000 W/m-k) are available at the bentonite/sand cost of $5.50/bag. As noted in Chapter V, at 1,000 W/m-k, no additional increases in bore hole size are required because the amount of short circuiting does not vary. The results showed that the total cost savings for a 1,000 W/m-k backfill were 11%.

Table 8. Cost vs bore hole width

Bore hole (inches)	Bore hole (meters)	Pipe Separation (l/D_o)	Q-net (W/m)	Length[1] (meters)	Unit[2] Cost ($/meter)	Length Cost ($)	Filler Volume (m^3)	Bentonite/ Sand (bags)	Cost[2] $5.5/bag ($)	Bore Cost ($)
2	0.051	0	21.28	187	26	$4,913	0.4	3.5	$19	$4,932
4	0.102	2	22.76	175	36	$6,316	1.4	13.1	$72	$6,388
6	0.152	4	23.85	167	49	$8,219	3.0	28.2	$155	$8,374
8	0.203	6	24.47	163	62	$10,146	5.3	48.9	$269	$10,415
10	0.254	8	25.16	158	85	$13,504	8.0	74.3	$408	$13,912
12	0.305	10	25.36	157	131	$20,611	11.5	106.1	$584	$21,195
14	0.356	12	25.51	156	164	$25,612	15.5	143.6	$790	$26,402

[1] 167 m for medium rock, medium bore hole and 3-ton unit [EPRI, pg 1-2, (1989)].

[2] Christiansen & Boyles Products Inc. Estimated by author

Soil Properties: k=1.73 W/m-k; α=9.7E-7 m^2/sec; ρ=2,082 kg/m^3

Table 9. Consumption and bore hole cost

Bore hole (inches)	Bore hole (meters)	Pipe Separation (l/Do)	Q-net (W/m)	Consumption (kWh/yr)	Cost $0.07/kWh ($/yr)	Consumption 5 yr Cost ($)	Bore Hole Cost ($)	Total 5 yr Cost ($)
2	0.051	0	21.28	6324	443	2213	4932	$7,145
4	0.102	2	22.76	5913	414	2070	6388	$8,457
6	0.152	4	23.85	5643	395	1975	8374	$10,349
8	0.203	6	24.47	5500	385	1925	10415	$12,340
10	0.254	8	25.16	5349	374	1872	13912	$15,784
12	0.305	10	25.36	5307	371	1857	21195	$23,052
14	0.356	12	25.51	5276	369	1846	26402	$28,248

3 ton unit operating at 0.9 kW/ton with a 25% on-cycle time

VIII.2.4.1.1 Summary and Conclusions of Costs

This chapter first summarized the practical field applications from this thesis. Then the costs were introduced. The first limitation was the cost data, which varies with geographical locations and drilling companies. Another factor was the type of

Table 10. Cost vs backfill thermal conductivity

Backfill Conductivity (W/m-k)	Bore hole (meters)	Pipe Separation (I/D_o)	Q-net (W/m)	Length[1] (meters)	Unit[2] Cost ($/meter)	Length Cost ($)	Filler Volume (m^3)	Bentonite /Sand (bags)	Cost[2] $5.5/bag ($)	Total Cost ($)
0.78	0.152	4	22.58	176	49	$8,681	3.2	29.8	$164	$8,845
1.60	0.152	4	23.85	167	49	$8,219	3.0	28.2	$155	$8,374
1.79	0.152	4	24.05	166	49	$8,150	3.0	28.0	$154	$8,304
8.65	0.152	4	25.95	153	49	$7,553	2.8	25.9	$143	$7,696
1,000	0.152	4	26.91	148	49	$7,284	2.7	25.0	$137	$7,421

soil conductivity and moisture content. The overall cost of GCHPs was estimated, and it was not economical to use wider bore holes – even with high conductivity backfills. In fact the initial bore hole cost eclipsed the cost of operation and backfill conductivity. The dominance of the initial cost probably explains why air-source heat pumps are more commonly installed. However, if wider bore holes or higher conductivity backfills are available at the same costs, they should be used. In addition, Dobson (1991) estimated that long off-times can increase the efficiency by as much as 5%.

CHAPTER IX

CONCLUSIONS AND RECOMMENDATIONS

The initial classification of literature into nine sequential levels of complexity in modeling ground heat exchange showed that cylindrical source heat and mass transfer models have generally not been used for simulating without averaging the thermal effect of backfill materials, soil conductivities, water contents, pipe temperatures, and thermal interference. A cylindrical source model offers the potential for improved accuracy over the line source models used by many investigators.

First, two dimensional horizontal cross sectional heat transfer models with finite difference (FD) and finite elements (FE) were constructed. Then simplified versions of the heat transfer models were verified with existing analytical solutions and experimental data for various configurations. Comparison of the FE model with the analytical solutions of Ingersoll et al (1948) for a single cylindrical source of constant heat flux or temperature yielded excess errors of about 6% and less than 3%, respectively for less than 1300 operation hours. The validity of the simple geometry models was the basis of the assumption that the model could be extended for parametric analysis and the entire array of underground double (supply and return) variable heat water pipe network.

Most importantly, both models provided a parametric analysis tool for a horizontal cross section of GCHP and soil. On the contrary, most investigators have primarily modeled the overall ground loop of a GCHP using the two dimensions of depth and radial direction. Such analyses have approximated varying soil conductivities, water contents, pipe temperatures, and thermal interference with secondary interest and accuracy.

The parametric study was performed with the FE heat transfer model. First, results showed that two one-radius sources with constant temperature imposed, perform equivalent heating as one two-radii constant temperature source. However, for constant heating, the equivalent radius was found to be the $\sqrt{2}$ value cited by

Claesson and Dunard (1983) and others. Then it was shown that all equivalent radii vary with time and source separation, and that the heat flux equivalent diameter ($r_{h,eqv}$) is more preferable than the geometric radius ($r_{g,eqv}$). Next, the heat exchanger effectiveness (ε_Λ) was found be independent of the dimensionless temperature (of tubes and soil) and only varied with separation distance at steady state. Steady state as defined by less than 1% change was reached after 100,000 hours. The thermal short circuiting ranged from 38% to 47% in the reasonable installation separation range of seven l/D_o. Therefore, even at a separation of seven l/D_o, GCHP installers should compensate for 38% capacity derating from a two independent coils calculation. Finally, non-homogenous media were modeled while varying backfill. Maximum heat transfer (less than 1% change) was achieved with a fictitious backfill backfill thermal conductivity of 1,000 W/m-K, while measured bentonite conductivities were less than 2 W/m-K. The overall heat transfer increased with backfill thermal conductivity but ε_Λ decreased. Therefore, backfill effectiveness ($\varepsilon_{b'fil}$) was required to rank backfill performance. The range of $\varepsilon_{b'fil}$ was from 45% for touching bentonite tubes to 60% for the fictitious backfill at a separation of seven l/D_o. The resulting performances were analyzed to recommend optimum pipe leg spacing to balance wider bore hole costs and thermal short-circuiting of "hot" and "cold" legs.

Results showed that heat transfer, r_{eqv}, ε_Λ, and $\varepsilon_{b'fil}$ decreased with time and increased with separation distance. Therefore, a single value of each parameter could only be defined at steady state. Unfortunately, steady state times exceeded the equipment life cycle.

Many formulations of equivalent diameter have been proposed that are internally consistent with their heat transfer model. The types of r_{eqv} examined in this chapter were Mei's convective experimental set up, Claeson's dipole solution, the author's models for analytical constant temperature and constant heat source, and the author's numerical FE models for constant heat or constant temperature (geometric and heat flux radius). The author concluded that the most universal and meaningful equivalent diameter was $r_{h,eqv} = Q_{eqv}/[(Q_1 + Q_2)/2]$. This allowed direct expression

of the equivalent radius as the equivalent heat flux (e.g. $r_{h,eqv} = 1.414$ implies that the Q_{eqv} was 41.4% greater than the average single coil heat flux).

Theoretical and numerical models for non-linear transient finite element heat and mass transfer in unsaturated compressible soils were developed. The two coupled equations for heat flux (94) and moisture migration (101) were derived and coded. All models presented in this thesis were combined into one numerical model (QM-heat and mass) with four options of operation:

- **QMode=0** Heat transfer with constant coefficients.
- **QMode=1** Heat transfer with non-linear (temperature dependent) coefficients.
- **QMode=2** Heat and mass transfer with non-linear coefficients.
- **QMode=3** Non-linear heat and thermal mass transfer.

Establishing a moisture migration model required formulating coupled partial differential equations for non-linear heat and mass transfer. equations solved for temperature and suction pressure - while moisture content was a function of both variables. The model was constructed with nine terms to handle the rate of increase of water stored in the control volume and the resulting flux divergence. The required input variables were volumetric water content, suction pressure, specific storage, porosity, thermal expansivity, hydraulic conductivity, and thermal moisture diffusivity. However, there was not enough soil data to verify moisture prediction.

Performance degradation was computed for decreased water content which in turn decreased thermal conductivity. This knowledge of capacity derating with time is essential for sizing a unit— so that one can oversize the unit or anticipate a shorter life cycle. However, due to lack of comprehensive soil data, the transient mass transfer prediction could not be verified.

Initially both finite difference and finite element numerical models were developed. However, the finite element model outperformed the finite difference model in three ways. First, it handled complex geometrical configurations (circular, etc) and allowed various boundary conditions by merely changing the input file. Second, FE meshed the farfield with fewer, better behaved, and more stable elements. Third, the model allowed up to 15 terms (nine for mass flow and 6 for heat transfer) in the

soil physics equation. And finally, FE allowed the same elements and matrices to alternatively compute heat transfer and moisture flow.

Chapter VIII summarized the practical field applications from this thesis, and calculated costs. Economics did not justify wider bore holes – even with high conductivity backfills. The initial bore hole cost eclipsed the cost of operation and backfill conductivity. The dominance of the initial cost probably explains why air-source heat pumps are more commonly installed. However, if wider bore holes or higher conductivity backfills are available at the same costs, they should be used.

IX.1 Recommendations

There are three further recommendations for maximizing the model development. First, the model should be extended to more closely approximate a full scale three dimensional model using a series of horizontal cross sections. This would allow bin analysis of the entire GCHP load with a cylindrical source model that was accurate at all depths. However, this will probably require a super computer, and might not significantly improve heat transfer or heat transfer induced mass flow simulation. The two dimensional model should be quite accurate because horizontal temperature gradients are a magnitude greater than vertical gradients. This was evident in a typical installation (Dobson, 1991) where the temperature gradient was 3 to 6°C over 35 meters (750 feet) of water tubing, while the horizontal gradient between the water and soil exceeded 11° C over 15 meters.

Secondly, experimental soil and backfill data should be measured to verify the mass transfer model. Finally, the three dimensional heat and mass model should be used to perform parametric analysis to improve GCHP installation sizing criteria.

REFERENCES

AIEE, 1960, "Soil Thermal Characteristics in Relation to Underground Power Cables." *AIEE Proceedings,* Dec., pp. 792-856.

Becker, E. B., Carey, G. F., and Oden, J. T., 1981, *Finite Element Analysis*, Prentice-Hall, Inc., New Jersey.

Bose, J. E., and Parker, J. D., 1984, "Ground-Coupled Heat Pump Research", *ASHRAE Transactions*, Vol 89, pt. 2B, pp. 375-390.

Bose, J. E., Parker, J. D., and McQuiston, F. C., 1985, *Design/Data Manual for Closed-Loop Ground-Coupled Heat Pump Systems*, ASHRAE, Atlanta, Georgia.

Braud, H. J., Klimkowski, H., and Baker, F. E., 1983, *Earth-Coupled Water-Source Heat Pump Research, Design and Applications in Louisiana*, Louisiana Agricultural Experiment Station, Baton Rouge, Louisiana.

Cane, R. L. D., and Forgas, D. A., 1991. " Modeling of Ground-Source Heat Pump Performance", *ASHRAE Transactions*, Pt. 1 pp. 909-925.

Carslaw, H. S., and Jaegar, J. C., 1940, "Some Two-Dimensional Problems in Conduction of Heat Circular Symmetry", *Proceedings of the London Mathematical Society*, V. XLVI, pp. 361-388.

Claesson, J., and Dunard, A., 1983, *Heat Extraction from the Ground by Horizontal Pipes- A Mathematical Analysis*, Swedish Council for Building Research, Document D1, Stockholm, Sweden.

Couvillion, R. J., and Cotton, D. E., 1990. "Laboratory and Computer Comparisons of Ground-Coupled Heat Pump Backfills," *ASHRAE Transactions*, Vol. 96, Pt. 1.

Deerman, J. D., 1989, "Simulation of Vertical U-Tube Ground-Coupled Heat Pumps Systems Using the Cylindrical Heat Source Solution," *ASHRAE Transactions*, Vol. 97, Pt. 1.

De Lange, K. .J., August 1988, *A Mathematical Model for the Simulation of Closed-Loop Earth-Coupled Heat Exchangers for a Water Source Heat Pump*, M.S.Thesis, Texas A&M University, College Station.

Deng, Y., Fedler, C. B., 1992, "Multi-Layered Soil Effects on Vertical Ground-Coupled Heat Pump Design," *Trans of the ASAE*, Vol. 35, Iss. 2, pp. 687-694.

de Vries, D. A. 1958, "Simultaneous transfer of heat and moisture in porous media", *Trans. AGU*, Vol. 39, pp. 909-916.

de Vries, D. A., 1987, "The Theory of Heat and Moisture Transfer in Porous Media Revisited," *International Journal of Heat and Mass Transfer*, Vol. 30, No. 7, pp. 1343-1350.

Dobson, M. K., May 1991, *An Experimental and Analytical Study of the Transient Behaviour of Vertical U-Tube Ground-Coupled Heat Pumps in the Cooling Mode*, pp. 81, 85, 93, 135, M.S.Thesis, Texas A&M University, College Station.

Electric Power Research Institute, 1989, *Soil and Rock Classification According to Thermal Conductivity.* EPRI CU-6482, prepared by STS Consultants, Ltd, Chantilly, Virginia, pp. 2-6, Fig. A-36, and table 1-2.

Fischer, R. D., and Newman, D. C., 1981, *Final Report on Design of Ground-Coupled Heat Pump System for UT Solar House.* Columbus, Ohio, Battelle Columbus Laboratory.

Gonzalez, J. A., August 1993, *A Simplified Methodology for Sizing Ground Coupled Heat Pump Heat Exchangers in Cooling Dominated Climates*, Texas A&M University, College Station.

Hampton, D., 1989, *Coupled Heat and Fluid Flow in Saturated-Unsaturated Compressible Media*, Ph. D. Diss., Colorado State University, Fort Collins, Colorado, Fig. 3-4.

Hopkins, P. L., 1983, *A Study of a Solar-Assisted Ground Source Heat Pump*, M.S. Report, Oklahoma State University, Stillwater.

Incropera, F. P., DeWitt, D. P., 1985, *Fundamentals of Heat and Mass Transfer*, John Wiley & Sons, New York, pp. 521, and table A.6

Ingersoll, L. R., Zoeble, O. J., and Ingersol, A. C., 1948, *Heat Conduction with Engineering, Geological, and Other Applications*, McGraw-Hill, New York, New York.

Jaeger, J. C., 1942, "Radial Heat Flow in Circular Cylinders with a General Boundary Condition," *Journal of the Royal Society of New South Wales*, V. 74, pp. 342-352.

Kavanaugh, S. P., 1984, *Simulation and Experimental Verification of Vertical Ground-Coupled Heat Pump Systems*, Ph. D. Diss., Oklahoma State University, Stillwater, Oklahoma.

Lambert, M., 1994, Personal Communication, Texas A&M University, Mechanical Engineering Department, College Station, Texas.

Lei, T. -K., 1993, "Development of a Computational Model for a Ground-Coupled Heat Exchanger," submitted to *ASHRAE Transactions*, Vol. 99, Part 1.

Mei, V. C., and Baxter, V. D., 1986, "Performance of a Ground-Coupled Heat Pump with Multiple Dissimilar U-Tube Coils in Series," *ASHRAE Transactions*, Vol. 92, Part 2A, pp. 30-42.

Mei, V. C., 1988, "Heat Pump Ground Coil Analysis With Thermal Interference," *Journal of Solar Energy Engineering*, Vol 110, pp. 67-73.

Mohammad-zadeh, Y., Johnson, R. R., Edwards, J. A., 1990, "Thermal Simulation of Ground-Loop Heat Pump Systems," *Advanced Computational Methods in Heat Transfer*, Vol 3: Phase Change and Combustion Simulation, pp. 255-294.

Mulay, S. P., Worek, W. M., 1990, "Simultaneous Transport of Heat and Moisture in a Partially Saturated Porous Media," *International Communications in Heat and Mass Transfer*, Vol. 17, pp. 135-145.

Neuman, S. P., 1973, "Saturated-Unsaturated Seepage by Finite Elements," *J. Hydraul. Div., ASCE*, Vol. 12, pp. 2233-2250.

Özişik, M. Necati, 1980, *Heat Conduction*, John Wiley & Sons. pp. 490, New York, New York.

Patankar, Suhas V., 1991, *CONDUCT Computer Program*, Innovative Research Incorporated, Minneapolis, Minnesota.

Phillip, J. R. and D. A. de Vries, 1957, "Moisture Movement in Porous Materials under Temperature Gradients," *Trans. Am. Geophys. AGU*, Vol 38, pp. 222-232, and 594.

Pietsch, J. A., 1990, "Water-Loop Heat Pump Systems Assessment," *ASHRAE Transactions*, Vol. 92, Part 1, 1990, pp. 1029-1038.

Reddy, J. N., 1993, *An Introduction to the Finite Element Method*, McGraw-Hill, Inc., New York, New York, pp. 224-235.

Remund, C, P. and Lund, J. T. 1993, "Thermal Enhancement of Bentonite Grouts For Vertical GSHP Systems," Heat Pump and Refrigeration Systems Design, Analysis, and Applications, pp. 95, AES-Vol 29, *ASME Winter Annual Meeting*, New Orleans, Louisiana, Dec., pp. 98.

Schroeder, C. N., August 1984, *The Development of an Optimized Computer Simulation Model for Heat and Moisture Transfer in Soils*, Ph. D. Diss. Texas A&M University College Station, Texas.

Slegel, D. L., 1975, *Transient Heat and Mass Transfer in Soils in the Vicinity of Heated Porous Pipes*, Ph. D. Dissertation, Oregon State University, Corvallis, Oregeon.

Sorour, M. M., Saleh, M. M. and Mahmoud, R. A., 1990, "Thermal Conductivity and Diffusivity of Soil," *International Communications in Heat and Mass Transfer*, Vol. 17, pp. 189-199.

Strouboulis T., 1992, Classroom lectures, Associate professor of Aerospace Engineering, Texas A&M University, College Station, Texas.

Walker, W. R., 1981, *Studies of Heat Transfer and Water Migration in Soils*, Ph. D. Diss., Colorado State Univ., Fort Collins, Colorado.

Supplementary Sources Consulted

Andrews, J. W., P. D. Metz, and J.H. Saunders, 1984, "A Refined Computer Program for the Transient Simulation of Ground-Coupled Heat Pump Systems". technical report, Brookhaven National Laboratory 34818, April.

Baca, R. G., King, I. P. and Norton, W. R., 1978, *Finite Element Models for Simultaneous Heat and Moisture Transport in Unsaturated Soils, in Finite Elements in Water Resources,* C. A. Brebbia, ed., Pentech Press, London, pp. 1.19-1.35.

Cary, J. W., 1967, "Experimental Measurements of Soil-Moisture Hysteresis and Entrapped Air", *Soil Science*, Vol. 104 (3), pp. 174-180.

Cassel, D. K., 1968. *Soil-Water Behaviour in Relation to Imposed Temperature Gradients*, Ph. D. Dissertation, University of California, Davis, California.

Childs, S. W. 1982, " Coupled Heat and Moisture Transport in Unsaturated Soils," *Proc. of the Symp. on Unsaturated Flow and Transport Modeling*, E. M. Arnold, G. W. Gee and R. W. Nelson, eds., Report NUREG/CP-0030 and PNL-SA10325, held March 23-24, Seatle, Washington, pp. 55-75.

Dakshanamurthy, V. and D. G. Fredlund, 1981, "A Mathematical Model for Predicting Moisture Flow in an Unsaturated Soil Under Hydraulic and Temperature Gradients," *Water Resour. Res.*, Vol. 17 (3), pp. 714-722.

de Vries, D. A., Van Wijk, W. R. ed., 1963, *Thermal Properties of Soils, in Physics of Plant Environment*, North-Holland Publ. Co., Amsterdam, pp. 210-235.

Eskilson, P., 1987, *Thermal Analysis of Heat Extraction Boreholes, Department of Mathematical Physics*, University of Lund, Sweden.

Fipps, G., and Skaggs, R. W., 1989, "Modeling Three-Dimensional, Saturated and Unsaturated Flow Using Multigrids," *Transactions of the ASAE*, Vol. 32, No.4 pp. 1263-1268.

Giffin, T., 1986, *Earth-Coupled Heat Pump Demonstrations for Commercial Building Applications*, Final Report, Niagara Mohawk Power Corporation, Syracuse, New York, Vol. 2, July.

Hackner, R. J., P. J. Hughes, and R. A. O'Neal, 1987, "Design of ECHP Systems in Northern Climates," *ASHRAE Transactions*, Vol 93, Part 2.

Harmathy, T. Z., 1969, "Simultaneous Moisture and Heat Transfer in Porous Systems with Particular Reference to Drying," *Ind. Eng. Chem. Fundam.*, Vol. 8, pp. 92-99.

Hart, D. P., and R. Couvillion, 1986, *Earth-Coupled Heat Transfer*, Prepared for the National Water Well Association, Dublin, Ohio.

Hartley, J. G. and W. Z. Black, 1981, "Transient Simultaneous Heat and Mass Transfer in Moist, Unsaturated Soils," *J. Heat Transfer*, Vol. 103, pp. 376-382.

Hartley, J. G., 1987, "Coupled Heat and Moisture Transfer in Soils: A Review," Majumdar, A. S., Ed., *Advances in Drying*, Vol. 4, Hemisphere.

Milly, P. C. D. and P. S. Eagleson, 1980, *The Coupled Transport of Water and Heat in a Vertical Soil Column under Atmospheric Excitation,* Rept. No. 258, R.M. Parsons Lab. for Water Resources and Hydrodynamics, Dept. of Civil Eng., Massachusetts Institute of Technology, Cambridge, Massachusetts.

Muraya, N. K., Peterson, G. P., 1994, *A Review of Heat Pipe Applications in the Energy Industry*, Trends in Chemical Engineering 2, editor: S.G. Pandalai, McGraw-Hill, New York, New York, pp. 175-198, 1994.

Sidiropoulos, K., and C. Tzimopoulos, 1983, "Sensitivity Analysis of a Coupled Heat and Mass Transfer Model in Unsaturated Porous Media," *J. Hydrol.*, (Netherlands), Vol. 64, pp. 281-298.

Slegel, D. L., and L. R. Davis, 1977, "Transient Heat and Mass Transfer in Soils in the Vicinity of Heated Porous Pipes," *J. Heat Transfer, Trans. ASME*, Vol. 99 (4), pp. 541-546.

Somasundaram, S., Anand, N. K., and Suh, Y. B., 1989, "Analysis of Moisture Migration in Two-Dimensional Unsaturated Porous Media with Impermeable Boundaries," *International J. Heat and Mass Transfer*, Vol. 32, No. 9 pp. 1733-1739.

Sophocleous, M., 1979, "Analysis of Water and Heat Flow in Unsaturated-Saturated Porous Media," *Water Resour. Res.*, Vol. 5, pp. 1195-1206.

Szabo B., Babuska, I., 1991, *Finite Element Analysis*, John Wiley & Sons, Inc., New York, New York.

Walker, W. R., J. D. Sabey, and D. R. Hampton, 1981, *Studies of Heat Transfer and Water Migration in Soils*, DOE final report, April 1981, Dept. of Agricultural and Chem. Eng., Colorado State Univ., Fort Collins, Colorado.

Yeh, G. T., and R. J. Luxmoore, 1983, "Modeling Moisture and Thermal Transport in Unsaturated Porous Media," *J. Hydrol.*, (Netherlands), Vol. 64, pp. 299-309.

APPENDIX A

FINITE ELEMENT METHOD

This study developed two finite element (FE) codes: one for pure heat conduction, and the other for coupled heat conduction and moisture diffusion. Both heat transfer as well as heat and moisture transfer program structures consisted of the *preprocessor, processor, time loop, and post processor* shown in Figure 59. In addition, both equations use the same general systematic method for calculating element matrices and equations.

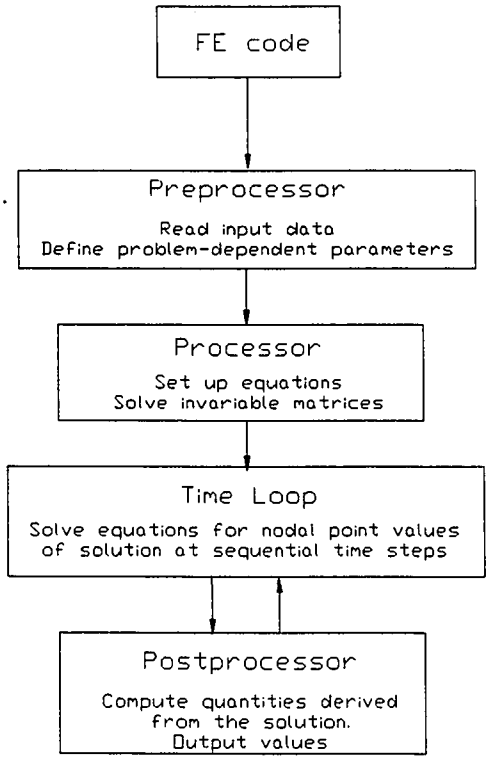

Figure 59. The FE structures of preprocessor, processor, time loop, and post processor

This appendix presents the mutual *finite element* (FE) method variations utilized in the *preprocessor* and *processor*. Physically, this involves outlining the systematic FE method of solving variational calculus of two point boundary value problems. The variational formulations for finite element equations are derived in Chapter III for heat conduction, and Chapter VI for coupled heat and moisture diffusion. Respective flow charts are included in Appendix B and C. The three-level flowcharts consist of the overall structure, the layout of subroutines, and the tasks of each subroutine.

A.1 Finite Element Method

The basis for implementing the finite element method is a master element $\hat{\Omega}$ on which all pertinent computations for the actual grid are performed. Different kinds of finite elements (FE) may be calculated with the general FE method. Therefore, a variational problem statement must specify an element type which entails

1. a prescription of the *master element* for generating the element grid,
2. the *element map* T_e from the master to the grid,
3. shape functions for *interpolation*, and
4. integration *quadrature* rules.

A.2 Master Element

The FE method is a systematic means of constructing reasonable basis functions from approximate variational calculus. The master element is a typical finite element isolated from the grid and with its own coordinate system (ξ, η). The master element $\hat{\Omega}$ is used to generate the actual finite element grid Ω_e. In addition all computations are performed on the master element. Therefore, one must define the geometry of the master element $\hat{\Omega}$ and define the element's coordinate system (ξ, η). The two codes work with two dimensional triangular elements (3 or 6 noded) or quadrilateral elements (4,8, or 9 noded). The master element for all quadrilaterals is shown in

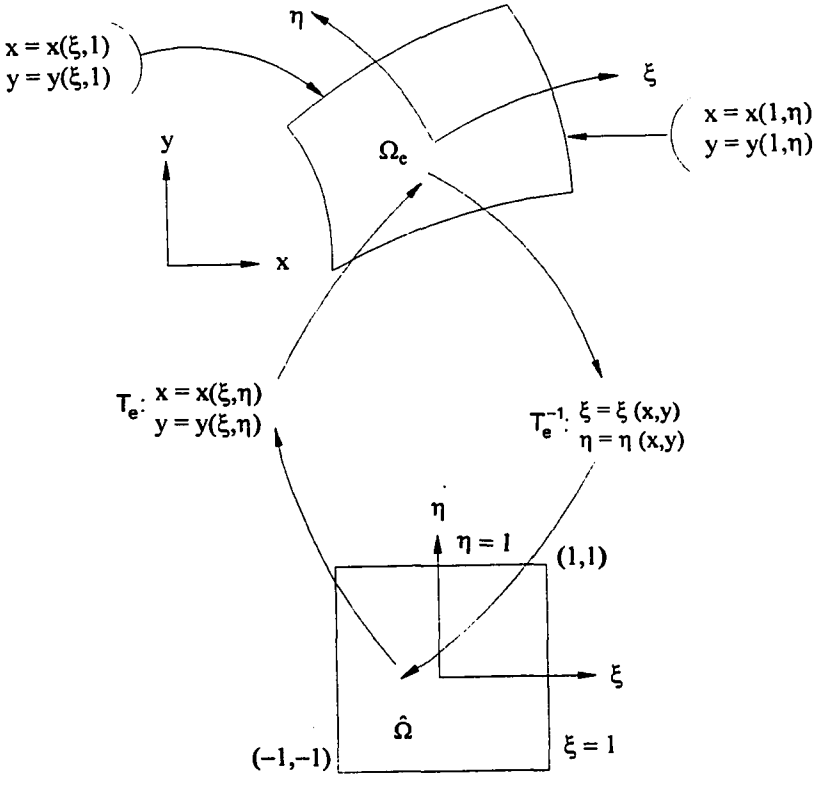

Figure 60. Quadrilateral linear mapping. T_e from the master element $\hat{\Omega}$, to the actual grid Ω_e, and reverse map T_e^{-1}.

Figure 60, while the the master element for all triangles is shown in Figure 61. Both master elements use (ξ, η) coordinates but with different geometrical orientations.

A.3 Element Map T_e

The linear element map T_e is used to convert master element $\hat{\Omega}$ geometry and computations to the actual finite element Ω_e grid. Figures 60 and 61 also show the linear mapping from (ξ, η) to the actual grid coordinates of (x, y) for quadrilateral and triangular elements respectively. The same figures show the required inverse mapping T_e^{-1}. The generation of the complete finite element mesh containing E elements is a

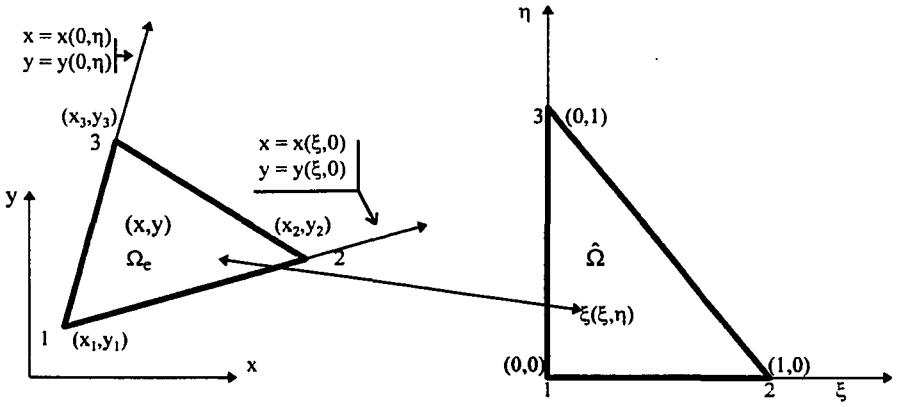

Figure 61. Triangular linear mapping. T_e from the master element $\hat{\Omega}$, to the actual grid Ω_e, and reverse map T_e^{-1}.

sequence of transformations $\{T_1, T_2, \cdots, T_E\}$ in which each element Ω_e is the image of the fixed master element $\hat{\Omega}$ under a coordinate map T_e. The element map T_e is specified by the element coordinates (ξ_j, η_j) and the shape functions $\tilde{\psi}_j$ for the nodes, $j = 1, 2, \cdots, M$, that define the map from $\hat{\Omega}$ to Ω_e. Two dimensional areas combine both coordinates and the resulting quadrilateral transformation in area elements is shown in Figure 62.

The invertible Jacobian $|J|$ in Figure 62 is used to transform the area elements into the grid with (x, y) coordinates:

$$\int_{\Omega_e} g(x,y)dxdy = \int_{\hat{\Omega}} \hat{g}(\xi,\eta)|J(\xi,\eta)|d\xi d\eta. \tag{111}$$

The Jacobian is calculated using the chain rule for each element as

$$|J| = \Big\{\sum_{j=1}^{M} x_j \frac{\partial \hat{\psi}_j}{\partial \xi}\Big\}\Big\{\sum_{j=1}^{M} y_j \frac{\partial \hat{\psi}_j}{\partial \eta}\Big\} - \Big\{\sum_{j=1}^{M} x_j \frac{\partial \hat{\psi}_j}{\partial \eta}\Big\}\Big\{\sum_{j=1}^{M} y_j \frac{\partial \hat{\psi}_j}{\partial \xi}\Big\}. \tag{112}$$

Because J is the area ratio, when $|J| = 0$ an area is transformed to a line, and when $|J| < 0$ then an area is turned inside out. Therefore, each element's Jacobian must

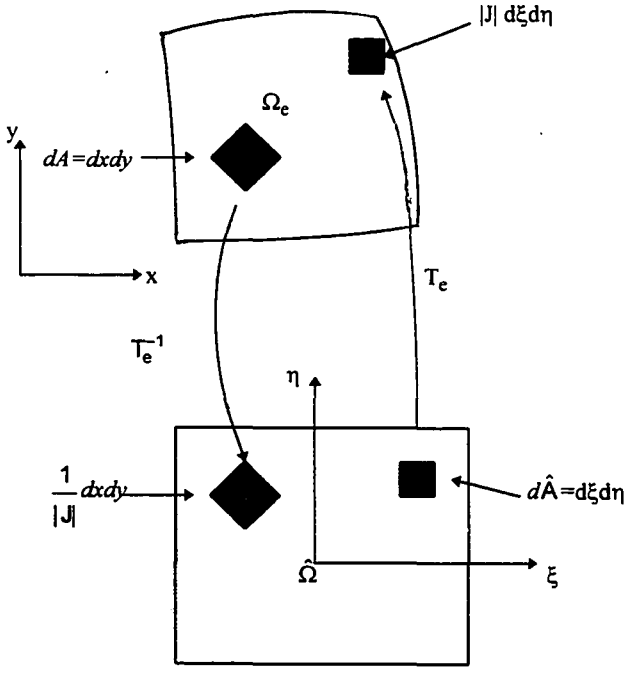

Figure 62. Transformation of quadrilateral area elements

be checked to see if it is positive $|J| \geq 0$ to guarantee an invertible function T_e^{-1} in a right hand coordinate system.

A.4 Shape Function Interpolation

An important physical change occurs in the boundary value problem because of replacing trial functions v with basis functions ϕ. The shape functions and their quadrature rules are developed with properties to maximize the quality of the solution at each given polynomial degree curve, fit boundary conditions of complex domain, ease solution, and be piece-wise defined in each element.

Finite elements use differential calculus to approximate continuity with piece-wise interpolation at the nodes. Discontinuities can also be incorporated by constructing a mesh with nodes located at all points of data discontinuity. As the mesh

is refined with more elements of smaller size, the FE interpolant should become progressively closer to the true solution.

Shape functions interpolate both initial values and solutions for a given mesh and master element. Therefore, one must prescribe the shape functions $\hat{\psi}_j$ for the nodes $j = 1, 2, \cdots, N_e$, that determine the finite element approximation of a value u,

$$u_h^e = \sum_{j=1}^{N_e} u_j{}^e \psi_j^e. \tag{113}$$

The Lagrange family of shape functions are used to construct polynomials of any degree k. Selection of the polynomial degree is a judicious balance of greater accuracy versus computational simplicity. The shape functions used in this study are the triangular 3 and 6 node, and the quadrilateral 4,8, and 9 node elements. The quadrilateral 4 node elements and triangular 3 node elements were shown in Figures 60 and 61 respectively. The quadratic shape function equations for each of the 9 nodes in quadrilateral elements are shown in Figure 63. The equations are second order in both coordinates. The geometry of all shape functions depends on the number of nodes on each side.

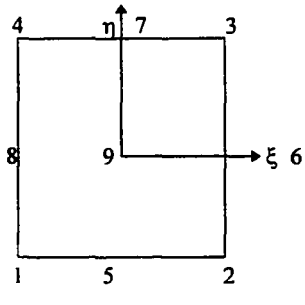

$$\hat{\psi}_1 = \frac{1}{4}(\xi^2 - \xi)(\eta^2 - \eta) \qquad \hat{\psi}_5 = \frac{1}{2}(1-\xi^2)(\eta^2 - \eta)$$

$$\hat{\psi}_2 = \frac{1}{4}(\xi^2 + \xi)(\eta^2 - \eta) \qquad \hat{\psi}_6 = \frac{1}{2}(\xi^2 + \xi)(1-\eta^2)$$

$$\hat{\psi}_3 = \frac{1}{4}(\xi^2 + \xi)(\eta^2 + \eta) \qquad \hat{\psi}_7 = \frac{1}{2}(1-\xi^2)(\eta^2 + \eta)$$

$$\hat{\psi}_4 = \frac{1}{4}(\xi^2 - \xi)(\eta^2 + \eta) \qquad \hat{\psi}_8 = \frac{1}{2}(\xi^2 - \xi)(1-\eta^2)$$

$$\hat{\psi}_9 = (1-\xi^2)(1-\eta^2)$$

Figure 63. Nine node shape functions

An elemental shape function has a value of unity at its node and is zero at all other nodes. Then the functions which are defined on each element are patched together.

This study employs isoparametric mapping. The M nodes and shape functions used in defining the coordinate maps T_e are equivalent to the N_e nodes and shape functions used to calculate the local approximate solution. By definition

$$M = N_e; \quad T_e \text{ is an } \textit{isoparametric} \text{ map.} \tag{114}$$

A.5 Quadrature Integration

The final specification with an element type is the rules of quadrature. "Quadrature" is a general term applied to the numerical evaluation of integrals using a specific set of rules. Physically, quadrature provides discrete numerical integration rules to replace the continuous integrals in the variational calculus problem statement. Because the variational problem statement is reduced to linear terms, the operations of integration are additive. Therefore, the global stiffness matrix K and load vector F can be generated as the computed sum of element matrices K^e and F^e for a typical element Ω_e. This summability of matrices and elemental duplicity (allowing use of a single master element) are among the most important properties of FE.

Since isoparametric finite elements are used, quadrature is used to integrate both spatial coordinates as well as the solution variables. The task at hand is to evaluate closed form integrals such as

$$\mathcal{I} = \int_{x_1}^{x_2} g(x)dx. \tag{115}$$

First, FE uses the master element to transform each arbitrary integral into an integral with limits from -1 to 1:

$$\mathcal{I} = \int_{x_1}^{x_2} g(x)dx \Longrightarrow I = \int_{-1}^{1} g(x(\xi))d\xi = \int_{-1}^{1} g(x)\tilde{\psi}(\xi)d\xi, \tag{116}$$

then the integral can be evaluated numerically using a *quadrature formula*

$$I = \int_{-1}^{1} g(x)\tilde{\psi}(\xi)d\xi \approx \sum_{l=1}^{N_l} g(\bar{x}_l)\tilde{\psi}_l(\xi)w_l, \tag{117}$$

where $\bar{x}_l$ are the integration points on the interval $x_1 \leq x \leq x_2$; $\tilde{\psi}_l$ are the shape functions; w_l are weight numbers, and N_l is the order of the formula. Quadrature associated with shape functions exactly integrates the curve up to the specified order. For example, a linear equation only requires Gaussian quadrature of order one. Therefore, exact equation evaluation would be done with one point at the centroid. The nine-noded quadrilateral shown in Figure 64 uses third-order Gauss quadrature with Gauss sampling points to evaluate the area under a curve. For the three thickness element, there are a total of 27 Gauss points.

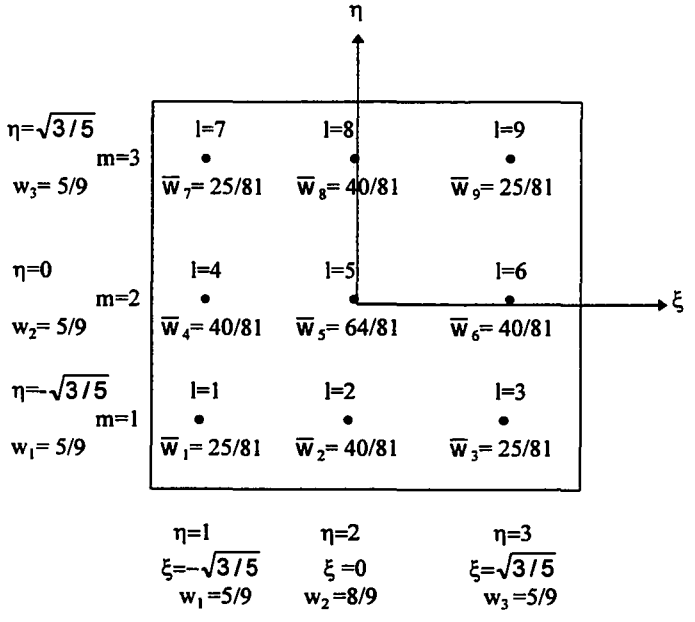

Figure 64. Nine-point Gauss quadrature rule integration points and weights. Tensor product of three point quadratures with respect to ξ and η.

Therefore, one must select the number N_l of integration points, and weights w_l for each integration point $l = 1, 2, \cdots, N_l$. Similar data should also be prescribed for the boundary calculations.

A.6 Conclusion

This appendix has explained the basic finite element theory applied to the *preprocessor* and *processor* for both the heat and coupled heat and moisture modeling. Physical insight was given to the systematic FE method of solving variational calculus of two point boundary value problems. The FE structures outlined were the *master element*, the *element map* T_e, the *shape functions* for interpolation, and the integration *quadrature* rules.

APPENDIX B

FINITE ELEMENT HEAT TRANSFER CODE FLOW CHART

QT is the finite element code that was developed for heat flow. This appendix is a three level flow chart of the program. The three levels are the four structural components, the subroutine sequence, and the documentation of subroutine tasks.

B.1 PART I- Four Components

The fortran program consists of the four functional units shown in Figure 65.

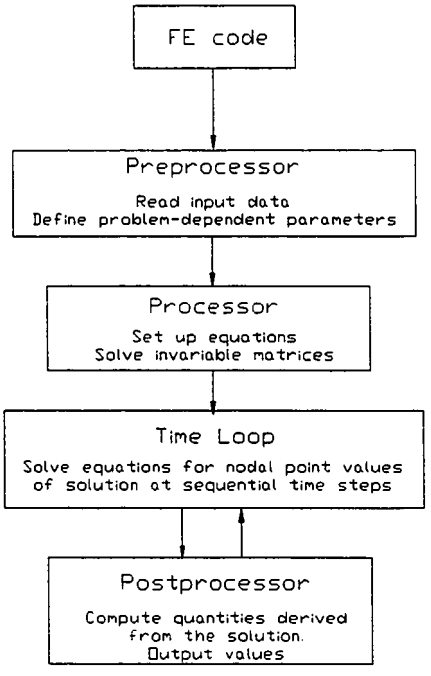

Figure 65. The FE structure of preprocessor, processor, time loop, and postprocessor

B.2 PART II- Subroutine Tree

The expanded diagram in Figure 66 shows the subroutine sequence in each unit.

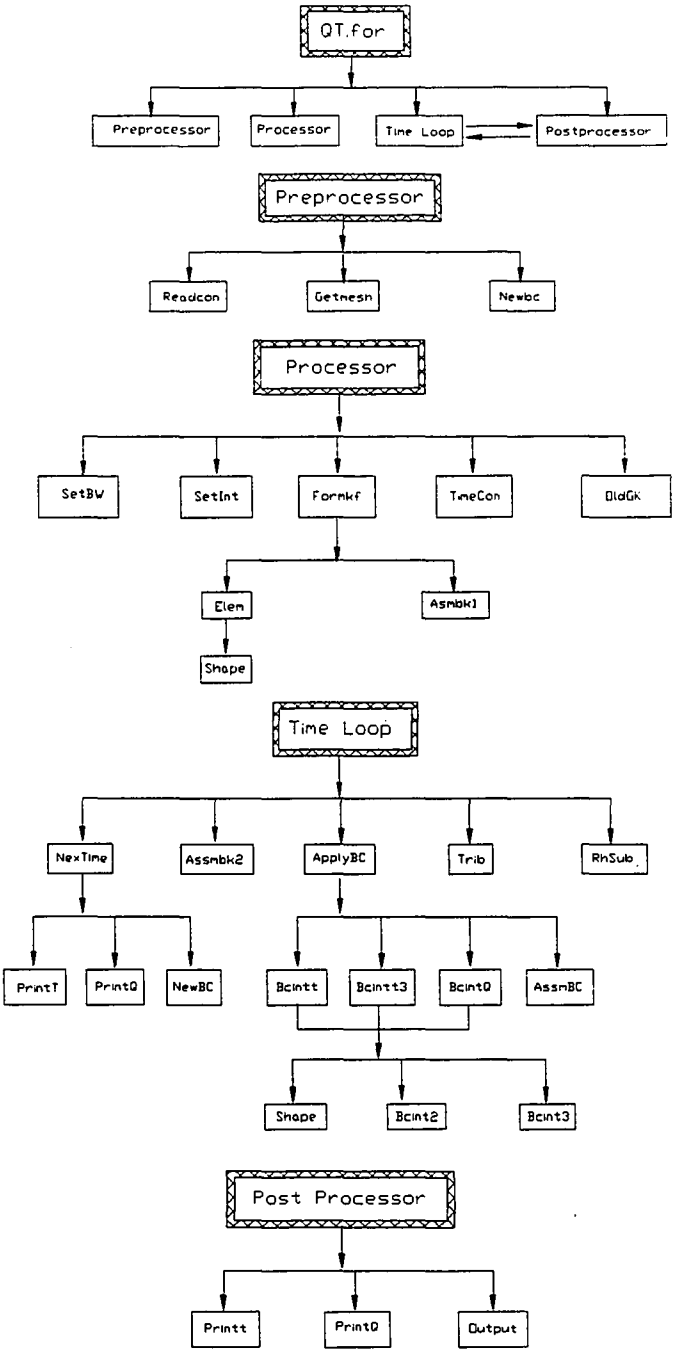

Figure 66. Subroutine sequences in QT

B.3 PART III - Subroutine Applications

The final flowchart level explains the task performed by each subroutine.

Subroutine **READCON** control dat

Subroutine **GETMESH**

Subroutine **NEWBC** p=v=0 gf=gk=0

Subroutine **SETBW** sets bandwidth

Subroutine **SETINT** sets up integration quadrature schemes

Subroutine **FORMKF** GF=GK=CKTNB=0 Call ELEM, ASSMB

I) Subroutine **ELEM** ef=ek=ec=0.

$$
\begin{aligned}
EF(i) &= \sum \{x_f * W(l) * |J| * \psi_i\} \\
EK(i,j) &= \sum \left\{ [x_k * W(l) * |J| * \left(\frac{\partial \psi_i}{\partial x}\frac{\partial \psi_j}{\partial x} + \frac{\partial \psi_i}{\partial y}\frac{\partial \psi_j}{\partial y} \right) \right\} \\
EC(i,j) &= \sum \{\rho * C_p * W(l) * |J| * (\psi_i \psi_j)\}
\end{aligned} \tag{118}
$$

a) Subroutine **SHAPE** ψ_i and $\frac{\partial \psi_i}{\partial x_i}$

II) Subroutine **ASSMBK1**

$$
\begin{aligned}
GF(ig) &= GF(ig) + EF(i) = \sum EF(i) \\
GK(ig,jg) &= GK(ig,jg) + EK(i,j) = \sum EK(i,j) \\
CKTNB(ig,jg) &= CKTNB(ig,jg) + EC(i,j) = \sum EC(i,j)
\end{aligned} \tag{119}
$$

Subroutine **TIMECON**

- read in nbc, tbc(i=1,nbc) for new BC data and printout times
- read in theta, $\theta = 0.5$, $t_1 = 0.05$ hrs , $T_{Final} = 1276$ hrs, Dtexp=0.182 =1.2xtime, nwbc =new BC times, printv =print intervals
- read in NRT,pnodes(j=1,nrt) = print point nodes

Subroutine **OLDGK**

GKOLD(i,j)=GK(i,j) and CKTNBO(i,j)=CKTN(i,j) — store original values

Subroutine **OUTPRINT1**

print initial data at time=(t_1-dt)

- - — — - - —>- - —**START OF TIME LOOP**—— - - — — - - - —>

Subroutine **NEXTIME**

I) Subroutine **PRINTT** print selected temperature field

II) Subroutine **PRINTQ** print selected heat flux field

III) increment TIME, $\Delta t \equiv \Delta t_{n+1} = t_{n+1} - t_n$ =Dt,

IV) Subroutine **NEWBC** if required get new BC (or f data)

$$
\begin{aligned}
&NPOINT = 0 \\
&\quad NBC1 = 5 \text{ essential BC nodes } 135 - 139 = 22.2^{\circ}\text{C} \\
&\quad NBC2 = 0 \quad \text{insulation by default} \\
&\qquad\quad = \text{natural BC on 3 heated sides total 48.1 W/lm} \\
&\qquad\quad = 3 = P_k + \gamma_f = \gamma_f = 574 \text{ W/m}^2
\end{aligned} \tag{120}
$$

Subroutine **ASSMBK**

re-setup Gk,Cktnb,Gf with new Temperature T_n, time t_{n+1}, and $\Delta t_{n+1} = (t_{n+1} - t_n)$

- $$[G\tilde{K}] = \left\{\theta * \Delta t_{n+1} * [G\tilde{K}old] + [\tilde{C}KTNBo]\right\} = \theta * \Delta t_{n+1} * G\tilde{K}_{n+1} + E\tilde{C}$$
$$= \begin{bmatrix} G\tilde{K}_{11} & \cdots & G\tilde{K}_{1N} \\ \vdots & \ddots & \vdots \\ G\tilde{K}_{N1} & \cdots & G\tilde{K}_{NN} \end{bmatrix} \tag{121}$$

In this program $\tilde{C}$ and $\tilde{K}$ are constant, but not P in $[K + P]_{n+1}$.

- $$[\tilde{C}KTNB] = [\tilde{C}KTNBo] - (1-\theta)\Delta t_{n+1} * [G\tilde{K}old]$$
$$= \left\{\tilde{C} - (1-\theta)\Delta t_{n+1} * \tilde{K}_n\right\} \tag{122}$$

- $G\tilde{F} = 0$ (re-initialize)

$$[G\tilde{F}] = \sum_{i,j} \left\{\tilde{C}KTNB_{i,j} * T_{n,j}\right\} = \left[\tilde{C} - (1-\theta)\Delta t_{n+1} * \tilde{K}_n\right]\left[T_n\right] = \begin{bmatrix} \tilde{F}_1 \\ \vdots \\ \tilde{F}_N \end{bmatrix} \tag{123}$$

Subroutine **APLYBC**

- NBC1 penalty method for $T = 22.2°C$

$$GF(n) = 1E20 * VBC1(i)$$
$$GK(n,1) = 1E20 \tag{124}$$

note: GK is permanent and inverted (permanent BC or unstable?)

- Natural boudary conditions - NBC2

⋆ Abrupt data inputs (not smooth weather data)

$$F_n = \gamma_n \; - - - > BC\#1 \text{ const temp at } T_n$$
$$F_{n+1} = \gamma_{n+1} \; - - - > BC\#2 \text{ const temp at } T_{n+1}$$
$$P_n = P_n \; - - - > BC\#1 \text{ variable temp at } T_n$$
$$P_{n+1} = P_{n+1} \; - - - > BC\#2 \text{ variable temp at } T_{n+1} \tag{125}$$

⋆ call BCINTQ/TF for NBC2

Subroutine **BCINTQF /TF** call BCINT2 call BCINT3F

Subroutine **BCINT2** for $|J|$and $W(l)$ - twice

Subroutine **BCINT3F** 2-pt integration per side

$$\text{gamef} = \gamma_f = \sum_{i=1}^{3} \left\{ g * \psi_i * |J| * W(l) \right\}$$

note: W(l)=0.5 for triangle and =1.0 for rectangle

where g= 1 (no P or γ yet)

because $\int (\gamma + HT_\infty + (HT = P)) d\psi = (\gamma + HT_\infty + P) \int d\psi$

$$\text{PeK} = \sum_{i=1}^{3} \sum_{i=1}^{3} \left\{ p * \psi_i * \psi_j * |J| * W(l) \right\} \text{where p} = 1 \tag{126}$$

⋆ back to Subroutine **APLYBC**

$$[BCF] = \left\{ \sum_{i=1}^{3} \gamma * \phi_i(x,y) * |J| * W(l) \right\} * \Delta T_{n+1} \Big[\theta F_{n+1} + (1-\theta) F_n \Big]$$
$$= \{gamef\} * \Delta T_{n+1} \Big[\theta F_{n+1} + (1-\theta) F_n \Big] \quad (127)$$

$$[BCPk] = \left\{ \sum_{i=1}^{3} \sum_{i=1}^{3} P * \phi_i(x,y) * \phi_j(x,y) * |J| * W(l) \right\} * \theta * \Delta T_{n+1} * P_{n+1}$$
$$= \{\{PeK\} * \phi_i(x,y) * \phi_j(x,y) * |J| * W(l)\} * \theta * \Delta T_{n+1} * P_{n+1} \quad (128)$$

$$[BCPc] = \left\{ \sum_{i=1}^{3} \sum_{i=1}^{3} P * \phi_i(x,y) * \phi_j(x,y) * |J| * W(l) \right\} * (-1) * (1-\theta) * \Delta T_{n+1} * P_n$$
$$= \{\{PeK\} \phi_i(x,y) \phi_j(x,y) |J| W(l)\} * (-1) * (1-\theta) \Delta T_{n+1} P_n \quad (129)$$

Subroutine **APLYBCK** Does nothing (for K loads Pe = 0 and f will be changed later)

pt loads -none

essential BC - none

Natural BC p=v=0 no effect

- Call BCINTQ/P call BCINT2 call BCINT3P get $|J|$ and $W(l)$
- Call ASSMBK2

Subroutine **BCINT3P/Q**

$$[P_{ek}] = \sum \Big\{ p * W(l) |J| * \psi_i * \psi_j \Big\} = 0 \quad (130)$$

Subroutine **ASSMBK2**

$$GK(ig,jg) = GK(ig,jg) + P_{ek}(i,j) \; ----> \text{no change } (p=0) \quad (131)$$

- call Subroutine **ASSMBC**

$$\sum_{i=1}^{ng} G\bar{F}(ig) = GF(ig) + BCF(i)$$

which in matrix formulation is

$$\begin{bmatrix} \tilde{GF}_1 \\ \vdots \\ \tilde{GF}_N \end{bmatrix} = \begin{bmatrix} \{[\tilde{C} - (1-\theta)\Delta t_n \tilde{K}]T_n\}_1 \\ \vdots \\ \{[\tilde{C} - (1-\theta)\Delta t_n \tilde{K}]T_n\}_N \end{bmatrix} + \begin{bmatrix} \{\Delta t_n[\theta \tilde{F}_{n+1} + (1-\theta)\tilde{F}_n]\}_1 \\ \vdots \\ \{\Delta t_n[\theta \tilde{F}_{n+1} + (1-\theta)\tilde{F}_n]\}_N \end{bmatrix}. \quad (132)$$

- $$[G\bar{K}] = [G\bar{K}] + [bcpk]$$
$$= \left\{\theta * \Delta t_{n+1} * [K + P_{n+1}] + [\tilde{C}\right\}$$
$$= \left\{\theta * \Delta t_{n+1} * [G\tilde{K}old] + [\tilde{C}KTNBo]\right\}$$
$$= \begin{bmatrix} G\bar{K}_{11} & \cdots & G\bar{K}_{1N} \\ \vdots & \ddots & \vdots \\ G\bar{K}_{N1} & \cdots & G\bar{K}_{NN} \end{bmatrix} \quad (133)$$

In this program $\tilde{C}$ and $\tilde{K}$ are constant (but not P in $[K + P]_{n+1}$)

- $$[\tilde{C}KTNB] = [\tilde{C}KTNBo] - (1-\theta)\Delta t_{n+1} * [G\tilde{K}old]$$
$$= \left\{\tilde{C} - (1-\theta)\Delta t_{n+1} * [\tilde{K} + P_{n+1}]\right\} \quad (134)$$

Subroutine **ASSMBF**

$\sum_{i=1}^{ng} G\bar{F}(ig) = [GF](ig) + [CKTNB]T_n$

Subroutine **TRIB**

Tridiagonalize

$$[G\bar{K}]^{-1} = \left[\tilde{C} + \theta * \Delta t_{n+1} * \tilde{K}_{n+1}\right]^{-1} = \begin{bmatrix} G\bar{K}_{11} & \cdots & G\bar{K}_{1N} \\ \vdots & \ddots & \vdots \\ G\bar{K}_{N1} & \cdots & G\bar{K}_{NN} \end{bmatrix}^{-1} \quad (135)$$

Subroutine **RHSUB**

$$[T_{n+1}] = [G\bar{K}]^{-1}[G\bar{F}] \equiv [\bar{K}]^{-1}[\bar{F}]$$

$$= \left[\tilde{C} + \theta * \Delta t_{n+1} * (\tilde{K} + \tilde{P})_n\right]^{-1}\left[\{\tilde{C} - (1-\theta)\Delta t_{n+1} * (\tilde{K} + \tilde{P})_n\}T_n\right.$$

$$\left.+\Delta t_{n+1}\{\theta * \tilde{F}_{n+1} + (1-\theta) * \tilde{F}_n\}\right] \tag{136}$$

which in matrix formilation is

$$\begin{bmatrix} T_1 \\ \vdots \\ T_N \end{bmatrix} = \begin{bmatrix} G\bar{K}_{11} & \cdots & G\bar{K}_{1N} \\ \vdots & \ddots & \vdots \\ G\bar{K}_{N1} & \cdots & G\bar{K}_{NN} \end{bmatrix}^{-1} \begin{bmatrix} G\bar{F}_1 \\ \vdots \\ G\bar{F}_N \end{bmatrix} \tag{137}$$

POST PROCESS

I) Subroutine **PRINTT**

print iteration, time, Fourier #, and temperature at select nodes

II) Subroutine **PRINTQ**

print iteration, time, Fourier #, and heat flux at select nodes

< – ——— end of time loop back to TIMESTEP ————————< ————————

Subroutine **OUTPUT** print $[T^{n+1}]$

print all node #, x, y, and temperature

STOP

END

APPENDIX C

FINITE ELEMENT HEAT TRANSFER AND MOISTURE CODE FLOW CHART

QM is the finite element code that was developed for heat and mass transfer. This appendix is a three level flow chart of the program. The three levels are the four structural components, the subroutine sequence, and the documentation of subroutine tasks.

C.1 PART I- Four Components

The fortran program consists of the four functional units shown in Figure 67.

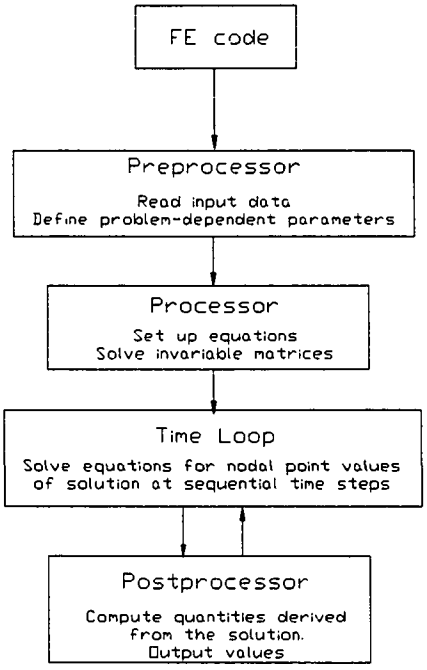

Figure 67. The FE structure of preprocessor, processor, time loop, and postprocessor

C.2 PART II- Subroutine Tree

The expanded diagram in Figure 68 shows the overall subroutine sequence in each unit, while Figure 69 shows the time loop for heat and mass transfer.

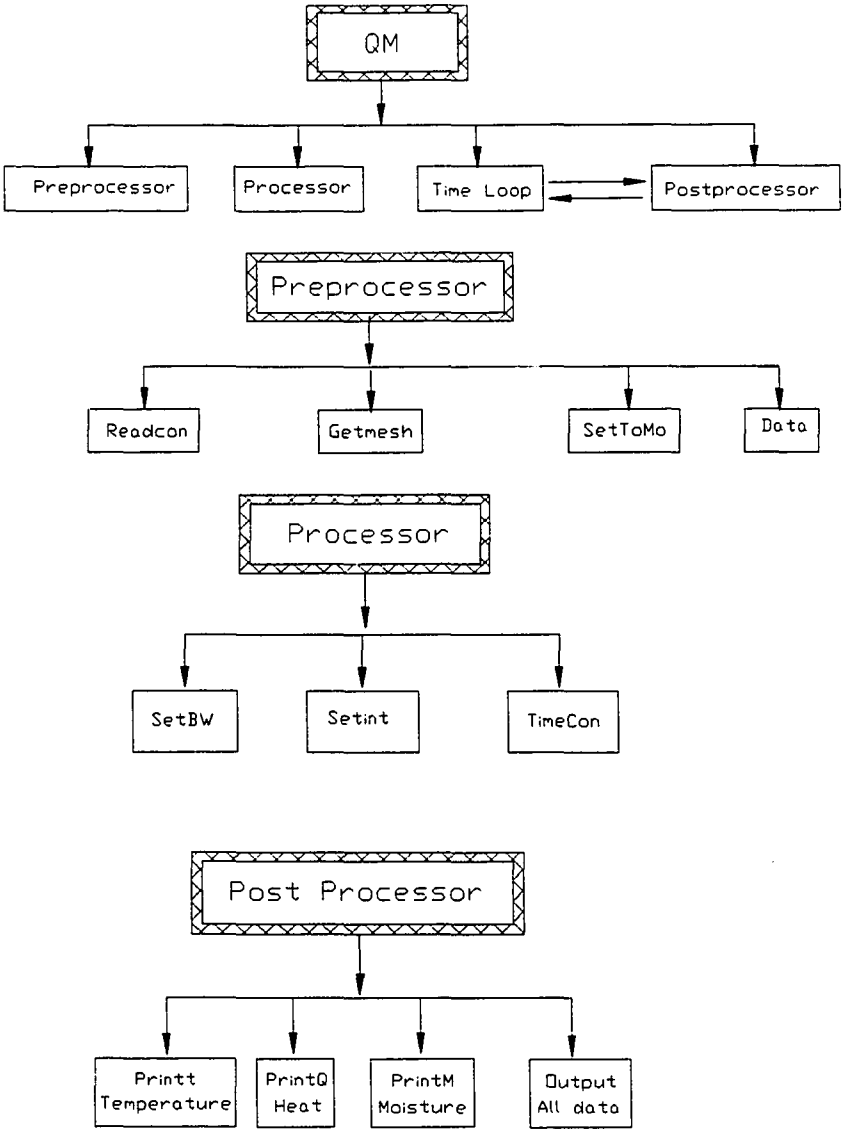

Figure 68. Overall subroutine sequences in QM

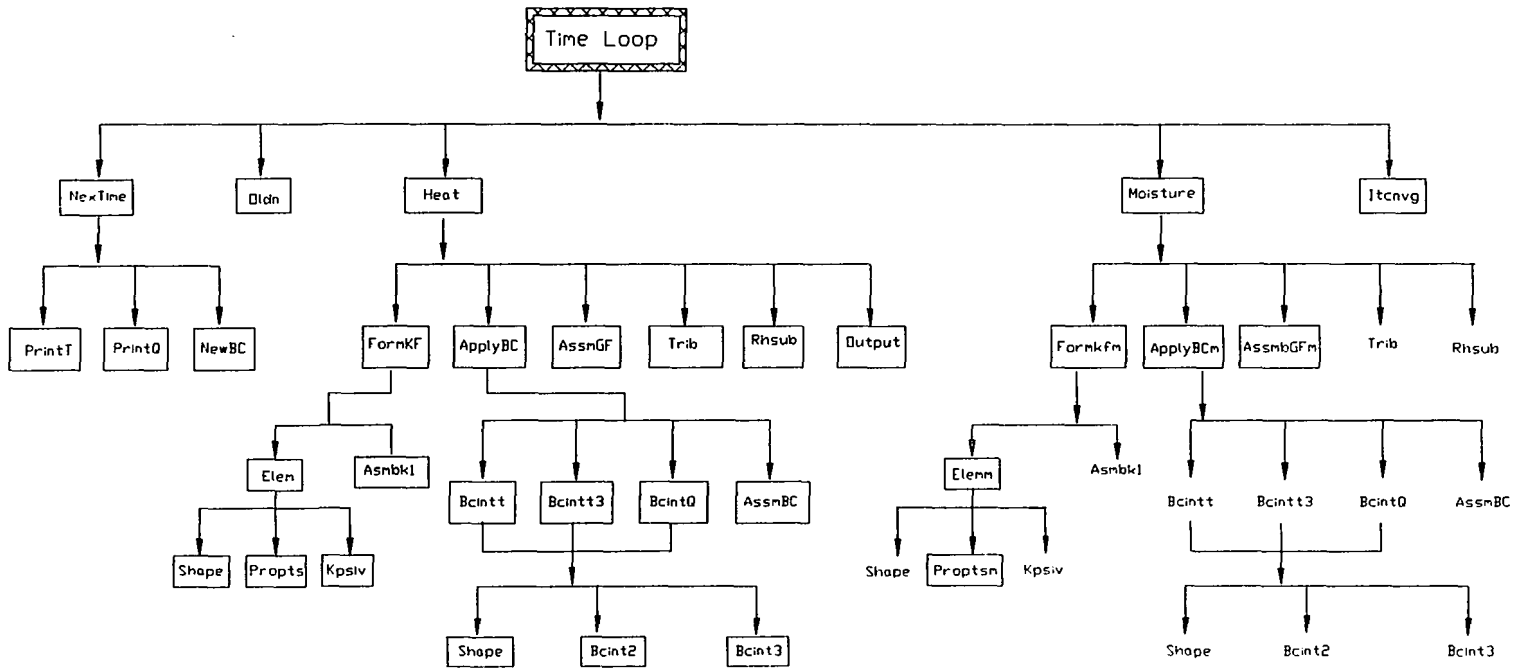

Figure 69. Time loop subroutine sequences in QM

C.3 PART III - Subroutine Applications

The overall process and notation is

$$[Cp]\{\dot{T}\} + ([K_{T\lambda}] + [K_{bcT}])\{T\} = [F_L]\{\Psi\} + [F_{Qh}]$$

$$\text{brief notation} \longrightarrow [\tilde{C}p]\{\dot{T}\} + [\tilde{K}]\{T\} = [\tilde{F}]$$

$$\text{reformulate as} \longrightarrow [Gk]\{T_{n+1}\} = [Gf]$$

$$\text{solve as} \longrightarrow \{T_{n+1}\} = [Gk]^{-1} * [Gf] \tag{138}$$

$$\begin{bmatrix} G_{CKT,11} & \cdots & G_{CKT,1N} \\ \vdots & \ddots & \vdots \\ G_{CKT,N1} & \cdots & G_{CKT,NN} \end{bmatrix}_{n+1} \begin{bmatrix} T_1 \\ \cdot \\ \vdots \\ T_N \end{bmatrix}_{n+1} = \begin{bmatrix} F_{CK,11} & \cdots & F_{CK,1N} \\ \vdots & \ddots & \vdots \\ F_{CK,N1} & \cdots & F_{CK,NN} \end{bmatrix}_{n} \begin{bmatrix} T_1 \\ \cdot \\ \vdots \\ T_N \end{bmatrix}_{n}$$

$$- \begin{bmatrix} F_L,11 & \cdots & F_L,1N \\ \vdots & \ddots & \vdots \\ F_L,N1 & \cdots & F_L,NN \end{bmatrix}_{n} \begin{bmatrix} \Psi_1 \\ \cdot \\ \vdots \\ \Psi_N \end{bmatrix}_{n} + \begin{bmatrix} F_{Qh,1} \\ \cdot \\ \vdots \\ F_{Qh,N} \end{bmatrix}_{n} \tag{139}$$

The final flowchart level explains the task performed by each subroutine.

Subroutine **READCON** control dat • read-in $\longrightarrow$ Nnode, Nnelem, Nmat

Subroutine **GETMESH**

• read-in $\longrightarrow$ nod,x(1,nod),x(2,nod),k,f,ρ,Cp,ne, mat(j),nodes(i,j)

Subroutine **setToMo** sets initial temp and moisture

I • read-in $\longrightarrow$ To(nmat) and VWCo(nmat)

Subroutine **DATA**

• read-in $\longrightarrow$ T_o,r_o,T_{sec} Cp(imat,j),j=1,5$\rightarrow$ Toc, thetam, thetao, rhoo, xmat(j), porosity, ithmax, conv

Subroutine **SETBW** sets bandwidth

Subroutine **SETINT** sets up integration quadrature schemes

Subroutine **TIMECON**

I • read-in $\longrightarrow$ nbc, tbc(i=1,nbc) for new BC data and printout times

II • read-in$\longrightarrow$ θ, t_1 (hrs) , T_{Final} (hrs), Dtexp=0.182 =1.2xtime, nwbc (times), printv (print intervals)

• read-in ⟶ NRT,tp(j),nprt(j),pnodes(j=1,nrt) = print point nodes

III • read-in ⟶ heat print nodes ncntr,centr,nqs,matk,nq

Subroutine Oupupt

print initial data at time=(t_1-dt)

==== === =====-> —**START OF TIME LOOP**— ========->

(T1) Subroutine **NEXTIME**

i) increment TIME, $\Delta t \equiv \Delta t_{n+1} = t_{n+1} - t_n$ =Dt,

I) Subroutine **PRINTT** print selected temperature field

II) Subroutine **PRINTQ** print selected heat flux field

III) Subroutine **PRINTM** print selected moisture nodes

i) • read-in ⟶ npoint, nbc1, nbc2, nbc3=vwc, time-c

IV) Subroutine **NEWBC** if required get new BC (or f data)

• read-in ⟶ point load BC, esent BC, Natural BC, VWC

$NPOINT = 0$

$NBC1 = 5$ essential BC nodes 135 – 139 = 22.2°C

$NBC2 = 0$ insulation by default

= natural BC on 3 heated sides total 48.1 W/lm

$= 3 = P_k + \gamma_f = \gamma_f = 574$ W/m^2

$NBC3 = 5$ moisture BC nodes- initial setting of nodes

Node first, last, increment (140)

(T2) Subroutine **OLDn**

store old nth time step matrices for convergence check

Tn(900) and Ppsin(900)

—- - ———> start iterate between moisture and heat ———— - ->

| (T3) Subroutine **HEAT**

(H1) CALL FORMKF

(H2) CALL ASSMBGF

(H3) CALL APLYBC

(H4) CALL TRIB

(H5) CALL RHSUB

(H6) CALL OUTPUT

| (T4) Subroutine **MOISTURE**

(H1) CALL FORMKFM

(H2) CALL ASSMBGFM

(H3) CALL APLYBCM

(H4) CALL TRIB

(H5) CALL RHSUB

(H6) CALL OUTPUT

(T5) Subroutine **Itconvg**

| If converged cnvgd=2

|

——- — — ——> end iterate between moisture and heat ———- — - ——>

(H1) Subroutine **FORMKF** $F_L = K_{T\lambda} = C_p = 0 \longrightarrow [Fl] = [Ktl] = [Cp] = 0$

I) Subroutine **ELEM** ecp=ekt=efl=0.

(a) Subroutine **SHAPE** ψ_i and $\frac{\partial \psi_i}{\partial x_i}$

(b) Subroutine **PROPTS** C_P=f($T_c, T_{oc}, \theta_m, \theta_o, \rho_o, \theta_w$)

$$[EC_P](i,j) = \sum \left\{ C_{p_j} * W(l) * |J| * \psi_i \psi_j \right\} \tag{141}$$

(c) $[E_{KT}]$

$\lambda_{i,j} = f(t, \theta_w, \text{soil type})$ assume $\lambda_x = \lambda_y$

(iii) $[EK_{T\lambda}](i,j) = \sum \left\{ \lambda_{i,j} * W(l) * |J| * \left(\frac{\partial \psi_i}{\partial x}\frac{\partial \psi_j}{\partial x} + \frac{\partial \psi_i}{\partial y}\frac{\partial \psi_j}{\partial y} \right) \right\} \quad \frac{J}{m - sec - ^\circ K}$

(a) L=f(t) = $2.5 \times 10^6 - 2430T$ (J/kg)

$0 \leq T \leq 120^\circ C$ Hampton (1989)

$\rho_w = f(T) = 1000 + 0.0145T - 0.00515T^2 \quad (\mathrm{kg/m^3})$

$0 \leq T \leq 45°C$ Finlayson et al. (1978)

(ii) Subroutine **kpsiv**

$k_{\Psi v} = f(\theta_w)$

$$[E_{FL}](i,j) = \sum \left\{ L_{i,j}\rho_{wi,j}k_{\Psi vi,j} * W(l) * |J| * \left(\frac{\partial \psi_i}{\partial x}\frac{\partial \psi_j}{\partial x} + \frac{\partial \psi_i}{\partial y}\frac{\partial \psi_j}{\partial y} \right) \right\} \qquad (142)$$

II) Subroutine **ASSMBK1**

$$\begin{aligned} [F_L](ig,jg) &= [F_L](ig,jg) + [E_{FL}](i,j) = \sum [E_{FL}](i,j) \\ [K_{T\lambda}](ig,jg) &= [K_{T\lambda}](ig,jg) + [EK_{T\lambda}](i,j) = \sum [EK_{T\lambda}](i,j) \\ [C_P](ig,jg) &= [C_P](ig,jg) + [EC_P](i,j) = \sum [EC_P](i,j) \end{aligned} \qquad (143)$$

(H2) Subroutine **ASSMBGF**

re-setup Gk, and Gf with new temperature T_n, moisture θ_w time t_{n+1} and $\Delta t_{n+1} = (t_{n+1} - t_n)$, etc

- $$[G\bar{K}] = \left[\frac{[Cp]}{\Delta t} + \theta([K_{T\lambda}]) \right]_{t_{n+1}} = \frac{C_P}{\Delta t} + \theta\lambda$$

$$= \begin{bmatrix} [Cp]_{11}/\Delta t + \theta * \bar{K}_{T\lambda 11} & \cdots & [Cp]_{1N}/\Delta t + \theta * \bar{K}_{T\lambda 1N} \\ \vdots & \ddots & \vdots \\ [Cp]_{N1}/\Delta t + \theta * \bar{K}_{T\lambda N1} & \cdots & [Cp]_{NN}/\Delta t + \theta * \bar{K}_{T\lambda NN} \end{bmatrix}_{t_{n+1}}$$

$$= \begin{bmatrix} G\bar{K}_{11} & \cdots & G\bar{K}_{1N} \\ \vdots & \ddots & \vdots \\ G\bar{K}_{N1} & \cdots & G\bar{K}_{NN} \end{bmatrix}_{t_{n+1}} \qquad (144)$$

(later addition of BC $\theta[K_{bcT}] = \theta[H + C_{vw}]$)

- $G\bar{F} = 0$ (re-initialize)

$$[G\bar{F}] = \left[\frac{[Cp]}{\Delta t} - (1-\theta) * [K_{T\lambda}] \right] \left\{ T_n \right\} - \left[[Fl] \right]_n \left\{ \Psi \right\}_n = \begin{bmatrix} G\bar{F}_1 \\ \vdots \\ G\bar{F}_N \end{bmatrix} \qquad (145)$$

* later addition of BC $\left[-(1-\theta) * [K_{bcT}] \right] \{T\}_n \Big] = -(1-\theta) * [H + C_{vw}]\{T\}_n$ and $[F_{QH}] = Q_h + HT\infty + S_h + S_l T_l$)

(H3) Subroutine **AplyBC**

Npoint, NBC1, NBC2

- NBC1 penalty method for $T = 22.2°C$

$$GF(n) = 1E20 * VBC1(i)$$
$$GK(n,1) = 1E20 \tag{146}$$

- Natural boudary conditions - NBC2

⋆ Abrupt data inputs (not smooth weather data)

$$F_n = \gamma_n \; - - - > BC\#1 \text{ const temp at } T_n$$
$$F_{n+1} = \gamma_{n+1} \; - - - > BC\#2 \text{ const temp at } T_{n+1}$$
$$P_n = P_n \; - - - > BC\#1 \text{ variable temp at } T_n$$
$$P_{n+1} = P_{n+1} \; - - - > BC\#2 \text{ variable temp at } T_{n+1} \tag{147}$$

⋆ for NBC2 temp indep (Q_h and S_h) Call Bcint(x)

⟶ if nodes=(6,3,4/8) Call Bcint(t,t3,q)

Subroutine **BCINTQF /TF** call BCINT2, BCINT3F

Subroutine **BCINT2** for $|J|$and $W(l)$ - twice

Subroutine **BCINT3F** 2-pt integration per side

BC a)Qh - heat (⟶ [FQh]) b) P_T temp dependent (⟶ $[K_{bcT}]\cdot$ T)

$$\text{gamef} = \gamma_f = \sum_{i=1}^{3} \Big\{ g * \psi_i * |J| * W(l) \Big\}$$

note: W(1)=0.5 for triangle and =1.0 for rectangle

where g= 1 (no P or γ yet- $\gamma = Q_h + S_h$) because $\int \gamma d\psi \approx \gamma \int d\psi$

$$\text{PeK} = \sum_{i=1}^{3} \sum_{i=1}^{3} \Big\{ p * \psi_i * \psi_j * |J| * W(l) \Big\} \text{where p} = 1 \tag{148}$$

⋆ back to Subroutine **AplyBC**

a) Surface integral VBC2(1,i)

$$= \int_s \gamma * (Q_h + HT_\infty) \approx \sum_s \psi_{si} * Q_h * |J| * Wl + \sum_s HT_\infty * \psi_{si} * |J| * Wl$$

$$[BcS](j) = \{gamef\} * \Delta T_{n+1}\Big[\theta(Q_h + HT_\infty)_{n+1} + (1-\theta)(Q_h + HT_\infty)_n\Big] \quad (149)$$

b) Volume integral VBC2(2,i)

$$\{BcV\} = \int_v \gamma * (S_h + C_v w S_l T_l) \approx \sum_v \psi_i S_h * |J| * Wl c_{vw} \sum_v S_l \psi_i T_l * |J| * Wl$$

$$[BcV](j) = \{gamef\} * \Delta T_{n+1}\Big[\theta(S_h + C_v w S_l T_l)_{n+1} + (1-\theta)(S_h + C_v w S_l T_l)_n\Big] \quad (150)$$

c) Surface integral-temperature dependent VBC2(3,i)

$$= \int_s \gamma * (H) \approx \sum_s \psi_{si} Q_h \psi_{sj} * |J| * Wl$$

$$[BcST](i,j) = \{\{P\} * \psi_i(x,y) * \psi_j(x,y) * |J| * W(l)\} * \theta * \Delta T_{n+1} * Q_{hn+1} \quad (151)$$

d) Volume integral-temperature dependent VBC2(4,i)

$$\{BcVT\} = \int_v \gamma * (C_v w S_l) \approx c_{vw} \sum_v S_l \psi_i \psi_j T_l * |J| * Wl$$

$$[BcVT](i,j) = \{\{P\} * \psi_i(x,y) * \psi_j(x,y) * |J| * W(l)\} * (C_v w S_l)_{n+1} \quad (152)$$

Units =(J/kg-°C)

* Call AssmBC

$GF = GF + f(BCS, BCV)$

Subroutine **BCINT3P/Q**

$$[P_{ek}] = [K_{bcT}] = \sum_s \Big\{H * W(l)|J| * \psi_{si} * \psi_{sj}\Big\} + c_{vw} \sum_v \Big\{S_L * W(l)|J| * \psi_i * \psi_j\Big\} \quad (153)$$

Subroutine **AssmBC**

b) P_T temperature dependent BC ($\longrightarrow [K_{bcT}]\cdot$ T)

where $[K_{bcT} \longrightarrow [H + C_{vw}]$

$$[Gk](i,j) = [Gk](i,j) + \theta * \sum^{ig,jg} \{[BcSV](ig,jg) + [BcVT](ig,jg)\} \quad (154)$$

$$
\begin{aligned}
&= \left\{ \frac{[Cp]}{\Delta t} + \theta * [K_{T\lambda}]_{n+1} \right\} + \{\theta * [K_{bcT}]_{n+1}\} \\
&= \left\{ \frac{[Cp]}{\Delta t} + \theta([K_{T\lambda}]_{n+1} + [K_{bcT}]_{n+1}) \right\} \\
&= \left[\frac{[Cp]}{\Delta t} + \theta(\lambda + H + C_{vw}S_l \right]_{n+1} \\
&= \begin{bmatrix} G\bar{K}_{11} & \cdots & G\bar{K}_{1N} \\ \vdots & \ddots & \vdots \\ G\bar{K}_{N1} & \cdots & G\bar{K}_{NN} \end{bmatrix}
\end{aligned} \tag{155}
$$

In this program $[Cp]$,$[K_{T\lambda}]$ and $[K_{bcT}]$ are variable and, therefore, recalculated for each t (time) but not heat/mass iteration.

(H4) Subroutine **ASSMBK1**

$$
[Gf](j) = [Gf](j) + \sum_{(j)}^{jg} -(1-\theta) * [BcST](i,j) * [T](j) + [BcVT](i,j) * [T](j)
$$

$$
+\theta * ([BcS](j) + [BcV](j)) + (1-\theta) * ([BcS](j) + [BcV](j)) \tag{156}
$$

$$
G\bar{F}(ig) = GF(ig) + \sum_{i=1}^{ng} P_{ef}(i)
$$

$$
= \left[\frac{[Cp]}{\Delta t} - \Big(1-\theta\Big)\Big([K_{T\lambda}]\Big] \Big\{T_n\Big\} - [Fl]\{\Psi\} + \{F_{Qh}\} + [-(1-\theta) * [K_{bcT}]] \Big\{T_n\Big\}
$$

$$
= \left[\frac{[Cp]}{\Delta t} - (1-\theta)(\lambda + H + C_{vw}S_l \right] \Big\{T_n\Big\} - [L\rho_w K_{\Psi v}]\Big\{\Psi_n\Big\}
$$

$$
+[Q_h + HT_\infty + S_h + C_{vw}S_l]
$$

which in matrix formulation is

$$
\begin{bmatrix} G\bar{F}_1 \\ \vdots \\ G\bar{F}_N \end{bmatrix} = \begin{bmatrix} \bar{F}_1 \\ \vdots \\ \bar{F}_N \end{bmatrix} + \begin{bmatrix} B\bar{C}F_1 \\ \vdots \\ B\bar{C}F_N \end{bmatrix} = \begin{bmatrix} \bar{F}_1 \\ \vdots \\ \bar{F}_N \end{bmatrix} \tag{157}
$$

(H4) Subroutine **ASSMBGF**

(H6) Subroutine **TRIB**

$$\text{Tridiagonalize } [G\bar{K}]^{-1} =$$

$$\left[\frac{[Cp]_{n+1}}{\Delta t} + \theta([K_{T\lambda}]_{n+1} + [K_{bcT}]_{n+1})\right]^{-1} = \begin{bmatrix} G\bar{K}_{11} & \cdots & G\bar{K}_{1N} \\ \vdots & \ddots & \vdots \\ G\bar{K}_{N1} & \cdots & G\bar{K}_{NN} \end{bmatrix}^{-1} \tag{158}$$

(H7) Subroutine **RHSUB**

$$\begin{aligned} [T_{n+1}] &= [G\bar{K}]^{-1}[G\bar{F}] \equiv [\bar{K}]^{-1}[\bar{F}] \\ &= \left[\frac{[C]}{\Delta t} + \theta([K_{T\lambda}]_{n+1} + [K_{bcT}]_{n+1})\right]^{-1} \\ *\left[\frac{[Cp]_{n+1}}{\Delta t} - \Big(1-\theta\Big)\Big([K_{T\lambda}]_{n+1} + [K_{bcT}]_{n+1}\Big)\right]\Big[T_n\Big] &- [F_L]\{\Psi\} + [F_{Qh}]\}\Big] \end{aligned} \tag{159}$$

which in matrix formilation is

$$\begin{bmatrix} T_1 \\ \vdots \\ T_N \end{bmatrix} = \begin{bmatrix} G\bar{K}_{11} & \cdot & \cdots & G\bar{K}_{1N} \\ \cdot & \ddots & \cdot & \cdot \\ \vdots & \cdot & \ddots & \vdots \\ G\bar{K}_{N1} & \cdot & \cdots & G\bar{K}_{NN} \end{bmatrix}^{-1} \begin{bmatrix} G\bar{F}_1 \\ \vdots \\ G\bar{F}_N \end{bmatrix} \tag{160}$$

POST PROCESS

(H7) Subroutine **PRINTT**

print iteration, time, Fourier #, and temperature at select nodes

(H8) Subroutine **PRINTQ**

print iteration, time, Fourier #, and heat flux at select nodes

< – ——— end of time loop back to TIMESTEP ————————< ————————

Subroutine **OUTPUT** print $[T^{n+1}]$

print all node #, x, y, and temperature

STOP

END

VITA

Norman K. Muraya was born on July 14, 1961, in Muranga, Kenya to Beth Wanjiru and Ayub Muraya. Muraya graduated from Rift Valley Academy high school in 1980. Later that year he enrolled at Wheaton College in Wheaton, Illinois. He competed in inter-collegiate soccer and received a B.S. in Physics in 1984.

From September 1984, to December 1986, he earned a B.S. in Mechanical Engineering from Texas A&M University. Then from September 1987, to December 1988, he earned a Mechanical Engineering M.S. in Energy Management from Texas A&M University. His thesis studies and employment were provided by the cogeneration project which was funded by the Texas Governor's Energy Management Center.

Muraya enrolled in the Ph.D. program for Mechanical Engineering at Texas A&M University in January 1989. From May to August 1989, he interned with the Governor's Energy Management Center in College Station. Employment and significant industrial experience was provided by performing energy and waste audits through the Department of Energy (DOE) programs for Energy Analysis and Diagnostic Center, and Industrial Assessment Center. Additional employment was also provided by cogeneration analysis and energy audit reviews for the State of Texas LoanSTAR project.

Muraya's two permanent addresses are (1) P.O. Box 154 Muranga, Kenya, and (2) P.O. Box 2883 College Station, Texas 77841.

The typist and graphical artist for this thesis was the author.